PHONON REFLECTION FROM CRYSTAL INTERFACES AND THE KAPITZA PROBLEM

Thesis by

Peter Taborek

In Partial Fulfillment of the Requirements
of the Degree of
Doctor of Philosophy

California Institute of Technology
Pasadena, California

1980

(Submitted November 15, 1979)

To my Parents

Jerry and Ella Taborek

ACKNOWLEDGEMENTS

Throughout the course of this project I have received much help and many valuable ideas from all the people in Low Temperature Physics. I would like particularly to thank

John Herb, for introducing me to the Kapitza problem and to the vagaries of experimental science;

Harris Notarys, for his interest in my day-to-day successes and failures, for much helpful advice on experimental matters and for his late-night companionship;

Jeff Greif, for many pertinent suggestions concerning both the experiment and the interpretation of the data, as well as enjoyable discussions on the rest of the universe; and,

David Goodstein, for encouraging my independent development as a scientist and for helping me to plan the research, for teaching me to be critical of theories, especially my own, and for teaching me to have the appropriate reverence for data, and for an expert introduction to Italian cuisine.

I would also like to thank my extended family for their encouragement and faith in me and my work. Special thanks are due to my wife, Barbara, whose sense of humor and enthusiasm for our lives together made the graduate years an enjoyable adventure.

ABSTRACT

We have used the heat pulse technique to study phonon reflection from sapphire-vacuum and sapphire-liquid helium interfaces. The high resolution data presented here show more structure than has been observed in previous experiments of this type.

In order to interpret the complex time-of-flight spectra, the problem of the reflection of elastic waves in an anisotropic medium is analyzed in detail. The analysis shows that there are, in general, nine phonon reflection processes, each with a different time of flight, which transfer energy from heater to detector via a single reflection. Iterative computer calculations are necessary to establish the trajectory of energy flow and the arrival time for each channel. The agreement between calculated and experimentally observed times of flight is very good.

Although the sharp features in the reflection signal due to specular ($k_{||}$ conserved) processes can be explained using anisotropic elastic theory, approximately half the energy which reaches the detector arrives via non-specular channels. The non-specular scattering, which may be due to surface roughness, gives rise to broad features in the signal. The main difference between crystal-vacuum and crystal-helium reflection signals is that the non-specular signal is much smaller for the helium covered surface. In contrast to previous works, we find that the specular signal is not affected by helium. Apparently, the non-specular processes are involved in the anomalous Kapitza conductance.

In some crystallographic orientations of heater and bolometer, the non-specular signal is particularly large. The orientational dependence of the diffuse scattering is due to the extreme anisotropy of energy flow in crystals, an effect which is known as phonon focusing. We develop a new method of analyzing phonon focusing based on an asymptotic analysis of the phonon Green's function. Geometric arguments are used to show that certain singularities in the acoustic field called caustics can be expected in most crystals. The general features of caustics can be predicted using results from mathematical catastrophe theory. The caustics in sapphire were located by numerical calculation, and used to explain the results of several experiments.

TABLE OF CONTENTS

CHAPTER ONE: INTRODUCTION

It has been known for more than thirty years that heat transport across a solid-liquid helium boundary is ten to one-hundred times more efficient than predicted by theory. Experimentally, one observes that a solid immersed in liquid helium cools off orders of magnitude faster than expected. This large discrepancy between theory and experiment is a classical problem of low temperature physics known as the Kapitza problem, and is the primary motivation for the work of this thesis.

This puzzle is particularly intriguing because the physics of heat transport in other situations is well understood. The theory of liquid helium is highly developed and the thermal properties of liquid helium are perhaps the best characterized of any substance. Similarly, thermal conduction in solids, particularly at low temperatures, is well described by standard theories. Nevertheless, hundreds of experimental and theoretical investigations[1,2,3] have failed to elucidate the physics of the processes which contribute to the anomalously high conductance at a solid-helium interface.

The history of this subject began in 1971 when Kapitza[4] noticed a peculiar effect while investigating the thermal conductivity of superfluid helium. Careful measurements revealed that there appeared to be a temperature discontinuity at the interface of a heated solid in contact with a helium bath. This was a remarkable result since the boundary conditions for the equations of diffusive heat flow require a continuous temperature distribution even across an interface where the thermal

conductivity changes discontinuously. This effect was phenomenologically described by introducing a thermal boundary resistance R_k, the Kapitza resistance.

The physical mechanism of the Kapitza resistance remained obscure for several years after the initial experiments, although it was thought to be related to the peculiar thermal properties of superfluid helium. It was eventually realized, however, that the equations of diffuse heat flow were not strictly valid very close to an interface. In particular, conservation of energy and momentum of the thermal carriers cannot be accounted for in a theory which characterizes a medium only by a mean free path and an average velocity. As pointed out by Khalatnikov,[5] energy is transported by phonons which impinge on an interface and are either reflected or transmitted with probabilities that can be calculated using classical continuum mechanics. Because the acoustical properties of liquid helium and any solid are very different, most of the phonons which reach a helium interface are reflected; it is the discontinuity of the acoustical properties which gives rise to the temperature discontinuity. The same reasoning shows that this thermal boundary resistance is not peculiar to helium, but can be expected at any interface between dissimilar materials.

The phonon picture clarifies the origin of the temperature discontinuity and thus resolves the original "Kapitza problem." Despite this progress, the detailed quantitative calculations by Khalatnikov[5] in 1952 introduced a new difficulty because the theoretical values of the thermal boundary resistance for solid-liquid helium interfaces were at least an order of magnitude larger than values obtained from experiment.

Thus the Kapitza problem, in its modern formulation, is not concerned with the existence of the thermal boundary resistance, but rather with the explanation of why it is not much larger than it is.

Since the theory developed by Khalatnikov, known as the acoustic mismatch model, is the basis of our (admittedly inadequate) understanding of heat transport across an interface and since most modern efforts have been directed at reconciling experimental results with versions of this model, it is worth discussing in more detail.

The Acoustic Mismatch Model

The theory of Khalatnikov assumes that the essential physics of the transport process can be understood by using continuum mechanics to analyze the reflection of an elastic wave at the interface separating an isotropic solid and an ideal fluid. The use of continuum mechanics is justifiable because the wavelength of thermal phonons at 1 K in a solid is typically 300 nm while in the helium it is 15 nm. In both cases the phonon wavelength is much longer than the interatomic spacing.

The system of incident, reflected and transmitted waves at a solid-liquid interface must satisfy not only the appropriate wave equations of elastic theory and fluid mechanics, but also certain boundary conditions. If the displacement field in the fluid and the solid are denoted by $\vec{u}_f$ and $\vec{u}_s$, respectively, then the condition that solid and fluid remain in contact is that

$$u_f \cdot \hat{n} = u_s \cdot \hat{n} \tag{1.1}$$

at the interface where $\hat{n}$ is a unit vector normal to the boundary.

Only the normal component of the displacement must be continuous, since a fluid with zero viscosity can slip across a solid moving parallel to itself. The condition that the stress be continuous across the boundary is given by

$$\sigma^{s}_{ik}\, n_k = \sigma^{f}_{ik}\, n_k \tag{1.2}$$

where σ^{s}_{ik} and σ^{f}_{ik} are the stress tensors in the solid and fluid, respectively. The displacement and stress can be expressed in terms of the various wave amplitudes. Equation (1.1) represents one constraint on these amplitudes while equation (1.2) represents three conditions. For a given incident wave from the solid, these four equations determine the amplitude of the longitudinal wave transmitted into the liquid and the amplitudes of three waves reflected back into the solid, of which two are transverse and one is longitudinal.

Although the computation of the reflection coefficients from these equations is algebraically complicated, the fact that most of the phonons incident on a solid-helium boundary will be reflected can be explained using a few qualitative arguments. As in the more familiar case of the reflection of electromagnetic waves, the translational invariance of a planar interface implies that the parallel component of the k vector of all the waves which take part in the reflection process must be equal to the parallel component of the incident wave k vector, $k^{in}_{||}$. This is simply a statement of Snell's law, but in the acoustic case the effects can be quite spectacular. For the same phonon frequency ω, the magnitude of the k vector $|k| = \omega/c$ is approximately 20 times larger in helium than

in a solid because of the large difference in c, the speed of sound. This means that there is a critical angle in the helium of approximately 3°; i.e., phonons from the helium with angle of incidence greater than 3° suffer total internal reflection so no energy transport across the interface results from these processes. Conversely, phonons incident from the solid side can only radiate phonons into a cone in the helium with a half-angle of 3°. Conservation of parallel momentum severely restricts the phase space available for transport processes.

A complication which is not present in the electromagnetic case is that the solid supports both longitudinal and transverse waves which for many solids have sound speeds which are approximately related by $c_t = (c_\ell/\sqrt{3})$ (stability of the solid requires $c_\ell > c_t$). Since the density of states goes as $1/c^3$ and there are two transverse modes, there are ten times as many transverse phonons in the solid as longitudinal, and 85% of the energy flux which reaches the interface is in the form of transverse phonons. Because the liquid is assumed to have zero viscosity, however, the coupling of the transverse modes is very poor. At normal incidence, a transverse phonon from the solid is totally reflected.

These qualitative considerations suggest that the mechanical coupling between a solid and an ideal fluid is rather weak, and detailed calculations show that this is particularly true for helium. Using equations (1.1) and (1.2), the energy reflection coefficients for the various phonon polarizations incident from the solid may be computed, as outlined in reference 6. The polarizations may be conveniently described using notation from the seismological literature as longitudinal (L), transverse with polarization in the plane of incidence, or shear vertical

(SV), and transverse with polarization perpendicular to the plane of incidence, or shear horizontal (SH). If the material properties can be described by the density, ρ_ℓ, and speed of sound in the liquid, c, and the density ρ_s, transverse speed of sound c_t and longitudinal speed of sound c_ℓ in the solid, the reflection coefficients labeled by the incident polarizations are[6]

$$R_L = \frac{c \cos\theta^2 \, 2Z_1}{c_\ell \cos\theta \, Z + Z_t \sin^2 2\theta^{SV} + Z_1 \cos^2 2\theta^{SV}} \tag{1.3}$$

$$R_{SV} = \frac{\tan\theta^2}{2(Z + Z_t \sin^2 2\theta^{SV} + Z_1 \cos^2 2\theta^{SV})} \tag{1.4}$$

$$R_{SH} = 1.0 \tag{1.5}$$

where the acoustic impedance are given by

$$Z = \frac{\rho_\ell c}{\cos\theta} \quad , \quad Z_1 = \frac{\rho_s c_\ell}{\cos\theta^2} \quad , \quad Z_t = \frac{\rho_s c_t}{\cos\theta^{SV}}$$

θ, is the angle from the normal of the k vector of the phonon in the liquid, while θ^2 and θ^{SV} are incidence angles of the longitudinal and shear vertical phonons in the solid. If we consider the most efficient transport process, a longitudinal phonon at normal incidence, and substitute the typical values ρ_s = 4.0 gm/cm^3, c_t = 5000 m/sec, c_ℓ = 9000 m/sec, into equation (1.3), the reflection coefficient is R_L = 0.995. Note also that the SH phonons have reflection coefficients of unity at all

angles of incidence, and that none of the reflection coefficients depend in any way on phonon frequency.

Khalatnikov used the phonon reflection model to calculate the Kapitza resistance explicitly in terms of material parameters. The basic idea of the calculation is to compute the net heat flux per unit area $\dot{Q}$ in terms of the temperature difference ΔT between solid and liquid and then to use the relationship

$$\dot{Q} = \frac{\Delta T}{R_k} \tag{1.6}$$

to define the Kapitza resistance R_k. If the solid has temperature T_s, the number of phonons with polarization α which hit the surface from the solid per unit time and per unit area is

$$\frac{\pi^2 k_B^4 T_s^4}{120 \hbar^3 c_\alpha^2} \tag{1.7}$$

where k_B is Boltzman's constant. The heat flux out of the solid $\dot{Q}_{s\to\ell}$ is a product of an angular average phonon energy transmission coefficient and the rate that phonons reach the wall:

$$\dot{Q}_{s\to\ell} = \sum_\alpha \frac{\pi^2 k_B^2 T_s^4}{120 \hbar^3 c^2} \int [1 - R_\alpha(\theta)] \cos\theta \, d(\cos\theta)$$

$$= \frac{\pi^2 k_B^4 T_s^4}{120 \hbar^3} \sum_\alpha \frac{A_\alpha}{c_\alpha^2} \tag{1.8}$$

where α ranges over L and SV. A similar expression holds for the heat

flux from the liquid into the solid $\dot{Q}_{\ell \to s}$:

$$\dot{Q}_{\ell \to s} = \frac{\pi^2 k_B^4 T^4}{120 \hbar^3} \frac{B}{c^2} \tag{1.9}$$

where T_ℓ is the temperature of the liquid,

$$B = \int [1 - R(\theta)] \cos\theta \, d(\cos\theta) \tag{1.10}$$

and $R(\theta)$ is the reflection coefficient of longitudinal phonons from the liquid side. When $T_\ell = T_s$, the net heat flux $\dot{Q}_{\ell \to s} - \dot{Q}_{s \to \ell}$ is zero, so

$$\sum_\alpha \frac{A_\alpha}{c_\alpha^2} = \frac{B}{c^2} \tag{1.11}$$

This is an algebraic relationship which expresses the microscopic reversibility of the phonon reflection process and is valid at all temperatures. If $T_s - T_\ell = \Delta T$ is small, one can make the approximation

$$T_s^4 - T_\ell^4 = 3T_s^3 \Delta T \tag{1.12}$$

The net heat flux $\dot{Q}$ can then be written

$$\dot{Q} = \frac{\pi^2 k_B^4 T_s^3}{40 \hbar^3} \Delta T \sum_\alpha \frac{A_\alpha}{c^2} \tag{1.13}$$

The integrals which define the angular-average reflection coefficients A_α are rather tedious, but were carried out by Khalatnikov. The final result is

$$\dot{Q} = \frac{16\pi^5}{15} \frac{\rho_\ell c}{\rho_s} \frac{k_B^4 T^3}{(2\pi\hbar c_t)^3} F \Delta T \tag{1.14}$$

or

$$R_k = \frac{15 h^3 \rho_s c_t^3}{16\pi^3 k_B^4 \rho_\ell c F} \frac{1}{T^3} \tag{1.15}$$

where F is a number of order unity.

The most direct method of measuring the Kapitza resistance is to produce a known steady heat flux across a solid-liquid helium interface and simply measure the temperature discontinuity ΔT. This has been done for many materials, but the available data are not self-consistent in the sense that values obtained on different samples or in different laboratories often differ by a factor of two. The experimental difficulty of measuring the temperature at the interface from the solid side and estimating the effective surface area of a sample are probably the main cause of the discrepancies. Nevertheless, the results of many steady heat flux experiments can be summarized by saying that although the T^{-3} behavior expected on grounds of simple kinetic theory is approximately obeyed, the experimentally measured numerical value of the Kapitza resistance is consistently lower than predicted by equation (1.15), usually by more than a factor of ten. For example, sapphire, the solid used in all the experiments reported in this thesis, the measured Kapitza resistance is $R_k^{meas} = 44/T^3$ (cm^2 K/W) while the acoustic mismatch value is $R_k^{AM} = 9800/T^3$ (cm^2 K/W).[1] Acoustic mismatch fails equally for metals, insulators and

superconductors. Perhaps the only real success of the theory is the T^{-3} dependence which is found in most experiments. The strong temperature dependence means that the acoustic mismatch mechanism becomes negligible at high temperatures, but conversely, it is very effective in the millikelvin range. Overcoming the Kapitza resistance is one of the main problems of very low temperature technology.

The clear conflict between the acoustic mismatch theory and the experimental results stimulated considerable work in the field which eventually led to an understanding of some additional subtleties of the anomalous Kapitza resistance. Although some progress has been made, the basic mechanism which overcomes the restrictions on heat flow imposed by acoustic mismatch is still not known. Some of the additional findings are:

1. the acoustic mismatch theory seems to work for interfaces between classical solids;[7,8,9]
2. superfluidity does not play a role; the Kapitza resistance is continuous through T_λ.[10] This is rather surprising since all other thermal properties of liquid helium change drastically at the lambda transition;
3. quantum systems such as solid or liquid ^4He, solid or liquid ^3He, solid H_2 and D_2 all exhibit anomalous Kapitza resistance;[9,11,12,13]
4. above 1 K the Kapitza resistance of a solid interface with either solid or liquid ^3He or ^4He is identical;[12]
5. phonons of frequency below 10 GHz seem to obey acoustic mismatch theory.[14]

These results confirm that the acoustic mismatch analysis is deficient in some serious way, and suggest that the error may lie in the calculation of the reflection coefficients $R_\alpha(\theta)$. Unfortunately, only an angular and polarization average of the $R_\alpha(\theta)$ is determined by measuring the Kapitza resistance in steady state heat flux experiments so it is impossible to find out which phonon processes are responsible for the efficient energy transport using this method.

Ballistic Phonon Reflection

In the early 1970's a new experimental technique was developed[15,16] which was designed to measure directly the reflection coefficient of phonon pulses which propagated ballistically though a crystal. This method was adopted for the studies reported in this thesis; a schematic form of the apparatus is shown in Figure 1.1. A pure, low defect density, single crystal of an insulator such as silicon, LiF or sapphire is equipped on one side with a phonon generator and detector made from evaporated

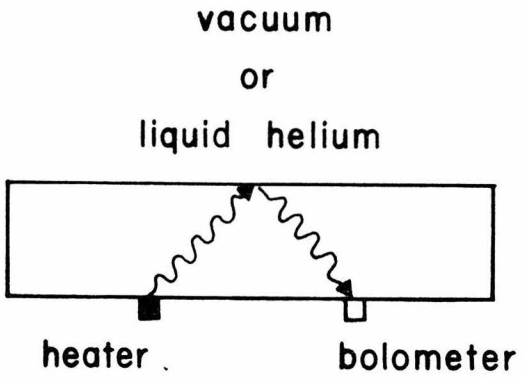

Figure 1.1. Schematic diagram of ballistic phonon reflection experiment.

metallic films. The opposite crystal surface is initially a vacuum interface, but helium can be introduced to form a liquid film of thickness varying between a sub-monolayer to bulk liquid. Because the mean free path of phonons in a dielectric crystal at helium temperatures is many centimeters, a phonon pulse produced at the generator travels ballistically at the speed of sound to the interface, where some fraction is reflected back to the detector. By comparing the reflection signal from a crystal-vacuum interface to the signal from a crystal-helium interface, the reflection coefficient at the crystal-helium interface can be deduced. Moreover, since the position of the generator and detector determine the angle of incidence of the detected phonons, and the flight time of the longitudinal and transverse polarizations are different, the method can be used to measure $R_{\alpha}(\theta)$ for a known phonon polarization and angle θ.

A reflection signal which was obtained in the earlier versions of our experiment, which is typical of the data reported by previous investigators, is shown in Figure 1.2. The detector signal as a function of time after the phonons have been emitted from the heater shows three prominent peaks. The first peak is due to the arrival of the fastest phonons; i.e., the longitudinal phonons. The third peak, due to the transverse phonons, is considerably larger because of the larger density of states for transverse modes. The middle peak is due to processes which involve one longitudinal and one transverse phonon, and thus have an intermediate time-of-flight. The upper curve represents the signal from a crystal-vacuum interface, the lower curve is the signal from a crystal-helium interface. The reflection coefficients deduced from such measurements

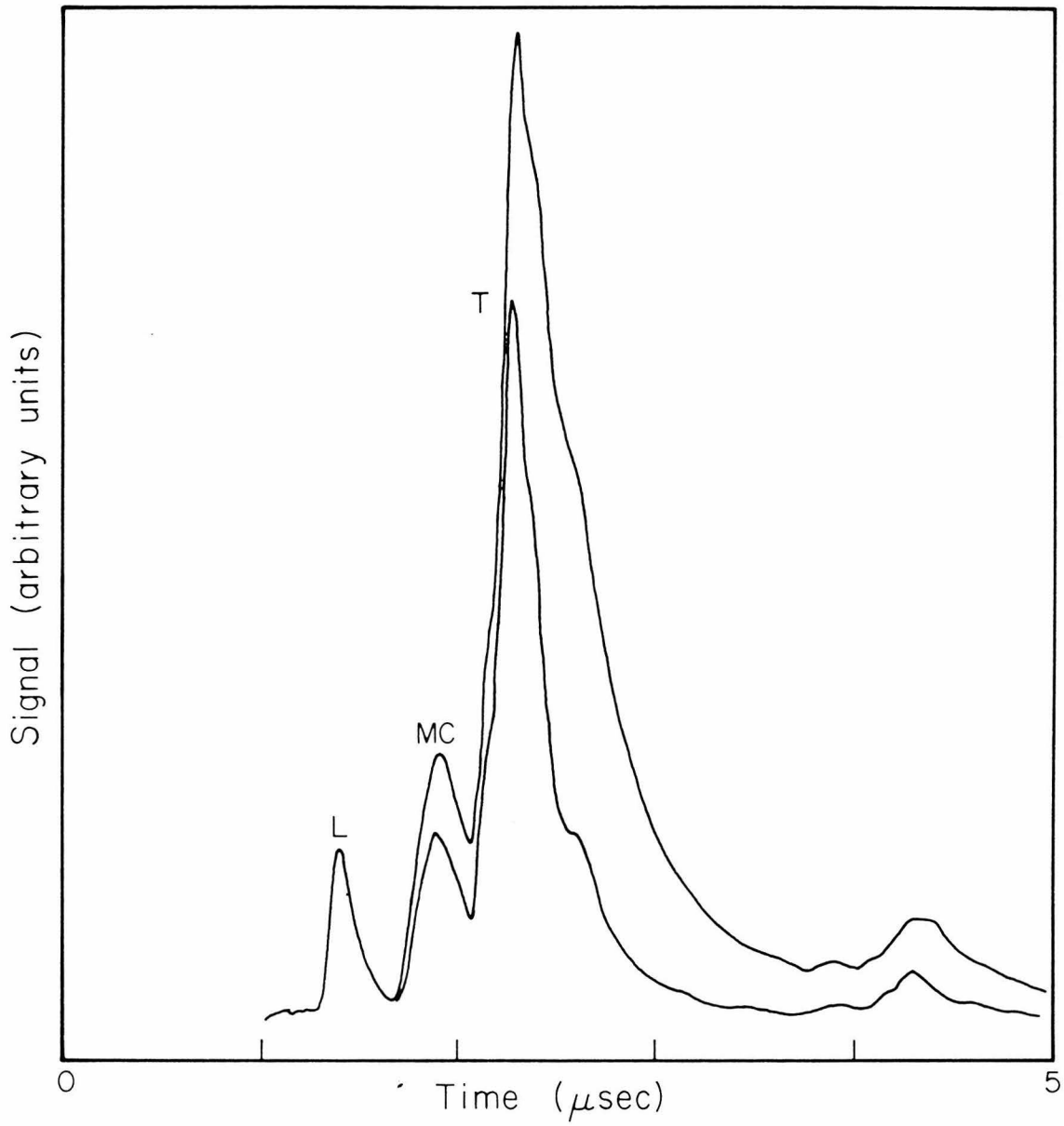

Figure 1.2. Typical phonon reflection signal, showing peaks corresponding to longitudinal, transverse and mode conversion processes. Upper curve is the reflection signal from a vacuum interface, while lower curve is the signal from a crystal-liquid helium interface.

by previous workers lie in the range 0.8-0.3 rather than 0.995 expected on the basis of acoustic mismatch theory, demonstrating once again that the theory is inadequate. The substantial absorption of the transverse mode was particularly paradoxical since elastic theory predicts no coupling to a fluid. An additional puzzling fact discovered in these experiments is that the absorption into helium is as effective for a film only three statistical atomic layers thick as for bulk liquid.[15,16]

These findings and the acoustic mismatch theory worked out by Khalantnikov and others forms the historical background for this thesis. After repeating the experiments of Guo and Maris,[10] several scientific questions presented themselves: Why is the absorption of transverse phonons so effective? Do SH and SV couple equally? Although elastic theory fails to give accurate reflection coefficients, does $R_\alpha(\theta)$ vary in a reasonable way as a function of θ? More particularly, can elastic theory at least describe the reflection processes from the crystal-vacuum interface, including mode conversion processes? How does the reflection coefficient depend on the parameters of film thickness, ambient temperature and gas pressure? (The interpretations offered by previous investigators[10,16] are in direct conflict.)

The attempt to answer these questions led to an improvement in experimental technique as well as a more precise theoretical understanding of the phonon reflection process. The main contributions are outlined below.

1. The apparatus of Guo and Maris[10] was made more flexible by using a superconducting bolometer biased in a magnetic field.

This enlarged the useful range of the bolometer to include the entire temperature range from the T_c of tin to the lowest temperatures obtainable in the apparatus, which was approximentely 1.4 K. A technique was developed to control the helium film thickness of the reflection surface.[17] The method utilizes previous work on the helium-Grafoil system and enables pressures as low as 10^{-15} torr to be measured in situ. By using shorter phonon pulses and much smaller phonon generators and detectors, the time-of-flight resolution was increased by a factor of twenty over previous experiments. The details of the experimental apparatus are described in Chapter Two.

2. Reflection experiments performed with higher resolution revealed a considerably more complex structure than the three peak signal of Figure 1.2. Isotropic elastic theory was inadequate to explain even the crystal-vacuum interface data. An analysis of the phonon reflection process which included the effects of crystal elastic anisotropy revealed complexities of the problem which had not been previously appreciated. Iterative computer calculations were used to predict phonon trajectories and times-of-flight in various crystallographic directions. The results of these calculations and the comparison to experimental data are presented in Chapter Three.
3. Although anisotropic elastic theory successfully predicts the time-of-flight for the various phonon reflection processes,

the observed pulse shapes of the reflection signal cannot be accounted for assuming only specular reflection ($k_{||}$ conserved) from a flat surface. Nonspecular processes appear in the data as "tails" which follow the sharp pulse due to specular processes. The high resolution data show that the nonspecular processes account for most of the anomalous coupling to helium. In an attempt to estimate the magnitude of the nonspecular scattering, it was necessary to compute the acoustic intensity along a given direction in the crystal; this involves the theory of phonon focusing developed by Maris.[18,19] This theory was found to predict unphysical infinities in acoustic intensity in certain special directions, known as caustics. Accurate formulas for the intensity along caustics were found and classified in terms of formal catastrophe theory. The computed position of the caustics was used to explain the spatial dependence of nonspecular scattering. The analysis required to classify and locate caustics, as well as the comparison with experimental data are presented in Chapter Four.

7. The experimental results are briefly summarized in Chapter Five. The main area of disagreement between theory and experiment is the behavior of nonspecular scattering. Several areas for future work are suggested which may help to reconcile the difference.

CHAPTER TWO: APPARATUS AND EXPERIMENTAL METHODS

Phonon Generation and Detection

Previous investigators[15,16] have used both tunnel junctions and superconducting bolometers as efficient detectors of phonons in the 100-1000 GHz frequency range. Although tunnel junctions have been used as frequency tunable phonon generators, this advantage is partially offset by uncertainties in the elaborate theory of nonequilibrium superconductivity which is required to deduce the emitted phonon spectrum. My original intention was to use a generation and detection system based on junctions, and after considerable effort, I finally succeeded in fabricating tin and lead junctions of acceptable quality. It was soon decided, however, that the difficulty of fabrication and the fragility of these devices outweighed the potential advantages of frequency resolution, and all of the experiments reported in this thesis used broad-band superconducting bolometer detectors, and resistive heater generators which are thought to produce a black-body phonon frequency spectrum.

The principle of operation of the superconducting bolometer is very simple. Above its transition temperature T_c, a superconducting strip has an electrical resistance R_N characteristic of a normal metal; below T_c the electrical resistance is zero. Because of impurities and internal strains, the transition to the superconducting state is not infinitely sharp, but typically has a width of a few milli-degrees, as shown in Figure 2.1. If the ambient temperature is in the middle of the transition region, a very small change in the local temperature ΔT

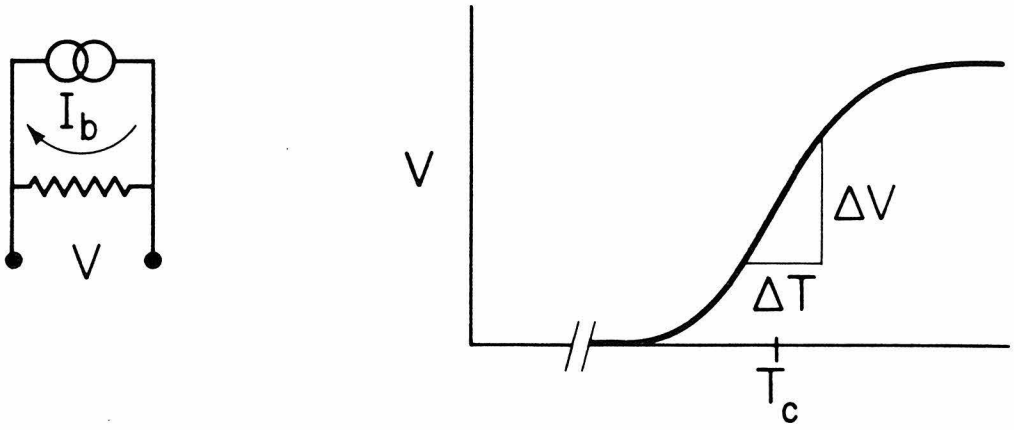

Figure 2.1. Schematic plot of the voltage as a function of temperature for a fixed bias current I_b for a superconducting bolometer. A phonon pulse increases the temperature by ΔT and causes a voltage change ΔV.

produces a large change in the voltage ΔV. By carefully measuring the changes in voltage, the superconducting strip serves as a thermometer with a sensitivity of micro-degrees. The useful range is only a few milli-degrees around the thermodynamic critical temperature T_c, but the device can be operated at any lower temperature by suppressing the transition temperature in a magnetic field. The characteristics of a typical bolometer are presented as a plot of voltage drop for a bias current of 3 ma as a function of temperature for several values of the magnetic field in Figure 2.2. The sensitivity of the bolometer is measured by the value of $(\partial v/\partial T)_{I_b}$.

The requirements of a bolometer in a phonon reflection experiment are that the active element be well localized spatially, the thermal response time be small compared to the duration of a phonon pulse, and that the voltage signal due to a phonon pulse be comparable to the rms noise voltage of the amplification electronics, which is approximately

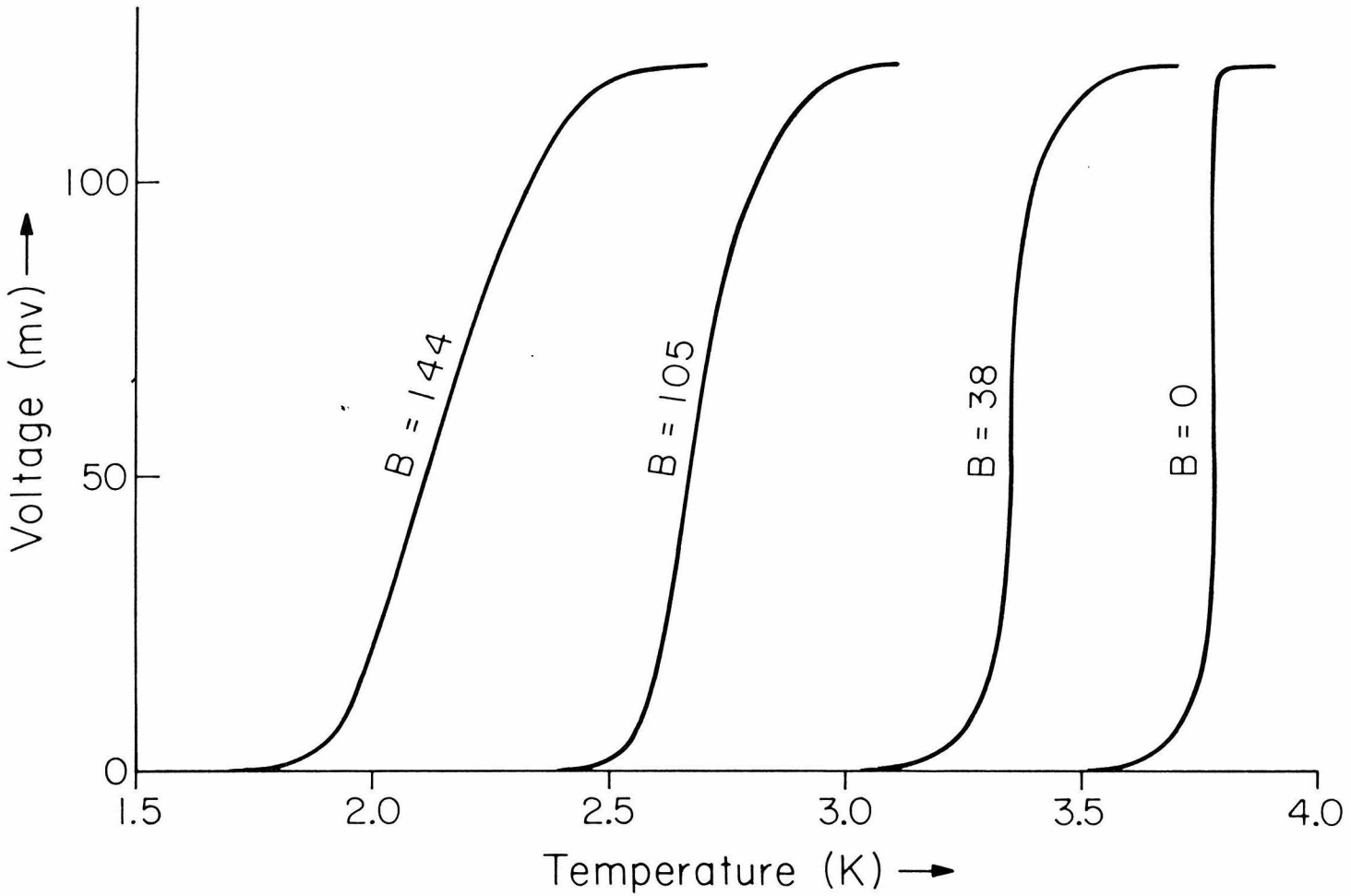

Figure 2.2. Voltage vs. temperature characteristics for a typical tin bolometer. I_b = 3 ma. Values of the external magnetic field B are given in gauss.

50 μV. The thermal response time is governed by the total mass of superconductor, so it is advantageous to make the device as small as possible. This is accomplished by using evaporated films of thickness 2000 Å. A thin conducting path in a serpentine shape is cut into the film with a razor blade under a microscope. The total area of the active part of the bolometer can be made as small as 0.4 x 0.4 mm^2 using this technique. Electrical connections were made using pressed indium contacts.

In principle, the sensitivity of the bolometer is optimized by making $(\partial v/\partial T)$ and therefore the normal state resistance R_N as large as possible. R_N can be increased by decreasing the film thickness or by making the conducting path longer. In practice it was found that increased sensitivity could only be obtained at a sacrifice in thermal stability and reliability of performance; bolometers with room temperature resistance $R_{300} \simeq 200\ \Omega$ and liquid helium temperature resistance $R_4 \simeq 20\ \Omega$ seem to represent a suitable compromise. Although the operating temperature could be adjusted with the magnetic field, all the experiments reported here were conducted at T = 2.05 K with a field of approximately 150 gauss. It was found that stability of the bolometers was greatly improved if they were run in a superfluid bath. In a normal bath, the bolometer signal was affected by bubbles and convection in the fluid and was very sensitive to mechanical vibrations of the dewar.

The heaters were made from 1000 Å thick films of aluminum from which a serpentine conducting path was cut. The heaters used in the experiments were designed to have a resistance at helium temperatures of approximately 50 Ω to match the impedance of the pulse generator and coaxial cables.

Crystals

All of the crystals used in this investigation were synthetically grown crystals of Al_2O_3, or sapphire, which were bought from the Union Carbide Company. Sapphire was originally chosen for these experiments because large, relatively inexpensive, high quality single crystals were readily available and because sapphire is chemically inert, mechanically strong and is considered to be one of the most nearly elastically isotropic cyrstals.[20] Because of the supposed near isotropy, the initial phonon reflection experiments were performed with unoriented crystals. The corresponding calculations using isotropic elastic theory were performed using the average sound speeds $c_\ell = 1.1 \times 10^6$ cm/sec and $c_t = 0.65 \times 10^6$ cm/sec. It soon became apparent, however, that elastic anisotropy was an important effect and the elastic properties could only be described using the fourth rank elastic tensor, $c_{ijk\ell}$.

Sapphire is a trigonal crystal, so the elastic tensor $c_{ijk\ell}$ has six independent elements (see references 21 and 22 and Chapter Three for more details). Rather than specifying the 81 components of the elastic tensor, elastic constants are usually presented in the form of a symmetric 6 x 6 matrix c_{mn} (which is <u>not</u> a tensor). The independent elements of the matrix of elastic constants for synthetic sapphire are shown in Table 2.1.[23]

Table 2.1. Elastic constants of sapphire (in 10^{11} newtons/m^2).

c_{11}	c_{33}	c_{44}	c_{12}	c_{13}	c_{14}
4.968	4.981	1.474	1.636	1.109	-0.235

The remaining elements of the c_{mn} are dictated by the crystal symmetry. For a trigonal crystal, the elements are:

$$c_{22} = c_{11} \qquad c_{23} = c_{12} \qquad c_{55} = c_{44}$$

$$c_{56} = c_{14} = -c_{24} \qquad c_{66} = 1/2\,(c_{11} - c_{12})$$

with $c_{ij} = c_{ji}$. All other elements are equal to zero. The elastic tensor $c_{ijk\ell}$ may be constructed from these elements by associating each subscript of the matrix c_{mn} with a pair of subscripts of the tensor $c_{ijk\ell}$ with $m \rightarrow i,j$, $n \rightarrow k,\ell$, according to the following scheme:

$1 \rightarrow 1,1$	$4 \rightarrow 2,3 = 3,2$
$2 \rightarrow 2,2$	$5 \rightarrow 1,3 = 3,1$
$3 \rightarrow 3,3$	$6 \rightarrow 2,1 = 1,2$

The reason for these peculiar rules is mainly historical; the terminology for the elastic properties of crystals was developed before the invention of tensor notation.

The elements of the c_{mn} and the $c_{ijk\ell}$ depend on the coordinate system used to express them, and a specific choice of coordinates has been

made which corresponds to the values given in Table 2.1. The coordinate system is specified in terms of the crystal symmetry axes which are shown in Figure 2.3. The point group of sapphire is $\bar{3}$ m. The crystal has one three-fold rotation axis, which is designated the C axis, and three two-fold rotation axes which are in the plane perpendicular to the C axis and separated by 120°. The canonical rectangular coordinate system with unit vectors $(\hat{x}, \hat{y}, \hat{z})$ is constructed with $\hat{z}$ along the C axis, $\hat{x}$ along a two-fold axis, and $\hat{y} = \hat{z} \times \hat{x}$ to form a right-handed orthonormal basis. This prescription does not define a unique basis, however, because opposite ends of a two-fold axis can be distinguished even though the point group $\bar{3}$ m has a center of symmetry. The arbitrary choice of aligning $\hat{x}$ along the (+) or (-) direction of a two-fold axis changes the sign of some of the elastic constants. Moreover, there is no established convention for making this choice. This confusing and subtle point was not appreciated by the early investigators who measured the elastic constants of sapphire, and conflicting values appear in the literature.[24,25,26]

Reference 23 specifies the choice of orientation of $\hat{x}$ in terms of the X-ray diffraction pattern. Unfortunately, the choice does not affect elements of second rank tensors like the dielectric tensor, so the crystals cannot be oriented by optical measurements. The X-ray analysis required to orient $\hat{x}$ in the same direction as was done in reference 23 is quite difficult, and I could not find a crystallographer who was willing to try. Because exact orientation was difficult and because the choice of direction of $\hat{x}$ did not alter the computed arrival times of reflected phonons (only the intensities are changed) an arbitrary choice was made for the crystals used in the experiment.

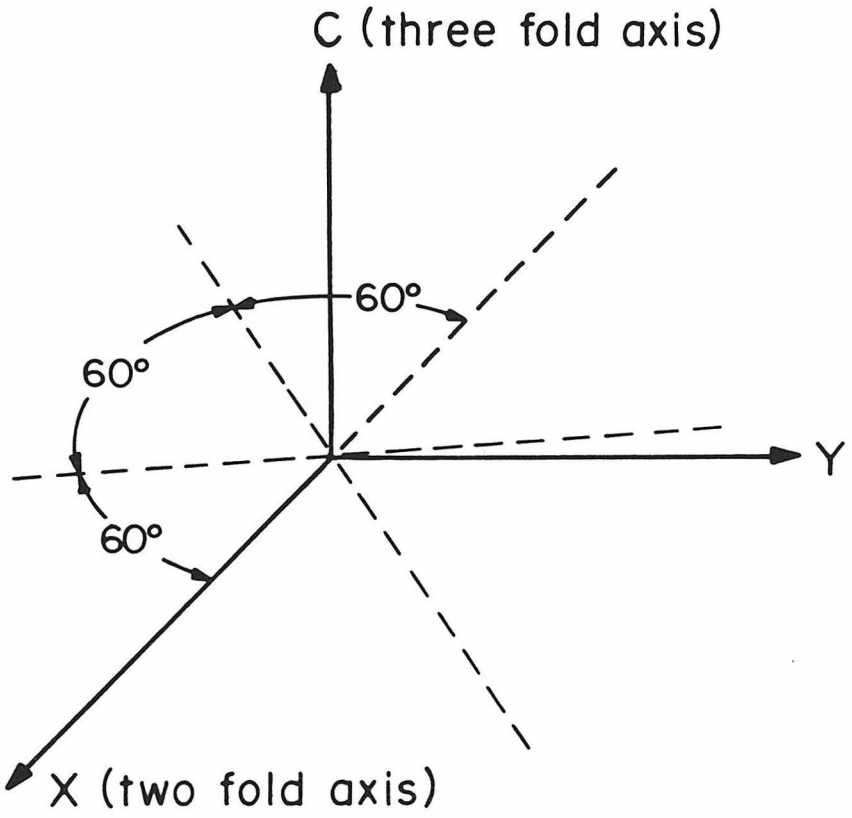

Figure 2.3. Crystallographic axes in sapphire.

Although the condition of the crystal surface is probably very important in phonon reflection experiments,[27] it is also very difficult to evaluate quantitatively. All of the crystals used in the experiments were ordered with the best surface polish provided by the manufacturer which yields a claimed surface roughness of ±1 micro-inch = 25 nm. In some experiments the crystals were cut with a diamond saw and repolished. The process required two days of mechanical polishing with successively finer diamond paste. A final polish with 250 nm grit produced a finish with no scratches observable under a microscope.

Electronics

A schematic diagram of the electronics used in the phonon reflection experiments is shown in Figure 2.4. The heating pulses were typically 35 nsec wide and 5.0 to 10.0 volts in amplitude with a repetition rate of 100 μsec. A few hundred nanoseconds before each heating pulse, an oscilloscope and the boxcar integrator were triggered. A few microseconds after the heating pulse, the reflected phonons reach the bolometer and cause a change in the voltage. The voltage pulse (typical magnitude = 20 μV) is amplified first with a PAR 115 wide band preamplifier and then an HP 461A pulse amplifier for a total gain of 1000. Although the signal can be seen on an oscilloscope, it is deeply buried in noise and the boxcar integrator is necessary to obtain a clean signal. The boxcar is a PAR 160 mainframe with a 162 processor module. For a given integration time and desired resolution, the various boxcar time constants can be chosen to optimize the so-called "signal-to-noise improvement ratio," SNIR. A calculator program was written to do this; typical settings are:

integration time = 5 min

aperture duration = 25 nsec

aperture delay = 5 μsec

mainframe time constant = 0.5 sec

processor module time constant = 10^{-4} sec

SNIR = 2000

The boxcar output could be displayed using an X-Y recorder.

The electrical connections to the heater and bolometer were made using miniature 50 Ω coaxial cable. For the experiments reported in

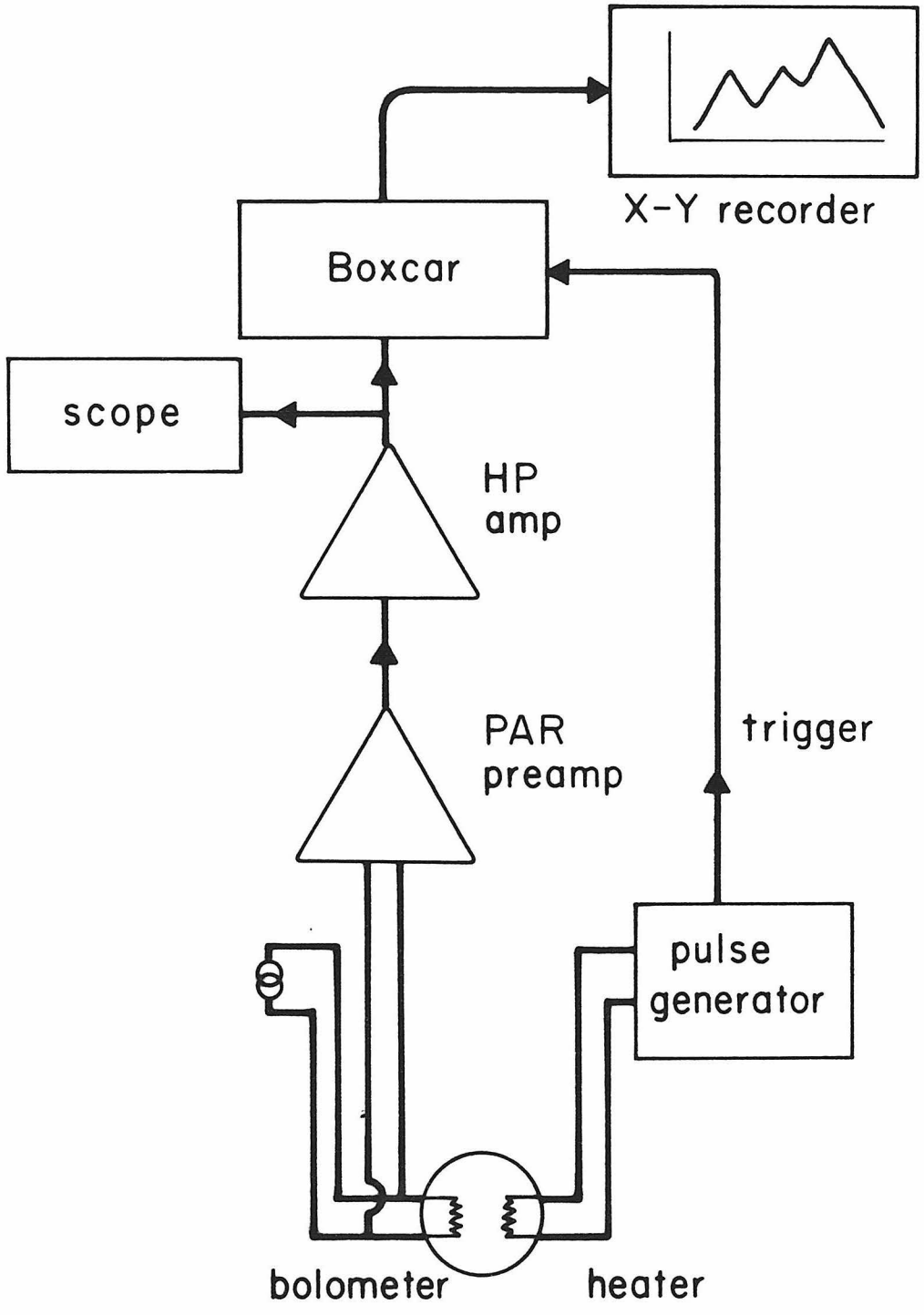

Figure 2.4. Schematic diagram of electronics used in phonon reflection experiments.

Chapter Three which used five heaters, it was necessary to have nine cables which went from room temperature into the helium bath. The heat leak using coax made of copper was too great, so the apparatus was rewired with Uniform Tubes 1/8" stainless steel coax, which worked very well.

A serious problem in the early stages of this experiment was electromagnetic cross-talk between the heater and bolometer circuits. Ideally, the output signal is due only to heating caused by reflected phonons, but in fact a large (50 mV) spike at zero time delay is always observed which is caused by direct coupling of the antennas formed by the heater and bolometer coax. Unless precautions are taken, the circuit may ring for many microseconds and completely swamp the phonon signal. The electromagnetic ringing is strongly affected by the position of all nearby conductors, and their relative potential with respect to ground. After much trial and error, it was found that by floating the heater and bolometer ground shields and connecting them to ground via variable resistors, the ringing time could be reduced to less than 0.5 μsec. One possible explanation of this effect is that the outside conductors of the coax and other metallic components of the apparatus form unterminated transmission lines. These transmission lines are excited by the electromagnetic radiation from the heater pulse. By adjusting the variable resistors for a minimum ringing time, one is presumably finding the characteristic impedence of the transmission lines formed by the coax shields and other conductors in the apparatus.

Vacuum System

In order to measure the effect of helium on the phonon reflection coefficients, it is necessary to calibrate the signal by measuring the vacuum interface reflection coefficients. The vacuum system shown in Figure 2.5 is designed to isolate one side of the crystal from the surrounding helium bath and allow the helium gas pressure on the reflection surface to be controlled in a range from 10^{-15} torr to the saturation vapor pressure.

The vacuum seal between the stainless steel vacuum can and the crystal is made using an indium O-ring, which provides a super leak-tight seal. The only difficulty experienced in using these seals was a tendency for the crystals to chip along the edges as the seal was being tightened. This problem was solved by first using a metal plug the same shape as the crystal to flatten the indium wire and form a smooth indium surface; also, crystals with slightly beveled edges did not chip as readily as crystals with sharp edges. The resulting seals could be reliably cycled many times. The indium adhered to the polished sapphire surface so well that the O-ring usually had to be melted to remove the crystal.

The vacuum can to which the crystal was attached contains approximately 6 grams of Grafoil, a form of exfoliated graphite with a large specific area. The large adsorbtion area of the Grafoil serves as a ballast which allows one to control the helium gas pressure, and therefore the thickness of the liquid helium film which covers the crystal, even for pressures as low as 10^{-15} torr. The calibration of the Grafoil manometer was accomplished by combining the extensive thermodynamic data of previous

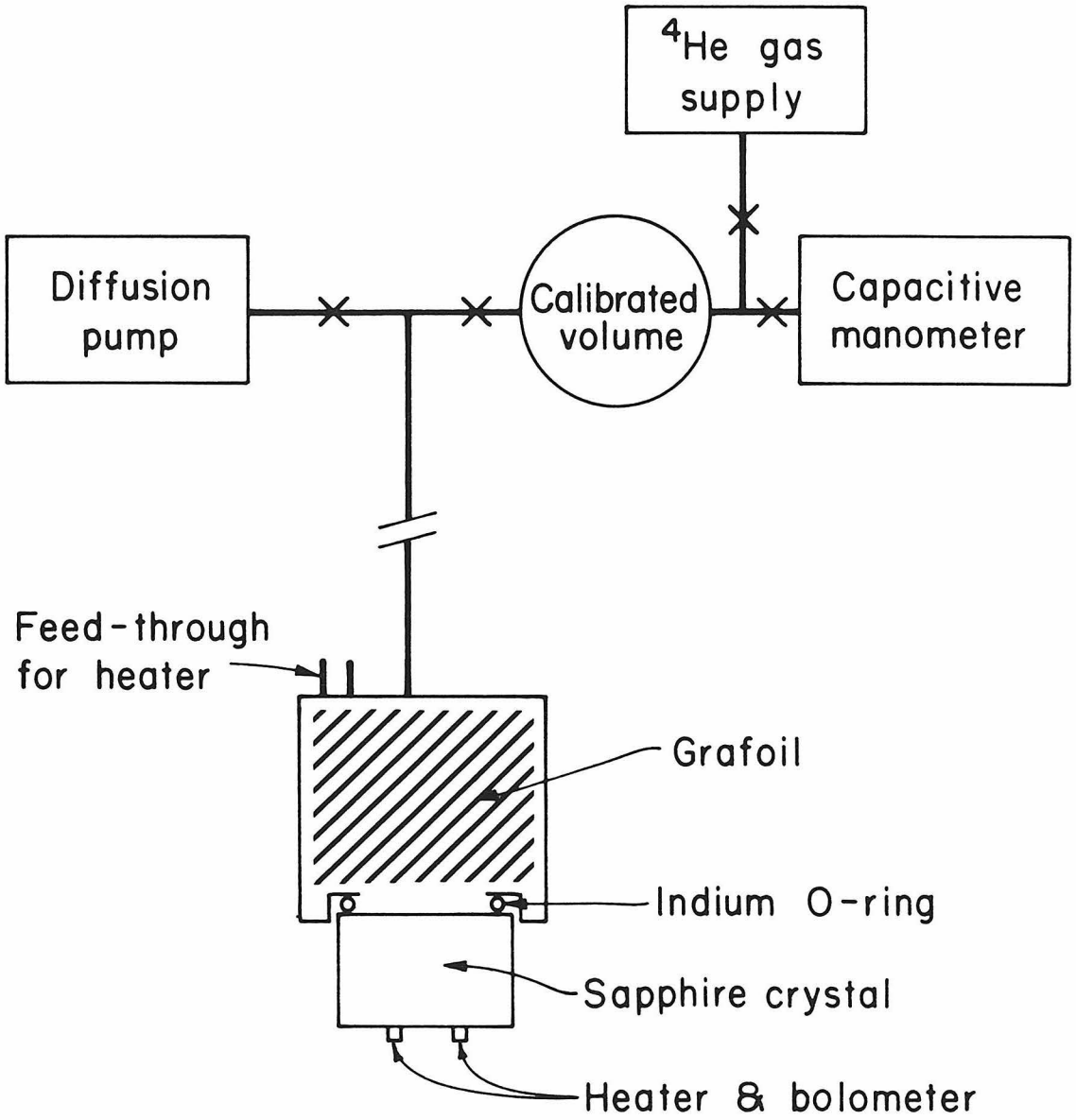

Figure 2.5. Schematic diagram of vacuum system.

investigators[28,29,30] with vapor pressure data obtained using this apparatus. The combined data were sufficient to characterize completely the thermodynamics of the Grafoil-helium system in a certain region of the N-T plane. Once $\mu(N,T)$, the chemical potential of the helium gas as a function of the amount of helium adsorbed N, and temperature T, is known, the pressure in torr is given by

$$P = 155.79\ T^{2.5}\ \exp(\mu/T)$$

where μ is measured in degrees. The technique takes advantage of the fact that even in the region where the pressure is very small and experimentally inaccessible, the heat capacity may be easily measured. Further details are given in a published paper "Control of Ultralow Pressures: An Absolute Thermodynamic Manometer."[17] The Grafoil manometer project was pursued with the intention of carefully studying the phonon reflection coefficients as a function of film thickness, temperature and pressure, but it soon became apparent that the effects of crystal anisotropy had to be understood first; the analysis of this problem is presented in the following chapter.

CHAPTER THREE: ANALYSIS OF PHONON REFLECTION EXPERIMENTS - SPECULAR SCATTERING

The use of the phonon reflection technique to study the Kapitza resistance is based on observing the difference between the reflection signals obtained with crystal-vacuum and crystal-helium interfaces. There has been, however, considerable confusion about how to measure this difference quantitatively. For example, Guo and Maris[15] implicitly use a ratio of peak heights to obtain a reflection coefficient, while Kinder[31] uses a ratio of integrals of the reflection signal with a subtracted background. These definitions are not equivalent and, as illustrated by data presented below, depend on such unlikely parameters as the shape of the crystal. Examination of our early data convinced us that whatever measure of reflection coefficient was to be used, it was essential to understand the background signal; i.e., reflection from a crystal-vacuum interface, before any progress on the problem of coupling to helium and the Kapitza resistance could be made. For this reason, this chapter presents an analysis of elastic, specular ($k_{||}$ conserved) phonon reflection processes from a perfectly smooth crystal-vacuum interface. Since elastic isotropy has been used to analyze previous phonon reflection experiments[15,32] and is used in the acoustic mismatch theory, we first present an analysis based on isotropic elastic theory. Although this analysis can explain some simple features of the experimental results, the details can only be understood in terms of anisotropic elastic theory. Once the vacuum interface reflection processes are properly analyzed, the reflection experiments from a crystal-helium interface can be interpreted much more

intelligently. Much of this chapter is adapted from a published paper "Phonon Reflection at a Sapphire-Vacuum Interface."[33]

Phonon Reflection in an Isotropic Solid

Some of the implications of isotropic elastic theory for transport across an interface were outlined in Chapter One. Here, we wish to apply a detailed analysis of the phonon reflection process, including the dependence on incidence angle and polarization, to the prediction of the experimentally observed reflection signal. We assume that the heater emits phonons with isotropically distributed k vectors and the phonon modes are populated according to their density of states. The isotropic solid is characterized by the longitudinal and transverse sound velocity, c_ℓ and c_t. The polarizations are denoted L, SV and SH, as described in Chapter One.

The laws which govern reflection at a vacuum interface[34] are that the normal stress must vanish

$$\sigma_{ik} m_k = 0 \tag{3.1}$$

where m_k is the normal vector and

$$k_{||}^{inc} = k_{||}^{ref} \tag{3.2}$$

the parallel component of incident and reflected waves must be equal, which is equivalent to Snell's Law. Equation (3.2) is also equivalent to Fermat's principle of least time. In an isotropic solid there are precisely three different types of phonon reflection processes which can

be labeled by the polarization of the incident phonon. These processes are shown in the upper inset of Figure 3.1. Note that SV and L phonons are coupled; a single incident phonon requires two reflected phonons to relieve the stress. Reflection processes which involve a change in phonon polarization are known as mode conversion processes. At normal incidence there is no mode conversion, but as the angle of incidence increases, the amplitude of the mode conversion wave also increases. For example, for a SV wave incident at angle θ_o with amplitude A_{SV}, the reflected L wave has amplitude A_L:

$$A_L = A_{SV} \frac{2\, c_\ell c_t \sin 2\theta_o \cos 2\theta_o}{ct^2 \sin 2\theta_\ell \sin 2\theta_o + c_\ell^2 \cos 2\theta_o} \tag{3.3}$$

where

$$\theta_\ell = \sin^{-1}\left[\frac{c_\ell}{c_t} \sin \theta_o\right] \tag{3.4}$$

and c_ℓ and c_t are, respectively, the longitudinal and transverse sound speeds. Note that as θ_o increases, θ_ℓ will eventually become complex, since $c_\ell > c_t$. Physically, this means that the reflected longitudinal wave is exponentially damped. Since SH waves do not induce a stress normal to the wall, they always reflect without mode conversion.

In order to calculate the arrival time of a phonon pulse at the detector, it is necessary to know the trajectory of the incident and reflected phonons which transfer energy from the heater to the detector. If Fermat's principle is applied to this problem, one obtains a quartic

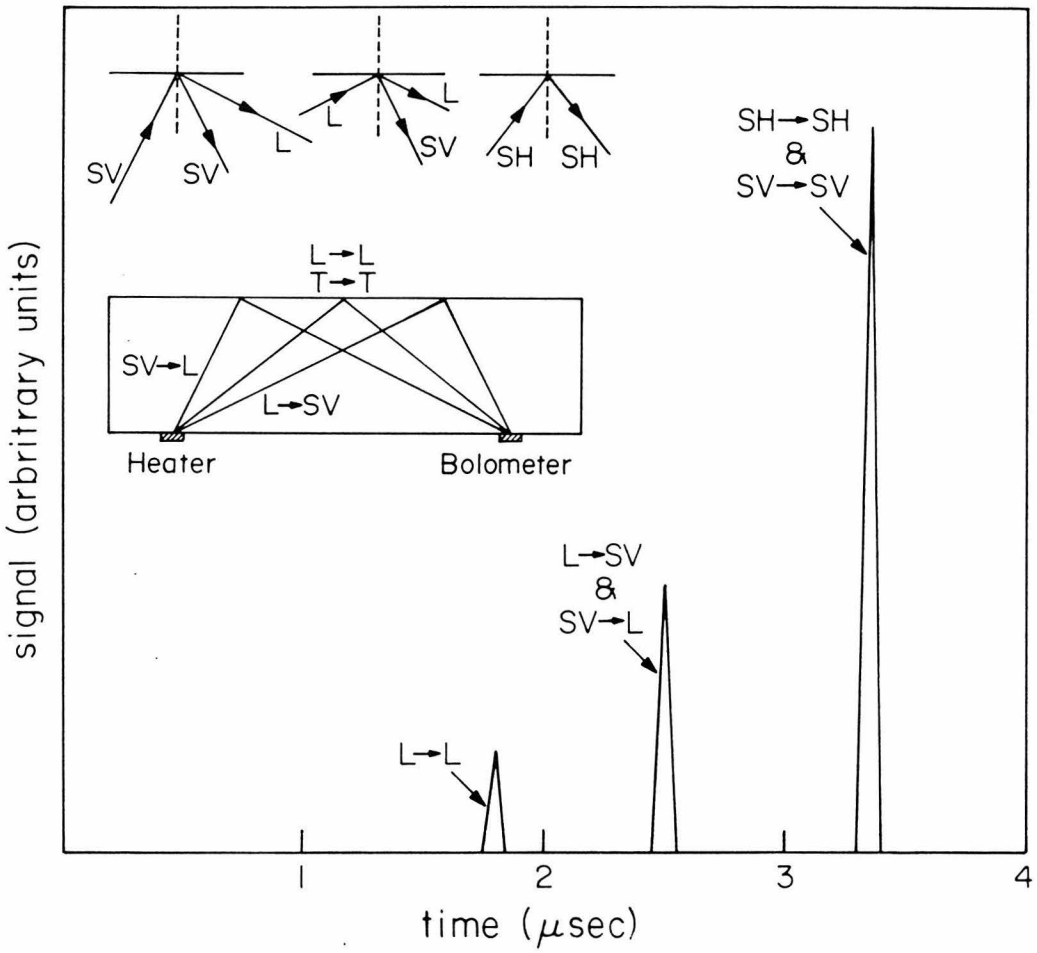

Figure 3.1. Schematic diagram of bolometer signal assuming an isotropic solid similar to sapphire. The calculation is done for a sample thickness of 6.5 mm and a heater-bolometer separation of 6.7 mm. The experimental signal for the same geometry in real (anisotropic) sapphire is shown in Figure 3.4.

equation, which can be easily solved numerically. Two of the four solutions are simply trajectories with equal angle of incidence and reflection that do not involve mode conversion. In addition, there are two trajectories which do involve mode conversion, as shown in Figure 3.1. Although the time-of-flight for both of these trajectories is the same in the isotropic case, they are not entirely equivalent. The SV → L channel dominates because the density of states of SV phonons is larger.

Qualitatively, isotropic elastic theory predicts the following results for phonon reflection experiments:

1. if heater and bolometer are very close together, the incidence angle of all the specular channels is close to zero, and there is no mode conversion. One should observe only two peaks due to longitudinal and transverse phonons;
2. at finite separation between heater and bolometer, one expects three peaks. The middle mode conversion peak increases monotonically with increasing generator-detector separation at the expense of the longitudinal and transverse peaks;
3. the effect of helium should be utterly negligible. The difference between the crystal-vacuum reflection signal and the crystal-helium signal is smaller than the thickness of the line used to draw the pulses in Figure 3.1.

The results of detailed calculations of signal intensity as a function of time of arrival for a given geometry including Fermat's principle, exact reflection coefficients, a Debye phonon density of states and solid angle effects are shown in Figure 3.1. Note that the signals corresponding to three different angles of incidence arrive at the detector.

Our first phonon reflection experiments, which were designed to test these predictions, were performed with time resolution of approximately 300 nsec using sapphire of unknown orientation. Since the importance of high time-of-flight resolution was not yet appreciated, the experimental parameters were similar to those used by previous workers;[15] i.e., heater and bolometers were made of a single strip 1 mm x 5 mm and 100 nsec heater pulses were used. A typical result of the earliest experiments is shown in Figure 3.2. In addition to three peaks expected on the basis of the above analysis there are several smaller peaks which follow the large transverse peak. These can be explained using isotropic elastic theory by taking multiple reflections into account. All the peaks lie on a smooth background signal that begins at t = 0. This background is presumably due to phonons that have not been reflected from the back wall, but rather have been scattered by impurities or defects in the crystal, and thus have a continuous distribution of arrival times; a simple argument shows that the background due to bulk scattering should be proportional to t^{-2} if the generator and detector are small and close together. Side wall scattering also contributes to the background signal which is not affected by helium on the reflection surface.

The peaks in Figure 3.2 are not well resolved, and it is difficult to appraise the effects of helium on a single peak since the shape of the signal seems to change when helium is added. In order to study each peak separately, crystals which were considerably larger than any previously used for ballistic phonon propagation experiments were purchased. Large crystals provide long flight times, so the interval between arrivals is also longer and the individual peaks can be more easily resolved.

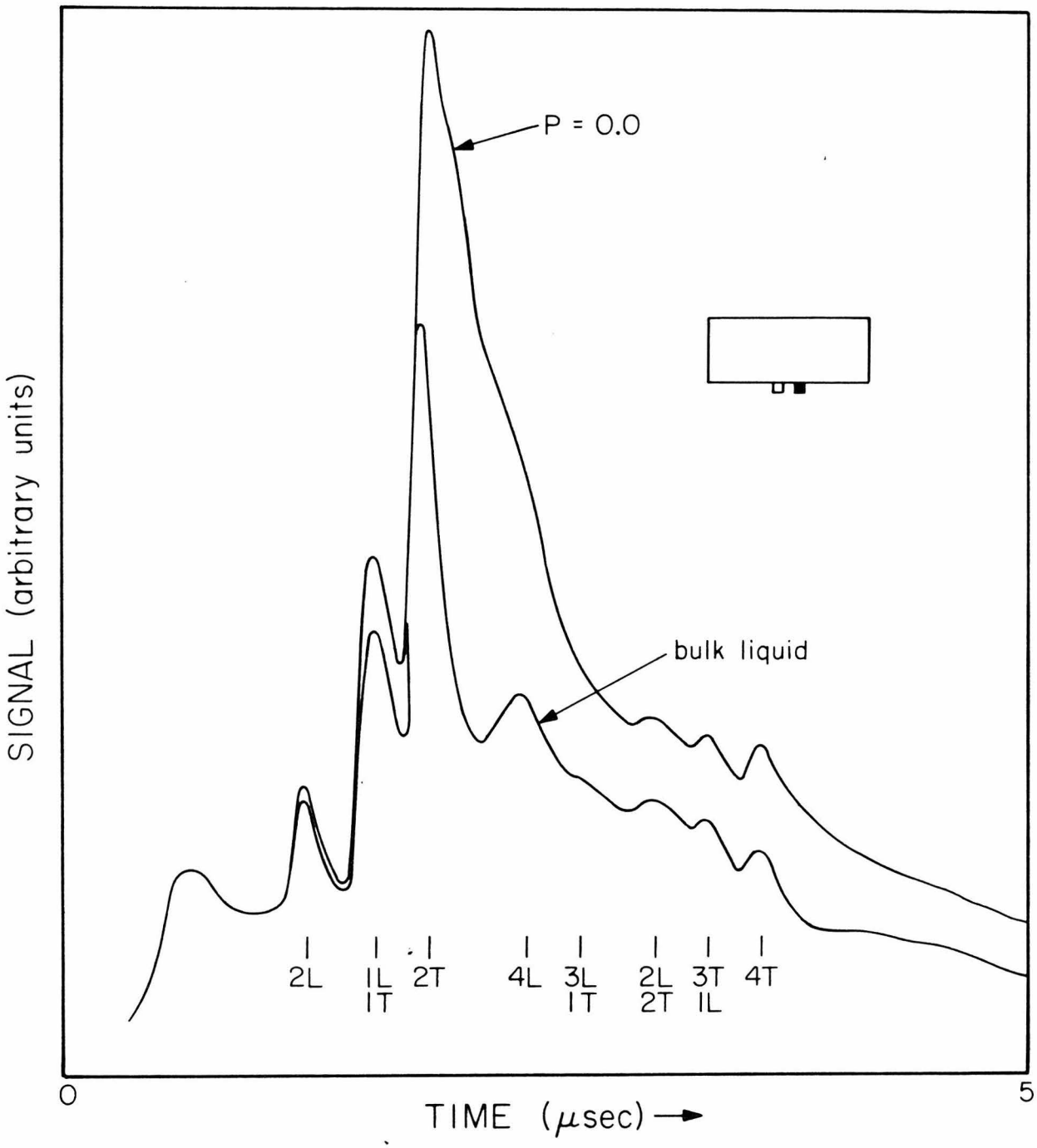

Figure 3.2. Low resolution phonon reflection signal. The shape of the crystal, which is 6 mm x 15 mm dia, is shown in the inset. The computed arrival time of various phonon processes for both two and four traversals of the crystal are also indicated.

Data from a crystal 42 mm x 22 mm diameter are shown in Figure 3.3. This long crystal has the additional advantage that for a heater-bolometer pair fabricated as close together as possible, the incidence angle for specularly reflected phonons is less than 1°; the finite separation of the heater and bolometer limit the smallest incidence angle that can be achieved using 1 cm thick crystals to about 5°. Note that there is no observable mode conversion signal, consistent with the small incidence angle. The arrival times of the two almost degenerate transverse modes can also be resolved, as can the signals due to multiple reflections of the transverse waves. The transverse phonons which have been reflected three times at the far wall have propagated through more than 25 cm of sapphire which probably represents a world's distance record for thermal phonons.

The effect of helium on the reflection spectrum in these experiments was surprisingly small. The reflection coefficient of the transverse phonons as measured by the ratio of the height of the bulk liquid reflection peak to the vacuum interface peak is R = 0.96, which is much larger than the reflection coefficient obtained in our previous experiments on shorter crystals, and much larger than any reflection coefficients reported in the literature (see, however, reference 27). This result remained paradoxical until the effects of nonspecular scattering were more clearly understood (see Chapter Four).

Since the anomalous coupling to helium seemed to depend strongly on angle, it was important to investigate phonon reflection at large incidence angles. An unoriented sapphire crystal 6 mm x 57 mm diameter

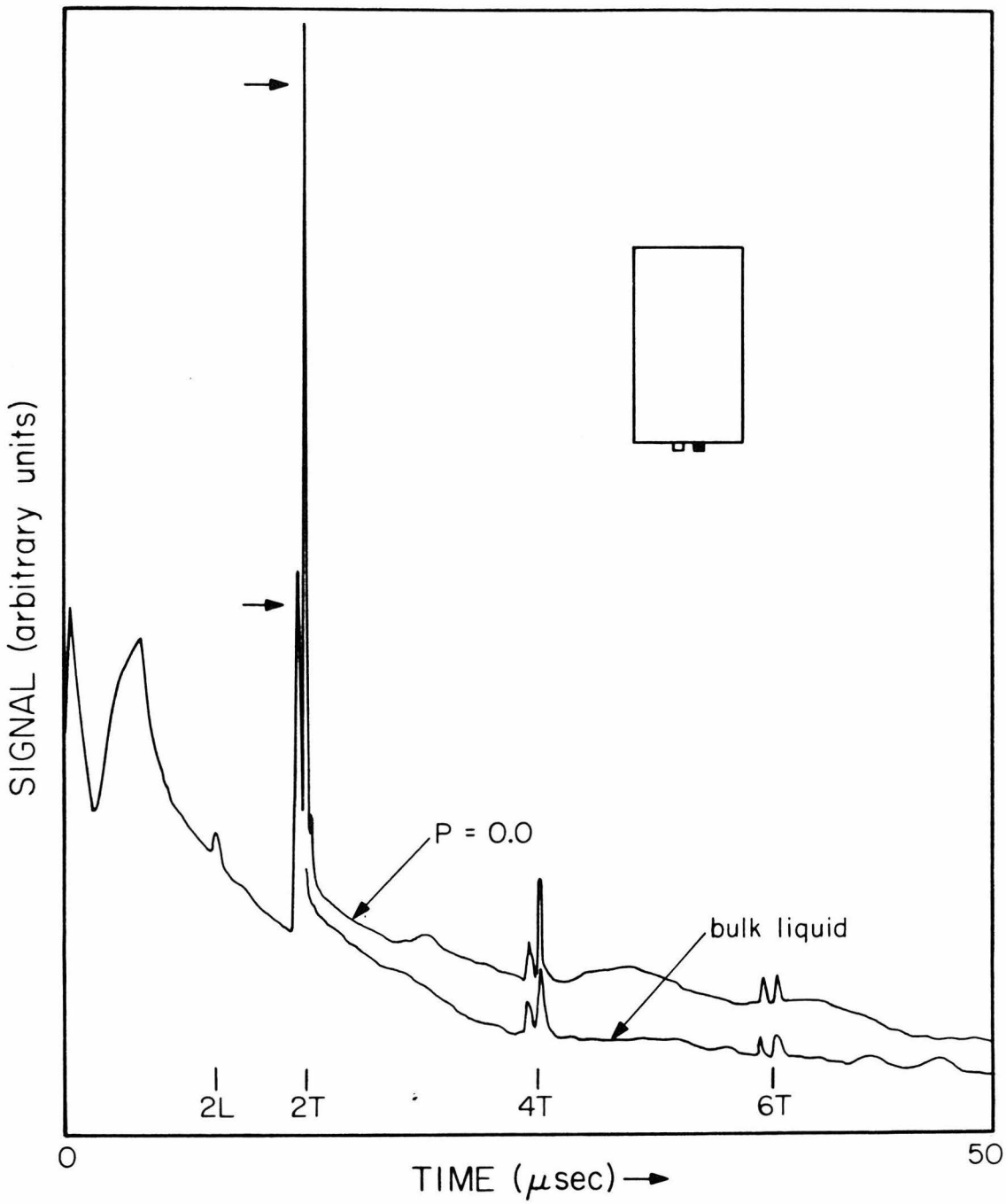

Figure 3.3. Phonon reflection signal in a 42 mm x 22 mm dia unoriented sapphire crystal. The horizontal arrows indicate the transverse peak heights for reflection from a helium interface. Note that the effect of helium is much smaller than in Figure 3.2. Peaks are labeled by the number of traversals of the crystal and the polarization. Although multiple reflections of the transverse peaks can be seen, there is no mode conversion peak.

was used for this purpose. Since calculations and previous experience showed that the phonon pulses could not be clearly resolved with a crystal of this thickness, an effort was made to increase the time resolution of the experiment by making smaller heaters and bolometers and by using shorter heating pulses.

The higher resolution reflection data at larger angles did not reveal a gradually increasing mode conversion peak, as expected on the basis of isotropic elastic theory, but rather a complicated signal with as many as seven peaks (see Figure 3.4). The fact that this pattern of peaks changed when the heater and bolometer were remade in a different position on the crystal confirmed the suspicion that the crystal anisotropy was responsible. This was somewhat surprising since the usual measures of crystal anisotropy are small for sapphire, and it was expected that the effects of anisotropy on the reflection signal would also be small. The effect of helium was also rather peculiar, with some peaks affected much more than others while some peaks seemed to appear only with helium on the reflection surface. This experimental result suggested that complicated effects which were crucial to the understanding of phonon reflection were being obscured by the low resolution spectra such as Figure 3.2.

Phonon Reflection in an Anisotropic Solid

In order to understand data like those shown in Figure 3.4, it was necessary to analyze the reflection of elastic waves in an anisotropic medium. The starting point for this analysis is Newton's Law in the form

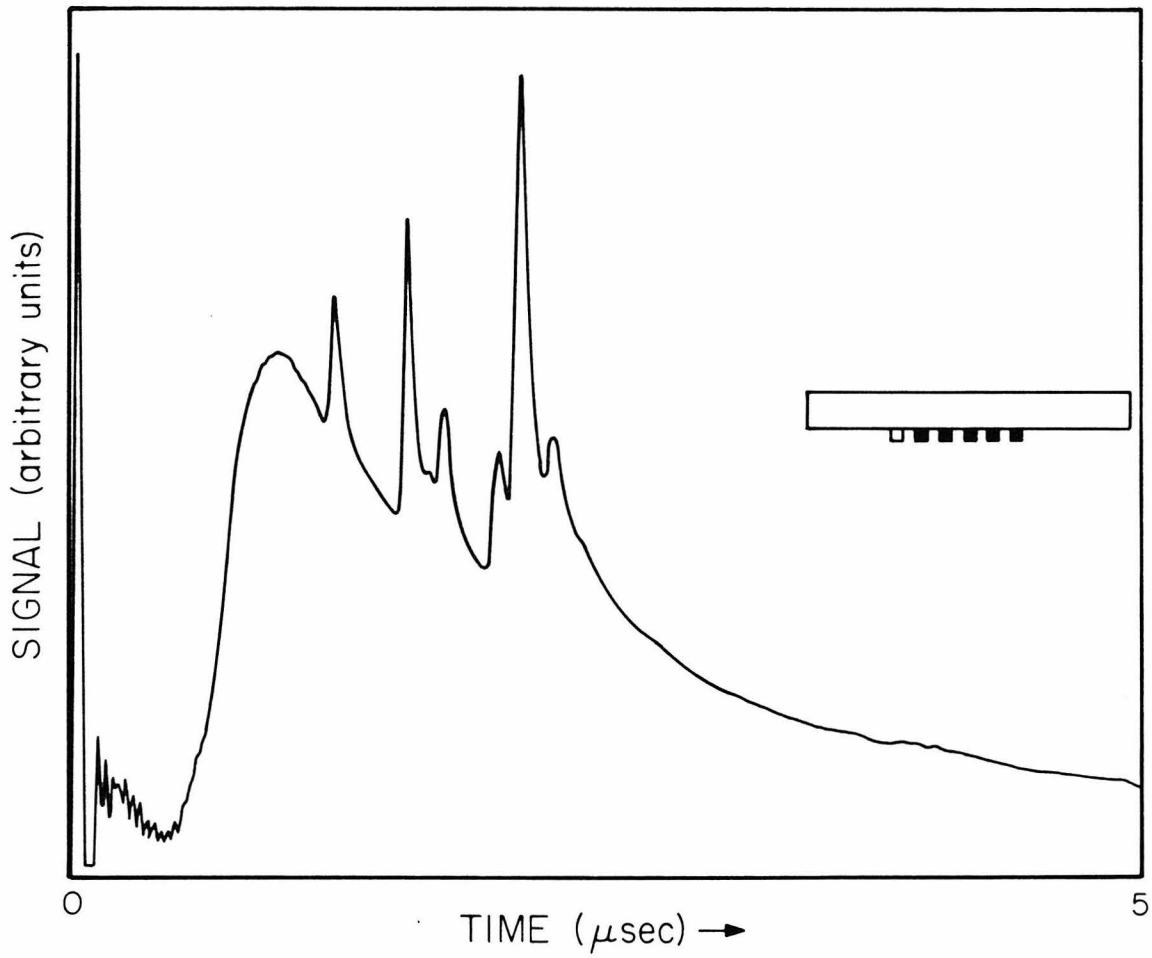

Figure 3.4. Phonon reflection signal for an unoriented sapphire crystal 6 mm x 57 mm dia.. The signal is due to firing the middle of the five heaters shown in the inset. The heater-bolometer separation is 6.7 mm; isotropic elastic theory predicts a signal like that shown in Figure 3.1.

$$\rho \frac{\partial^2 u_i}{\partial t^2} = \frac{\partial \sigma_{ik}}{\partial x_k} \tag{3.1}$$

where ρ is the density, u_i the displacement and components x_k are any convenient basis of three orthogonal vectors.[21,22,34] The repeated index convention is observed throughout. The stress tensor, σ_{ik}, is in general related to the strain tensor, $u_{\ell m}$ by

$$\sigma_{ik} = c_{ik\ell m} u_{\ell m} \tag{3.2}$$

The elastic tensor $c_{ik\ell m}$ has $3^4 = 81$ elements, but crystal symmetries and stability criteria reduce the number of independent ones. For sapphire, there are six independent elastic constants, listed in Table 2.1. In terms of the elastic tensor, Newton's law takes the form

$$\rho \frac{\partial^2 u_i}{\partial t^2} = c_{ij\ell m} \frac{\partial^2 u_m}{\partial x_i \partial x_\ell} \tag{3.3}$$

which is the equation obeyed by elastic waves in an anisotropic medium. In contrast to the isotropic case, the polarization of a wave is not simply parallel or transverse to the k vector; the crystal selects preferred directions of oscillation. Substitution of plane wave displacements

$$u_i = e_i e^{i(k\cdot x - \omega t)}$$

into equation (3.3) where $\hat{e}$ is a unit polarization vector, k and ω the wave-vector and frequency, yields an eigenvalue condition on the polarization:

$$(\lambda_{ij\ell m}\, n_i\, n_j - v^2\, \delta_{\ell m})\, e_m = 0 \qquad (3.4)$$

Here $\lambda_{ij\ell m} = (1/\rho)\, c_{ij\ell m}$ and $\vec{k} = (\omega/v)\, \hat{n}$ where $\hat{n}$ is a unit vector. The solutions of equation (3.4) determine the three allowed orthogonal polarization vectors and associated phase velocities v for any given direction $\hat{n}$. The polarizations have no particular orientation with respect to $\hat{n}$ or the surface of the crystal, so they can only be described as quasi-longitudinal or quasi-transverse.

Another important effect of anisotropy is that the energy of a wave does not move in the same direction as the $\vec{k}$ vector, but rather is transmitted in a direction given by the power flow vector $\vec{p}$,

$$p_i = -\sigma_{ik} \frac{\partial u_k}{\partial t} \qquad (3.5)$$

The time average power flow may be written in terms of the elastic tensor as

$$\overline{p_i} = \frac{1}{2}\omega\, c_{ij\ell m}\, k_\ell\, e_j\, e_m \qquad (3.6)$$

This vector is similar to the Poynting vector of electromagnetic theory, and is sometimes called the elastic Poynting vector. Thus, an elastic wave in an anisotropic medium is described by three vectors, $\vec{k}$, $\hat{e}$ and $\vec{p}$ whose mutual orientation is a complicated function of direction.

As in an isotropic solid, translation invariance along the surface requires that on reflection the component of $\vec{k}$ parallel to the surface must be conserved. However, this law cannot be expressed in simple

form because the magnitude of $\vec{k}$ for each polarization depends on direction in the crystal. The values of the reflected wavevectors for any given incident geometry must generally be found by solving a sixth order polynomial equation, the solutions of which may be represented graphically as shown in Figure 3.5. Here, in a polar plot, curves of constant ω for each mode in the plane of incidence are drawn. The intersections of those curves with the line given by $k_{||}^{ref} = k_{||}^{in}$ (the symbols represent the parallel components of the reflected and incident wavevectors, respectively) give the permitted solutions for outgoing waves. The line may intersect all three polarizations, giving rise to three outgoing waves, or there may be evanescent solutions as occur in the isotropic case when the critical angle is exceeded.

The curves shown in Figure 3.5 represent a planar cross section of the constant ω surface, which is also known as the slowness surface, since the points on the surface given by $k = (\omega/v)\hat{n}$ are inversely proportional to the phase velocity v. For every direction $\hat{n}$, there are three possible phase velocities, so the slowness surface is composed of three sheets in k space which may intersect. The surface is described algebraically by the condition

$$\det (\lambda_{ij\ell m} k_i k_j - \delta_{\ell m}) = 0 \qquad (3.7)$$

which yields a very complicated polynomial in the components of $\vec{k}$. The equations for the curves in Figure 3.5 are obtained by restricting the k_i in equation (3.7) to lie in the plane of incidence determined by $k_{||}^{in}$ and the surface normal m_k. It is easier to evaluate the coefficients of the

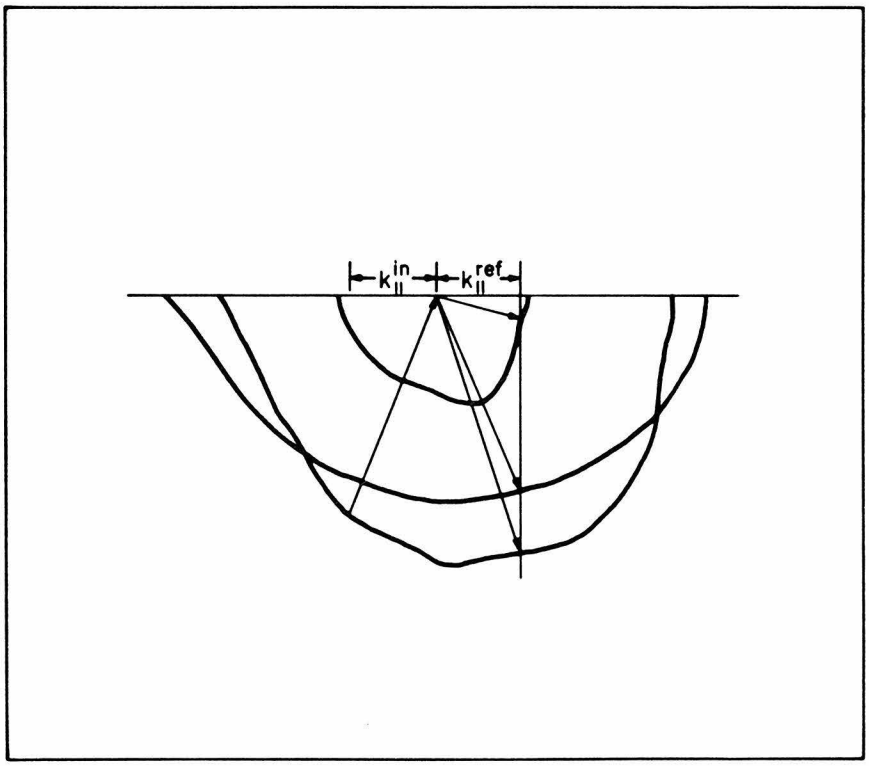

Figure 3.5. Schematic polar plot of curves of constant ω in k space for the crystallographic plane defined by $\underset{\sim}{k}^{in}$ and the surface normal $\hat{m}$. The inner curve represents the quasi-longitudinal mode, which always has the larger phase velocity. The larger curves correspond to the two quasi-transverse modes. If the solid were isotropic, these curves would be circles. The k vectors of the three reflected waves, which are related to the incident wave by the relation $k_{\|}^{in} = k_{\|}^{ref}$, are determined by the geometrical construction illustrated in the Figure.

resulting polynomial in a rotated frame in which $k_y^{in} = 0$. In this frame $\underset{\sim}{k}^{in} = (k_{||}^{in}, 0, k_{\perp}^{in})$ and $\underset{\sim}{k}^{ref} = (k_{||}^{in}, 0, k_{\perp}^{ref})$. Since $k_{||}^{in}$ and $k_{\perp}^{in}$ are known, equation (3.7) reduces to a sixth order polynomial equation in the single variable $k_{\perp}^{ref}$. Three of the solutions (those with $Re(k_{\perp}^{ref}) > 0$) correspond to refracted modes which are not allowed at a vacuum interface. Solutions with $Re(k_{\perp}^{ref}) < 0$ correspond to possible reflection processes, although if $k_{\perp}^{ref}$ has a complex part the reflected wave will be exponentially damped.

Once the permitted solutions have been determined, the amplitude of each is obtained using (as in the isotropic case) the stress-free boundary condition at the surface

$$\sigma_{ik} m_k = 0 \tag{3.8}$$

If we imagine an orthogonal coordinate frame defined by the polarization vectors for each $\vec{k}$, then the coupling upon reflection between the various modes is proportional to the projection of a given incident polarization on each of the three reflected polarizations. In other words, the coupling is governed by how much the coordinate frame twists when the waves change direction due to reflection. The important point here is that the twisting of the polarization frame is not simply related to the anisotropy of the phase velocity. That is why, even in the nearly isotropic case of sapphire, mode mixing in an arbitrary orientation may be strong, giving rise to complicated results like those shown in Figure 3.4.

Computation of the trajectories that transport energy from the heater to the detector is also more difficult than in the isotropic case because energy flows along the p vector, but reflection is governed by the k vector which is not collinear with it. Moreover, the vector $\underset{\sim}{k}^{in}$ of an emitted beam that will result in a signal at the detector need not be in the plane containing the heater, detector and surface normal. It is not uncommon to find the necessary $\underset{\sim}{k}^{in}$ more than 30° out of that plane. Thus the process of finding the right path for a given combination of modes is similar to artillery ranging. A beam is sent in some direction from the heater, and the point where energy in the desired reflected mode arrives back at the same surface is computed. The aiming direction is then adjusted and the computation repeated until a hit is scored on the bolometer. To further complicate matters, the time-of-flight of (say) the SV → L path is no longer equal to that of the L → SV path because, unlike the isotropic case, each of the velocities now depends on direction. Instead of the three processes shown in the inset of Figure 3.1, an anisotropic solid has nine distinct channels connecting heater and bolometer, and the above artillery practice must be repeated nine separate times for each configuration of heater and bolometer to predict a complete spectrum.

If the incident (i.e., emitted) and reflected p vectors are, respectively, $\underset{\sim}{p}^{in}$ and $\underset{\sim}{p}^{ref}$, the mathematical criterion for scoring a hit on the bolometer is

$$H \frac{\underset{\sim}{p}_{in}}{(\underset{\sim}{p}_{in} \cdot m)} + \frac{\underset{\sim}{p}_{ref}}{(\underset{\sim}{p}_{ref} \cdot m)} = \vec{x} \qquad (3.9)$$

where H is the thickness of the crystal and $\vec{x}$ the vector separation of heater and bolometer. A computer is programmed to guess $\underset{\sim}{k}^{in}$, calculate $\underset{\sim}{k}^{ref}$ by imposing the condition $k_{||}^{in} = k_{||}^{ref}$ and solve equation (3.7) numerically for the intersections shown in Figure 3.5. The initial guess for k_{in} is obtained by first solving the problem by assuming that the crystal is isotropic. Equations (3.4) and (3.6) are then used to find the associated p vectors for each combination of polarizations. If $\underset{\sim}{p}^{in}$ and $\underset{\sim}{p}^{ref}$ do not satisfy equation (3.9) to within a tolerance set by the size of the generator and detector, $\underset{\sim}{k}^{in}$ is corrected and the calculation repeated until the error is satisfactorily small. Moreover, the calculation must be repeated until all nine channels have been found.

In order to describe systematically all the specular reflection channels, a convenient labeling scheme is required. In an isotropic solid, every phonon reflection process can be labeled by its polarization as, for example an SV → L process, but this obviously does not work for anisotropic media. In most crystals the quasi-longitudinal mode has the largest phase velocity in all directions, so it can usually be distinguished from the two quasi-transverse modes. Using the same idea, previous authors[15,16,35] have divided the transverse modes into fast transverse (FT) and slow transverse (ST) according to the magnitude of the phase velocity. This scheme is not suitable for classifying reflection processes because the polarization and energy flow vector are not continuous functions of $\vec{k}$ as $\vec{k}$ varies over the ST or FT phase velocity surfaces.

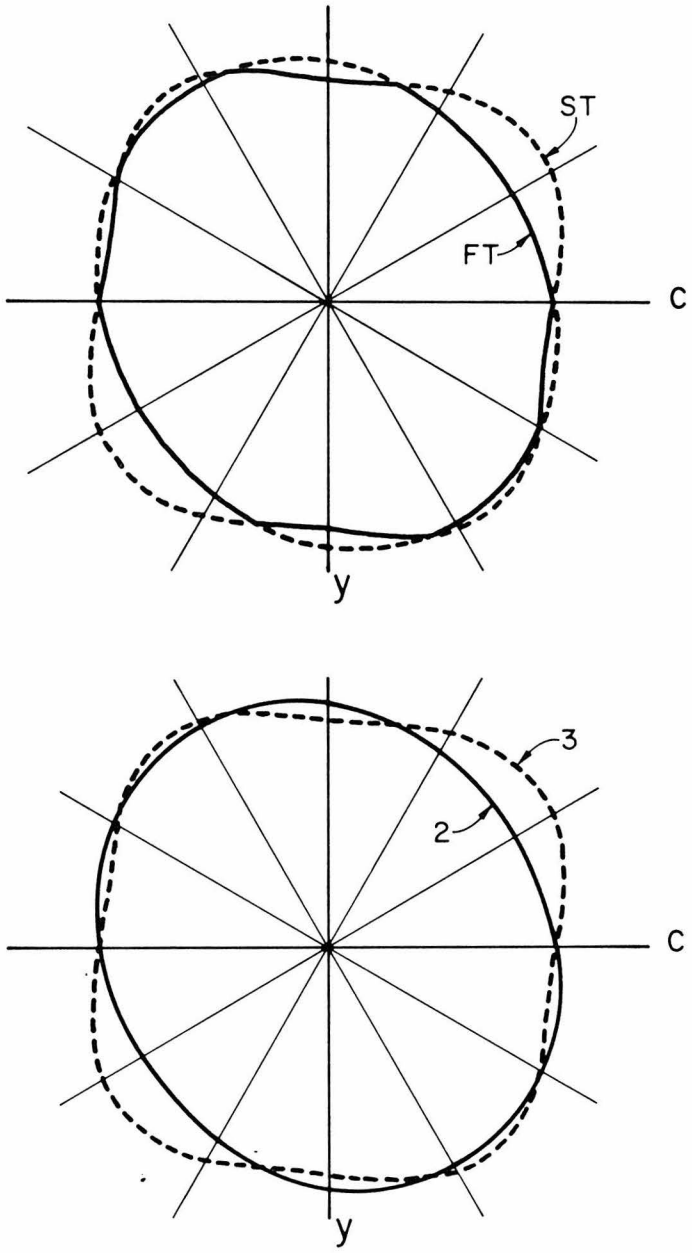

Figure 3.6. Polar plot of the phase velocity of the two transverse modes in the CY plane of sapphire. The upper plot shows the fast and slow transverse branches; note the sharp corners in both curves. The lower plot illustrates the number labeling scheme discussed in the text.

The discontinuities arise at points where the two sheets of the phase velocity surface intersect, as shown in Figure 3.6. Because of these discontinuities there may be several possible reflection channels which would be labeled FT → FT while no FT → ST channel may exist. The lack of a one-to-one correspondence between reflection channels and phase velocity labels, and the possible discontinuities of the polarization and power flow vectors are very inconvenient for computer searches, so a different labeling scheme was developed.

The phonons with k vectors in the surface normal direction are labeled 1, 2 or 3 according to the magnitude of the phase velocity with 1 = longitudinal. A phonon with k vector in any other direction $\hat{n}$ can be associated with one in the surface normal direction $\hat{m}$ by finding a smooth curve on the phase velocity surface which connects the two directions and on which the polarization is continuous. In practice, this means that at intersections of the phase velocity surface the transverse sheets are patched together to make a smooth surface without corners. The two methods of labeling transverse phonons are illustrated in Figure 3.6. Although the number labeling method yields continuous dependence of p_i and e_i on $\vec{k}$, it is not a local characterization of the polarization and is much more difficult to apply than simply distinguishing between fast and slow transverse modes.

Experimental Results

To test the calculations outlined in the previous section, we have performed experiments using a crystal whose orientation was chosen

to simplify the spectrum and facilitate the computations in at least one plane of incidence. The crystal is a cylinder, 9.53 mm thick whose two faces (which are optically polished) lie in the C-X plane of the sapphire lattice (the X, Y and C axes in the sapphire lattice are shown in Figure 2.3). The ambiguity in the exact crystal orientation which is discussed in Chapter Two means that one face of the disk is a $(01\bar{1}0)$ plane while the other is a $(0\bar{1}10)$ plane, but we do not know which is which. The difference is not crucial to the experimental results, and for purposes of calculation we have assumed that the reflection surface is a $(01\bar{1}0)$ plane corresponding to the Y-axis in Figure 2.3. The diameter of the cylinder, 57.2 mm, is large enough to assure that sidewall reflections do not interfere with the spectrum.

The C-Y plane is a particularly simple one for phonon propagation in sapphire because one of the transverse modes has polarization perpendicular to the plane and the other two polarizations are contained in it. Moreover, for waves propagating in the C-Y plane, the k vectors and p vectors, while still not collinear, are at least all in the plane, greatly reducing the number of iterations needed for the calculations. The coplanar feature is especially economical since each change in the $\underset{\sim}{k}^{in}$ surface normal plane requires rewriting the elastic tensor in a new basis, a procedure which requires over 10^4 computer operations. As in an isotropic solid, the mode with polarization perpendicular to the C-Y plane is decoupled from the other two, so there are only five reflection channels (rather than nine) in this plane. Because of the high symmetry of this plane and the simple orientation of the polarization vectors, each mode can be uniquely labeled by its polarization as L, SV or SH.

Experiments were thus conducted in which the heater, bolometer and surface normal lay in the C-Y plane. For contrast, we also present results with the heater-bolometer-surface normal in the X-Y plane which is a more typical low symmetry plane, where none of the above simplifications are valid. In the first case, one bolometer and five heaters are laid out at intervals along the C axis. In the second case a bolometer and five heaters are laid out along the X axis. The heaters are numbered, with heater no. 1 closest to the bolometer. In addition to testing our calculations, the data presented here constitute, to our knowledge, the first systematic study of phonon reflection as a function of angle of incidence (see, however, reference 32).

A typical example of a spectrum on the C-Y plane is shown in Figure 3.7. Here the heater (heater no. 3) and bolometer are separated by 6.7 mm along the C axis. One sees five peaks, just as expected. The reflection signal of Figure 3.8 was taken in the same crystal with heater and bolometer separated by 9.0 mm along the X axis. Both figures also show the predicted arrival time of the various specular reflection processes.

Because the purpose of these experiments was to measure times-of-flight for as many channels as possible in each orientation, all experimental parameters were chosen so as to optimize the resolution of peaks such as those seen in Figure 3.7 and 3.8. The width of a peak is a time which is a consequence of some six separate phenomena, each of which may in turn be characterized by a time; the width of the initial heater pulse, the thermal relaxation times of the heater and the bolometer,

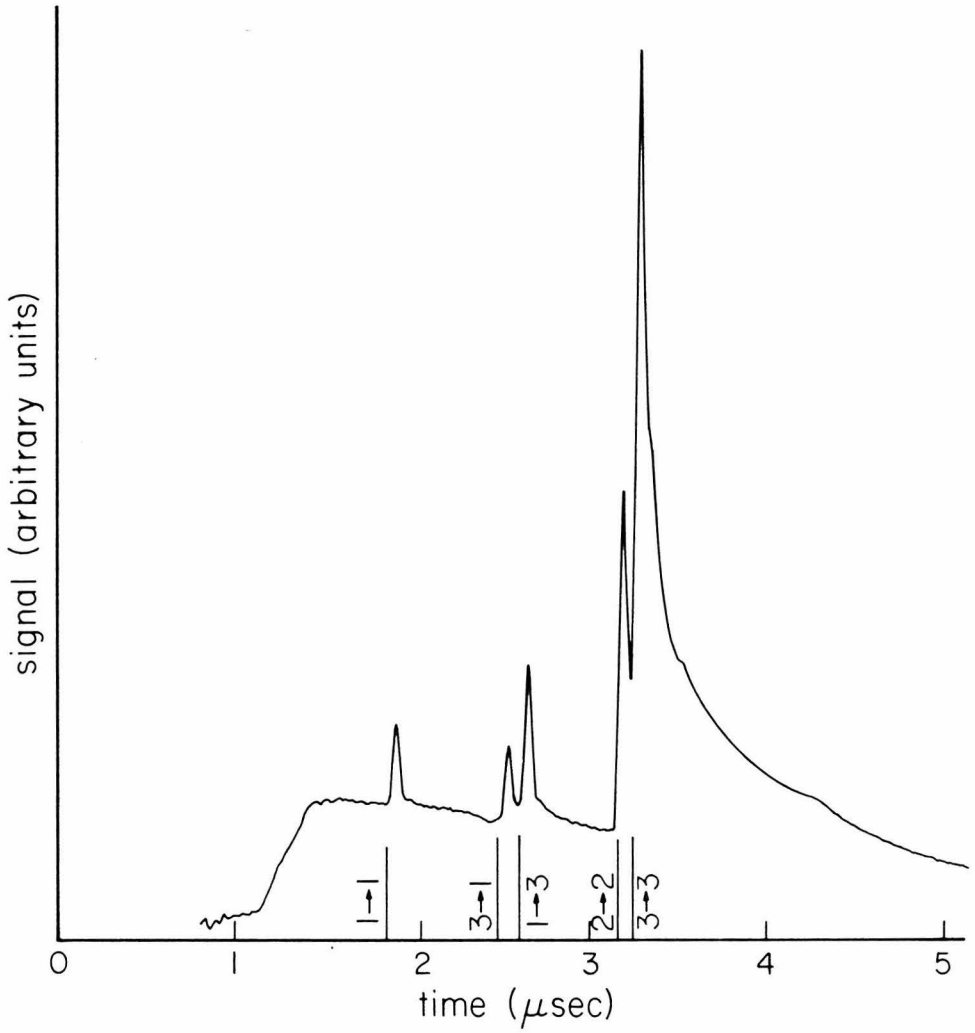

Figure 3.7. Reflection signal for heater no. 3 in the C-Y plane. The predicted arrival times for processes with non-zero coupling are marked by the vertical lines.

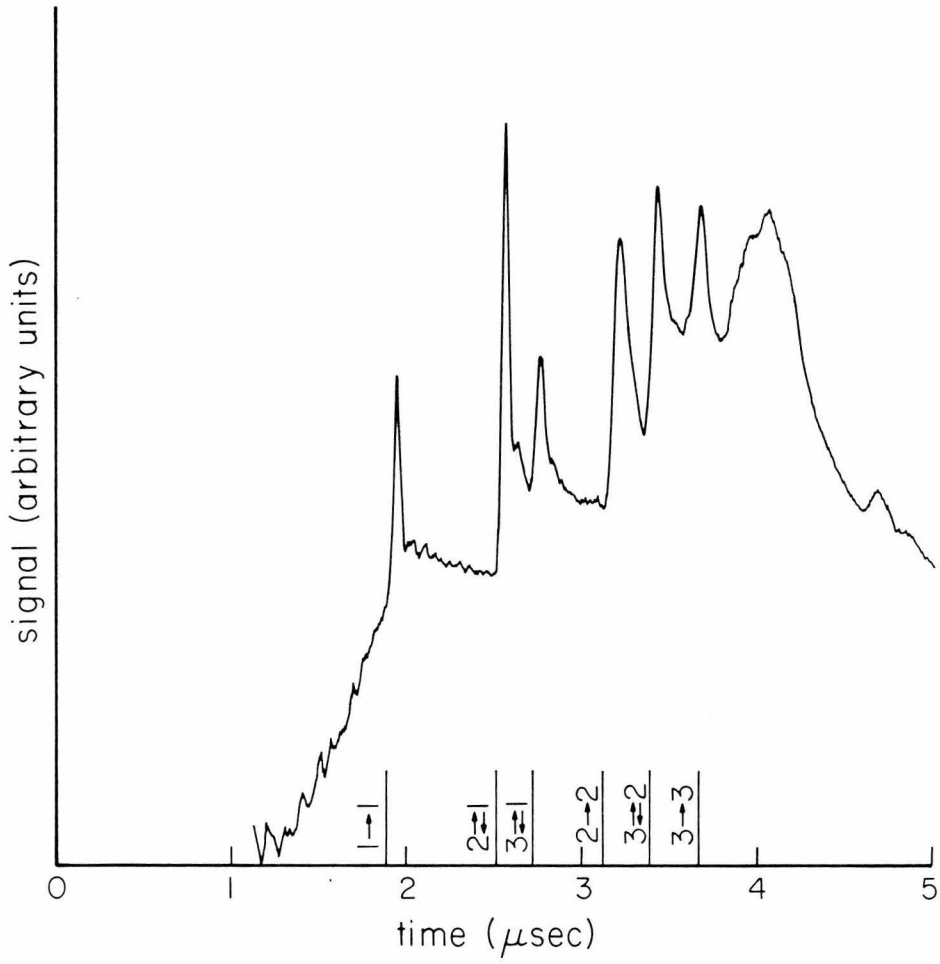

Figure 3.8. Reflection signal for heater no. 4 in X-Y plane. The predicted arrival times for processes with non-zero coupling are marked by the vertical lines.

effective times due to solid angle effects at heater and bolometer, and the aperture of the boxcar integrator used to read out the data.

Heater pulses of 35 nsec width were used. Heater and bolometer relaxation times are not well known, but were minimized by being at an interface between sapphire and superfluid helium. They are believed to be less than 20 nsec. Broadening due to the solid angle subtended by heater and bolometer may be estimated by $(w/v)\sin\theta$ where w is a dimension of the device, v is a speed of sound, and θ is the angle of incidence or reflection. The heaters were of serpentine form localized to 0.4 mm square, the bolometer slightly larger. Since for sapphire $v \simeq 10^7$ mm/sec, we estimate a characteristic time of up to 50 nsec for these geometric effects. Finally, the boxcar aperature was set at 25 nsec. Thus, all of these times were of the same order of magnitude, around 50 nsec. All of these times interact in a complicated way, but the resulting peaks may be observed to have widths of roughly 50 nsec. It is probably possible to resolve peaks if they are more than 25 nsec apart. The absolute time-of-flight of each mode, measured from the beginning of the heater pulse (detected on the bolometer signal by electronic cross-talk) and the beginning of the rise of the peak is probably determined to better than 50 nsec, but there is a geometric uncertainty of that order inherent in the finite size of the heater and detector.

The results of calculation and experiment for heater-bolometer-surface normal in the C-Y plane are summarized in Table 3.1. The spectra themselves are shown in Figure 3.9. Data and calculations for the X-Y plane are given in Table 3.2 and Figure 3.10.

Table 3.1. Heater-bolometer-surface normal in C-Y plane.

Channel		$\hat{e}_{in} \cdot \hat{e}_{ref}$	θ_{in} (degrees)	t (Predicted) (μsec)	t (Observed) (μsec)
Heater no. 1: heater-bolometer separation = 1.5 mm; θ_o = 4.57°					
1 → 1	L → L	0.987	7.45	1.714	1.71
3 → 1	SV → L	0.0205	0.57	2.428	2.43
1 → 3	L → SV	0.206	10.3	2.455	
2 → 2	SH → SH	1.0	4.57	2.956	2.93
3 → 3	SV → SV	0.998	2.29	3.156	3.10
Heater no. 2: heater-bolometer separation = 4.3 mm; θ_o = 12.8°					
1 → 1	L → L	0.89	17.18	1.765	1.74
3 → 1	SV → L	0.147	4.18	2.442	2.42
1 → 3	L → SV	0.385	18.5	2.523	2.49
2 → 2	SH → SH	1.0	16.0	3.044	2.98
3 → 3	SV → SV	0.987	6.3	3.191	3.14
Heater no. 3: heater-bolometer separation = 6.7 mm; θ_o = 19.5°					
1 → 1	L → L	0.748	24.6	1.851	1.84
3 → 1	SV → L	0.302	8.59	2.484	2.48
1 → 3	L → SV	0.516	23.5	2.602	2.58
2 → 2	SH → SH	1.0	24.1	3.165	3.11
3 → 3	SV → SV	0.97	9.62	3.241	3.20
Heater no. 4: heater-bolometer separation = 9.3 mm; θ_o = 25.9°					
1 → 1	L → L	0.57	30.4	1.967	1.94
3 → 1	SV → L	0.479	13.6	2.566	2.53
1 → 3	L → SV	0.65	29.6	2.718	2.68
2 → 2	SH → SH	1.0	31.0	3.318	3.26
3 → 3	SV → SV	0.942	13.4	3.320	

Table 3.1. continued

Channel		$\hat{e}_{in} \cdot \hat{e}_{ref}$	θ_{in} (degrees)	t (Predicted) (μsec)	t (Observed) (μsec)
Heater no. 5: heater-bolometer separation = 12.6 mm; θ_o = 33.4°					
1 → 1	L → L	0.36	35.6	2.134	2.12
3 → 1	SV → L	0.702	20.0	2.710	2.69
1 → 3	L → SV	0.788	35.5	2.896	2.87
3 → 3	SV → SV	0.87	19.2	3.471	3.45
2 → 2	SH → SH	1.0	40.4	3.612	3.55

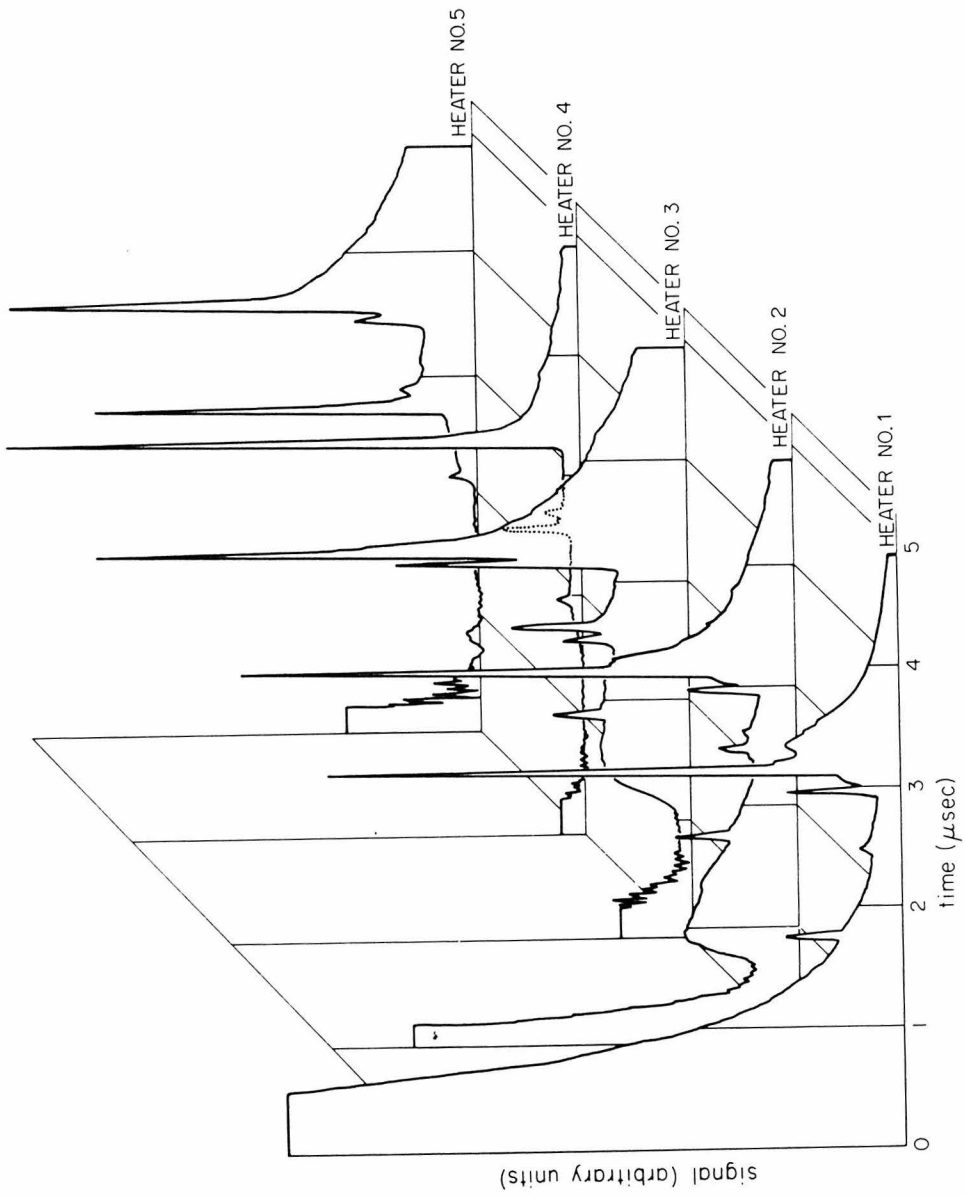

Figure 3.9. Summary of reflection data in C-Y plane. Ordinate scales have been chosen so that the tallest peak in each spectrum is approximately the same height. See Table 3.1 for comparison to numerical predictions.

Table 3.2. Heater-bolometer-surface normal in X-Y plane.

Channel	$\hat{e}_{in} \cdot \hat{e}_{ref}$	θ_{in} (degrees)	ϕ_{in} (degrees)	t (Predicted) (μsec)	t (Observed) (μsec)
Heater no. 1: heater-bolometer separation 1.5 mm; $\theta_o = 4.50°$					
1 → 1	0.987	4.50	0.0	1.710	1.72
1 → 2	.069	10.6	71.6	2.347	
2 → 1	.069	6.59	-72.2	2.350	
1 → 3	0.177	10.89	31.5	2.448	2.45
3 → 1	0.178	6.02	-29.22	2.448	
2 → 2	0.975	1.89	0.0	2.952	2.92
2 → 3	0.475	4.87	0.0	3.060	3.02
3 → 2	0.475	4.58	0.0	3.060	
3 → 3	0.606	12.9	0.0	3.204	3.17
Heater no. 2: heater-bolometer separation 4.2 mm; $\theta_o = 12.4°$					
1 → 1	0.910	12.4	0.0	1.744	1.75
1 → 2	0.212	14.0	42.4	2.378	2.37
2 → 1	0.209	8.25	-43.5	2.379	
1 → 3	0.318	21.2	12.0	2.513	2.49
3 → 1	0.329	11.2	-13.2	2.516	
2 → 2	0.819	5.73	0.0	2.978	2.95
2 → 3	0.766	13.2	0.0	3.121	3.08
3 → 2	0.769	12.0	0.0	3.124	
3 → 3	0.525	18.9	0.0	3.331	3.26
Heater no. 3: heater bolometer separation 6.6 mm; $\theta_o = 19.3°$					
1 → 1	0.788	19.3	0.0	1.803	1.80
1 → 2	0.359	18.9	22.9	2.425	2.38
2 → 1	0.361	11.2	-23.6	2.429	
3 → 1	0.406	14.8	-5.15	2.602	2.58
1 → 3	0.417	29.2	6.30	2.606	
2 → 2	0.563	11.5	0.0	3.034	3.02
2 → 3	0.787	21.2	0.0	3.227	3.20
3 → 2	0.786	18.0	0.0	3.229	
3 → 3	0.510	23.5	0.0	3.489	3.45

Table 3.2. continued

Channel	$\hat{e}_{in} \cdot \hat{e}_{ref}$	θ_{in} (degrees)	ϕ_{in} (degrees)	t (Predicted) (μsec)	t (Observed) (μsec)
Heater no. 4: heater bolometer separation 9.0 mm; θ_o = 25.3°					
1 → 1	0.636	25.3	0.0	1.886	1.903
2 → 1	0.512	15.4	-12.0	2.507	2.51
1 → 2	0.520	26.9	11.5	2.513	
1 → 3	0.482	36.3	2.64	2.721	2.70
3 → 1	0.480	18.0	-2.29	2.721	
2 → 2	0.286	20.0	0.0	3.129	3.14
3 → 2	0.723	24.4	-1.26	3.381	3.35
2 → 3	0.721	29.2	1.14	3.388	
3 → 3	0.510	27.2	0.0	3.665	3.57
Heater no. 5: heater bolometer separation 12.7 mm; θ_o = 33.7°					
1 → 1	0.383	33.7	0.0	2.054	2.05
1 → 2	0.717	39.5	0.0	2.689	2.67
2 → 1	0.718	22.6	0.0	2.691	
1 → 3	0.542	45.8	-0.86	2.939	2.90
3 → 1	0.543	21.9	0.92	2.944	
2 → 2	0.145	37.8	0.0	3.391	3.37
2 → 3	0.595	38.3	1.15	3.684	3.63
3 → 2	0.593	32.1	-1.15	3.688	
3 → 3	0.549	32.1	0.0	3.974	3.91

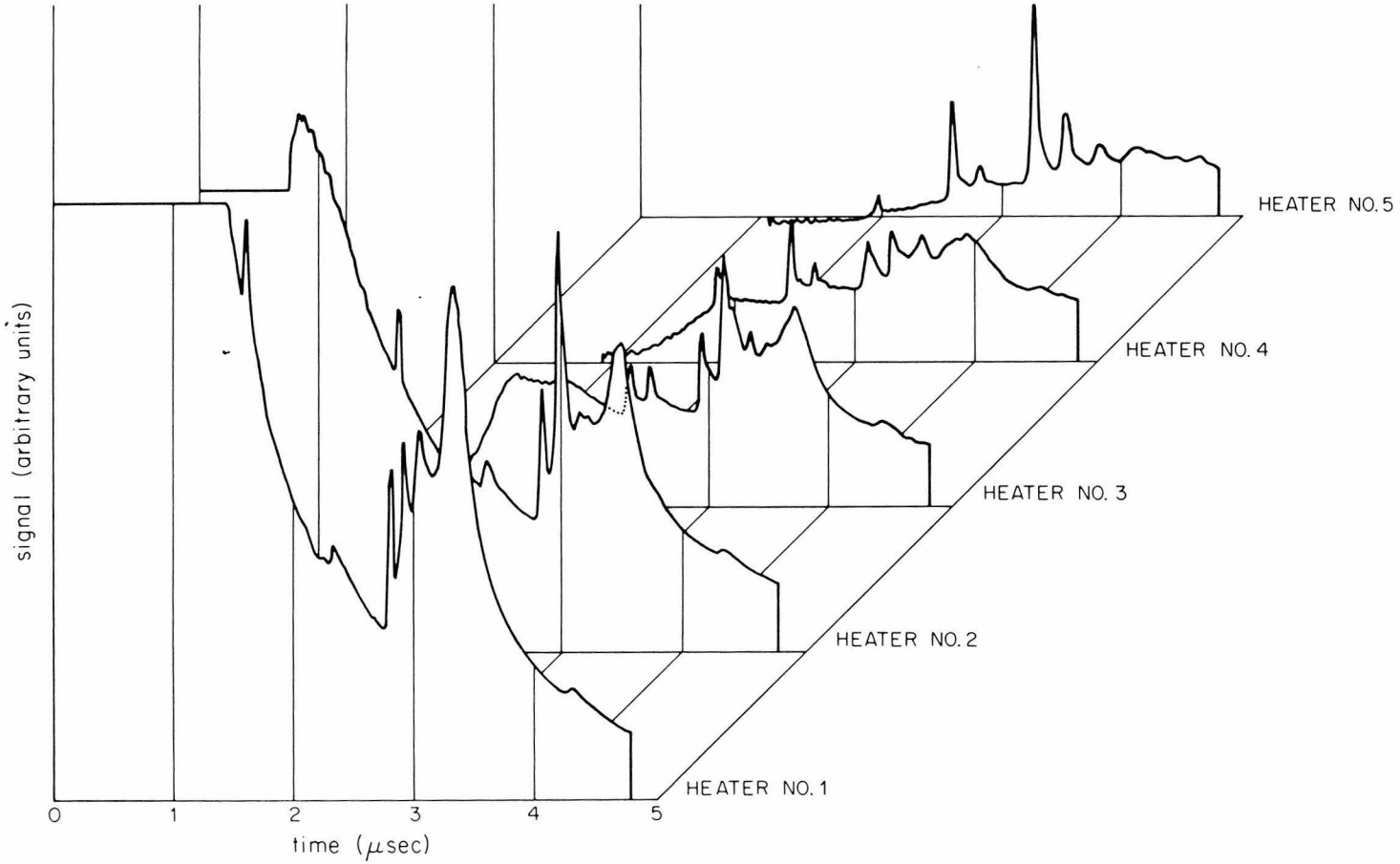

Figure 3.10. Summary of reflection data in X-Y plane. Ordinate scales have been chosen so that the tallest peak in each spectrum is the same height. See Table 3.2 for the comparison to numerical predictions.

Each of these tables has a separate section for each heater, headed by the heater-bolometer separation, and θ_o, the angle of incidence for which an equal angle of reflection would connect heater and bolometer. The first two columns in Table 3.1 give the channel connecting heater and bolometer. The channels for each heater are listed in order of their predicted arrival time. The modes within each channel are identified first by number, 1, 2 and 3, then by name, L, SH and SV, respectively. Identification by name is possible only in the C-Y plane; even here it would be more proper to say quasi-L and quasi-SV. It is also interesting to note that although mode 2 (SH) is the fast transverse mode along the surface normal, the SH-SH channel is the last to arrive when fired from heater no. 5.

The third column of Table 3.1 gives the projection of the incident polarization vector on the reflected polarization vector for each channel. This quantity measures the strength of the coupling on reflection from one mode to the other. The channels not listed (i.e., L → SH) would have zeros in this column, hence are not expected to arrive.

The fourth column of Table 3.1 gives the angle of incidence in the path used by that channel to connect heater and bolometer. For orientation it may be compared to θ_o which would be the angle of incidence of an L → L or T → T channel of the crystal were isotropic.

Finally, columns 5 and 6 show the predicted and observed times-of-flight. The observed times are listed on the same level with the predicted times they are believed to correspond to.

Table 3.2 differs from Table 3.1 in that the modes can be identified by number only. In addition, since the required incident

k vector does not stay in the X-Y plane, an aximuthal angle, ϕ_{in} for the incident (i.e., emitted) ray is also given. The coordinate system identifying θ and ϕ is shown in Figure 3.11. In Table 3.2 there are nine channels with nonzero coupling for each heater, all of them listed.

All told, for the ten heaters in both planes, 54 peaks are predicted to occur with nonzero coupling and at least 25 nsec separation. Every one is observed experimentally with an arrival time agreeing with prediction within the estimated expected error. We thus believe the calculations and procedures we have described have been fully validated.

These results have a number of interesting features which deserve to be pointed out. For four out of the five heaters in the C-Y plane, the SV $\rightarrow$ L and L $\rightarrow$ SV channels are clearly resolved. One result is that in three of the cases, five peaks, which is the maximum number possible, are clearly seen. By contrast, in the X-Y plane, all of the mode conversion peaks arrive within 10 nsec of their inverse channels. For example, in heater no. 2 of the X-Y plane, the 1 $\rightarrow$ 3 and 3 $\rightarrow$ 1 channels are expected at 2.513 and 2.516 μsec, respectively, although they necessarily follow quite different paths through the crystal. The experimental consequence is that one never resolves more than six separate peaks in this plane (as seen, e.g., in Figure 3.8). This behavior is apparently a geometrical accident peculiar to the X-Y plane. Calculations for propagation in arbitrarily chosen crystal orientations indicate seven or eight peaks should often be resolved by 20 nsec or more. On the other hand, the X-Y plane reflection spectra usually have a prominent peak due to mode conversion of transverse phonons, i.e., processes like

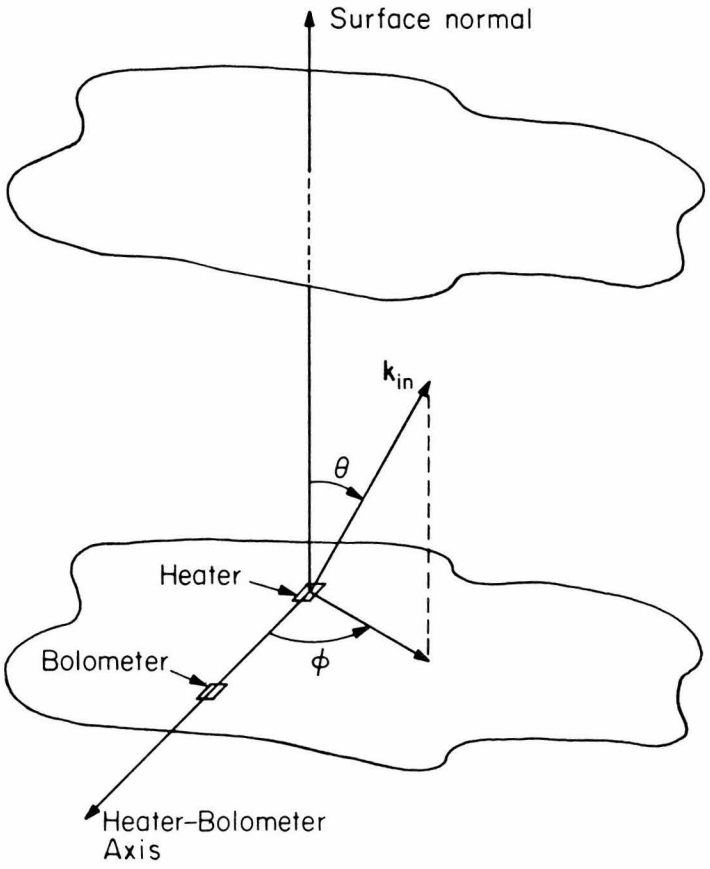

Figure 3.11. Coordinate system used to define θ and φ, as used in Tables 3.1 and 3.2.

$3 \rightarrow 2$. These processes are, of course, completely unexpected on the basis of isotropic elastic theory. They are, nevertheless, quite typical in real crystals. The fact that no $3 \rightarrow 2$ process is observed in the Y-C plane is due to symmetry; in other experiments where the heaters and bolometer were misaligned from the C axis by only 3°, the transverse $\rightarrow$ transverse mode conversion process was easily detected.

The equations of elastic theory also in principle predict the relative heights of the peaks in the various channels. Only limited progress can be made on this point without additional elaborate calculations, but a brief discussion may be useful in order at least to bring out where the complexities lie.

Let us leave aside for the present the difficult question of what distribution of phonons actually emerges from the heater into the crystal. Some progress can still be made by the following argument. The L-L peak height (for example) is proportional to the intensity of the L beam incident at the surface, multiplied by the L-L reflection efficiency at the interface, given by $e_{in} \cdot e_{ref}$. The $L \rightarrow SV$ peak height should be given by the incident L intensity at the surface multiplied by the L-SV conversion efficiency. Thus, calling the peak heights in each channel S_{i-j} and the conversion efficiencies R_{i-j}, one might expect

$$S_{L-SV} = \frac{R_{L-SV}}{R_{L-L}} S_{L-L}$$

The same would be true of course, for any other combination of converted and unconverted channels.

Consider, for example, heater no. 1 of the C-Y plane. The SV → L channel and the L → SV channel are expected to arrive 27 nsec apart, at the edge of resolvability. However, the L → SV coupling is 0.2 while the SV → L coupling is only 0.02. Observed at the expected arrival point is one small peak, which on careful inspection proves noticeably broader than the other specular peaks of the same spectrum. Can we assign it to one channel, or is it an unresolved combination of both?

Application of the above argument indicates it probably belongs to both. The reason is because although $R_{L\text{-}SV} \simeq 10\ R_{SV\text{-}L}$, we observe $S_{SV\text{-}SV} \simeq 10\ S_{L\text{-}L}$ (see Figure 3.9. The L-L and SV-SV peaks are, respectively, the first and last for heater no. 1.) Thus we expect $S_{L\text{-}SV} \simeq S_{SV\text{-}L}$. Quantitatively the argument predicts that each channel will contribute a peak of height about 3/4 the maximum of the observed peak. Thus the argument agrees very well with observation if the peak is an unresolved doublet. If the channels had greater intensity we could probably resolve the two.

Systematically applying the same analysis to all other relevant combinations of peaks, we find reasonable agreement in about half the cases, but serious disagreement in at least some instances. For example, for C-Y heater no. 3 (Figure 3.9), $R_{SV\text{-}L}/R_{SV\text{-}SV} \simeq 0.3$. We thus expect the SV-L peak (the second to arrive) to be about 1/3 the height of the SV-SV peak (the last one). After subtracting background, however, we find it is only about 1/10 the height of that peak, or about 3 times smaller than expected.

Such discrepancies are probably due to the phenomenon of phonon focusing in the incident mode. In the example cited, the SV beam that reflects into the SV-SV channel does not follow the same path as the SV beam that reflects into the SV → L channel. Even if the heater emits an isotropic distribution of SV phonons, the two beams will not generally have the same intensity. Thus the argument we have presented needs to be corrected for the effects of phonon focusing in the incident mode. This phenomenon will be discussed in more detail in Chapter Four. A more accurate analysis would also require exact reflection coefficients computed from equation (3.8).

Implications for the Kapitza Resistance Measurements

In most previous experiments reporting phonon reflection spectra, the focus of attention has generally been on changes in the spectra that occur when helium is brought into contact with the reflecting surface. It is clear that the interpretation of those experiments will remain contradictory and confusing until details such as those described above are fully understood. For example, our analysis and high resolution data show that the single "transverse peak" observed in earlier data is usually the result of four different reflection processes (2 → 2, 2 → 3, 3 → 2, and 3 → 3). The data presented here also show that the signal is composed of two separate parts: sharp specular peaks and broader features which must be due to nonspecular scattering. Phonons which are scattered non-specularly ($k_{||}$ not conserved) arrive at the detector after the specular phonons and sometimes produce a significant "tail" following the sharp

specular peak. This is shown clearly for the last specular peak in the Y-C plane data of Figure 3.7.

In previous low resolution experiments, the signal due to the various specular processes involving transverse phonons as well as the diffuse tail were treated as a single peak. The fact that the transverse peak was strongly affected by helium was generally interpreted as evidence of non-elastic coupling of the transverse modes to the helium.[15,16] The high resolution data suggest a different interpretation.

A comparison of the crystal-vacuum and crystal-helium interface reflection signal for two heaters in the Y-C plane are shown in Figure 3.12. The figure shows that the effect of helium is largest on the diffuse tail. The last sharp peak is also affected, but the earlier arriving sharp peaks are affected very little if at all. It seems that the anomalous coupling to the helium is predominantly due to diffusely scattered phonons. In retrospect, our early low resolution results as well as other published data[15,16,36] confirm this interpretation, since the shape of the "transverse peak" changes substantially when helium is introduced; the trailing edge of the peak (in fact due to diffuse scattering) always is more strongly affected than the leading edge.

In some crystallographic directions, the diffuse signal is not merely an appendage to the specular peak, but the most prominent feature in the reflection spectrum. Figure 3.13 shows the effect of helium on the reflection signal for heater no. 1 in the X-Y plane. The sharp peaks are due to specular processes as listed in Table 3.2, but the large bump which is strongly absorbed by the helium is not attributable to any

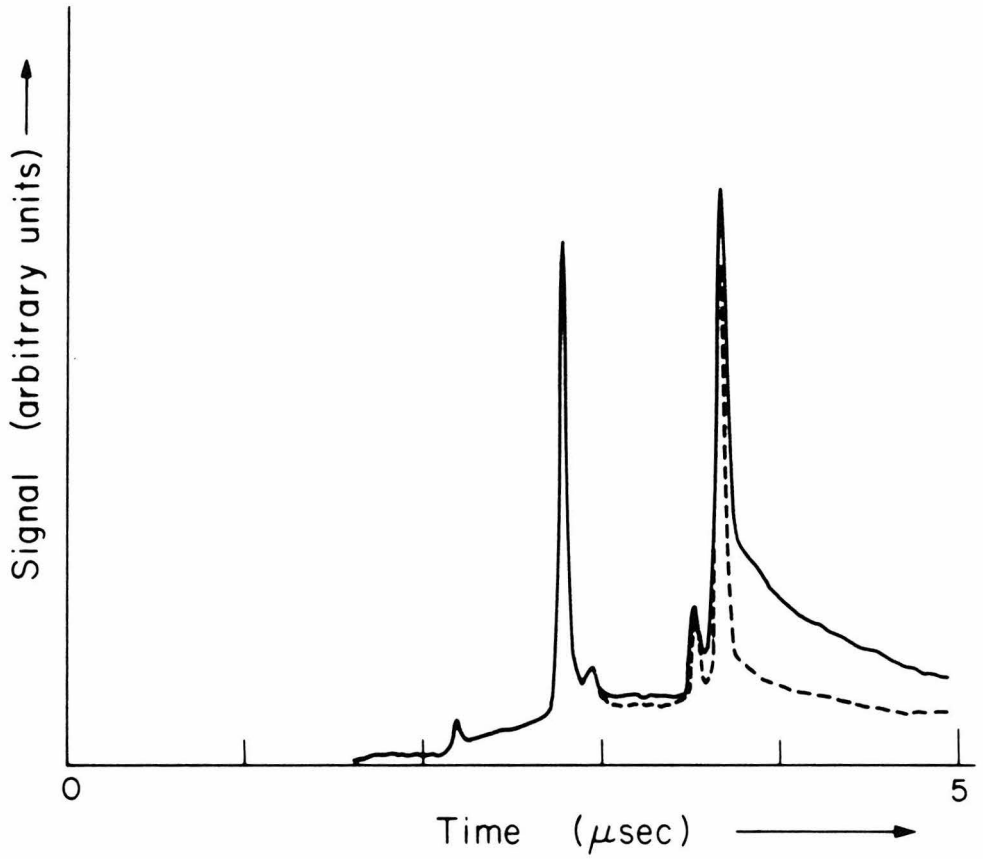

Figure 3.12. Reflection signals for heater no. 5 in C-Y plane. Solid curve is the crystal-vacuum interface spectrum, while the dotted curve is the signal from a crystal-liquid helium interface. Note that most of the effect seems to be in the "tail" which follows the transverse peaks. The mode conversion peak at 2.8 μsec which is well separated from the diffuse scattering signal is not affected at all.

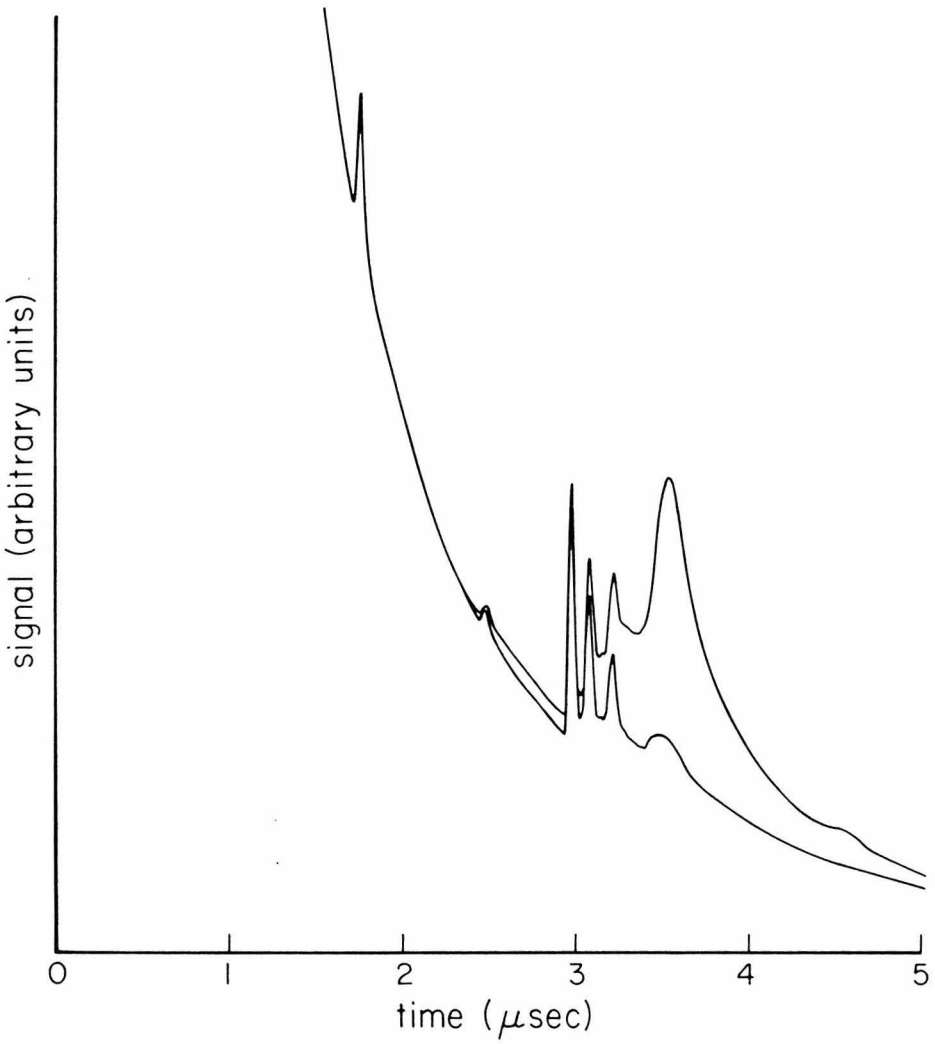

Figure 3.13. Reflection signal for heater no. 1 in X-Y plane. Upper curve is reflection from a vacuum interface, while the lower curve is reflection from a crystal/liquid helium interface. The large diffuse bump, which is not due to any specular reflection process, is almost completely absorbed by the helium.

specular channel. Although the specular peaks are also diminished, it is difficult to quantitatively separate the specular signal from the diffuse signal and the bulk scattering background. Despite this difficulty, the examination of many reflection spectra such as those shown in Figures 3.12 and 3.13 has lead to the following tentative explanation of the experimental results: the diffusely scattered phonons are entirely responsible for the anomalous coupling to helium. Any apparent decrease in the specular peaks is due to a decrease in the underlying diffuse scattering signal. The specularly reflected phonons whose trajectories can be predicted using elastic theory also couple to the helium in accordance with elastic theory; i.e., extremely weakly.

This hypothesis is radically different from the traditional interpretation of phonon reflection spectra. It suggests that the behavior of specularly reflected phonons, which was supposedly being studied in previous experiments, is actually quite simple and can be predicted in detail with tedious but straightforward calculation. The fact that theories which only include specular processes do not explain the experimental results is due to the large effects of diffuse scattering. It is also significant that the diffuse reflection processes are important even at the vacuum interface. This suggests that whatever anomalous coupling mechanism may exist, it is probably intrinsic to the solid and not some peculiar property of quantum systems. If specular processes obey elastic theory, the important scientific questions then become: What causes diffuse scattering? Is there some non-elastic coupling mechanism associated with diffuse scattering? Can the coupling of the

diffuse signal also be explained in terms of classical elastic theory? Before these difficult questions can be answered, it is essential to gain as much information as possible about nonspecular processes from the experimental data. The following chapter addresses this problem.

CHAPTER FOUR: ANALYSIS OF PHONON REFLECTION EXPERIMENTS - NONSPECULAR SCATTERING

As explained in the last chapter, even anisotropic elastic theory does not describe all the features of the vacuum interface reflection spectrum. Moreover, both the "tails" after specular peaks and the large diffuse bumps which appear in the data are strongly affected by introducing helium to the reflection surface; the cause of these effects must therefore be associated with the surface and cannot be explained by bulk scattering processes. In this chapter, we first suggest a possible mechanism for nonspecular scattering and then explore some simple experimental consequences of reflection from a diffusely scattering surface. As in Chapter Three, some of the effects can be described qualitatively using isotropic elastic theory, while others require a more careful analysis which acknowledges elastic anisotropy. The principle goal is to understand the diffuse signal pulse shape and how it depends on crystallographic orientation of heater and bolometer.

Mechanisms of Diffuse Scattering

The condition $k_{||}^{in} = k_{||}^{ref}$, which defines specular scattering and was used in all the calculations in the previous chapter is a consequence of the exact translational invariance of a smooth planar surface. Since a significant fraction of the incident phonons do not obey this condition, it is natural to consider surface roughness which breaks this symmetry as a likely cause of nonspecular scattering.

A useful model of a nonplanar interface which provides a source of nonspecular scattering is the sinusoidally corrugated surface. A sinusoidal surface with wavevector $\vec{q}$, shown in Figure 4.1, can be thought of as the Fourier component of a more realistic statistically rough surface. The symmetry of this surface is not the group of arbitrary translations, but only translations by integral numbers of corrugation wavelengths. Reflection of phonons from such a surface is similar to the reflection of light from diffraction grating; in addition to specular reflection, waves with $k_{||}^{ref} = k_{||}^{in} + n\vec{q}$, $n = \pm 1, \pm 2, \pm 3, \cdots$ are also allowed by the symmetry of the problem, as shown in Figure 4.1. Infinite sets of linear equations can be constructed which represent the boundary conditions of equation (3.2) in terms of the reflected wave amplitudes, and I have devoted some effort to solving these equations numerically. Although this problem has many subtleties and is a very amusing problem in applied mathematics, it is not well adapted to detailed interpretation of experimental data because of its complexity. A real crystal surface is rough on a broad range of length scales. As mentioned in Chapter Two, it is difficult to describe quantitatively the surface condition of the crystals used in the experiments, or even to alter the surface roughness systematically. The surface roughness quoted by the manufacturer of ±25 nm is, however, comparable to the phonon wavelength in the crystal and considerably larger than the phonon wavelength in the helium. To provide a simple mathematical model of real crystal surfaces, it is useful to think of an "infinitely rough" surface which scatters incident radiation uniformly in all directions. An "infinitely rough" surface is thus similar to the black bodies of thermodynamics, except the randomization is in k space rather than in frequency.

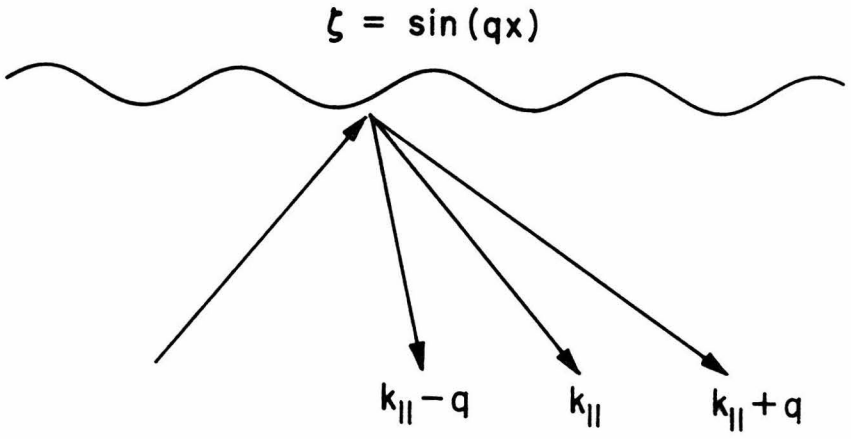

Figure 4.1. Scattering from a sinusoidally corrugated interface, showing the specular channel and the first two diffraction channels.

(The surface is assumed to be static, so the frequency of the incident and scattered waves is the same.) Another mechanism for destroying translational invariance is random stresses on the surface. These stresses could be provided by dislocation lines which terminate on the surface, or patches of adatoms.

Diffuse Scattering in an Isotropic Solid

A simple calculation using this model shows how crystal surface roughness can lead to the "tails" observed in many phonon reflection spectra. We will calculate the response of a bolometer to the nonspecular backscattering from a rough surface. For simplicity, we assume that a constant fraction α of the incident radiation is reradiated uniformly into all solid angles (fraction $(1 - \alpha)$ reflects specularly as if the surface was perfectly flat) and that the heater and bolometer are coincident points. h is the thickness of the crystal, c is the velocity of sound, r and ϕ are the polar coordinates on the reflection surface, and θ is defined in Figure 4.2. t is the time after the heater pulse, and Q(t) is the heat flux (j/sec) emitted by the heater as a function of time.

Each element of area $dA = rdrd\phi$ on the top surface is irradiated by phonons from the heater which arrive at $t = \sqrt{r^2 + h^2}/c$. If each element absorbs the fraction α of the incident energy and reradiates it, each area element can be considered as a new source of strength dQ_{dif}

$$dQ_{dif}(t) = \frac{\alpha \cos\theta \, Q(t - \frac{\sqrt{r^2 + h^2}}{c})}{r^2 + h^2} \, rdrd\phi \qquad (4.1)$$

The diffuse signal S(t) observed at the bolometer is due to the sum of all these elementary sources, and is given by

$$S(t) = \int_{\substack{\text{all} \\ \text{sources}}} \frac{dQ_{dif}\left(t - \frac{\sqrt{r^2 + h^2}}{c}\right)}{r^2 + h^2} \cos\theta \qquad (4.2)$$

Substituting $\cos\theta = h/\sqrt{r^2 + h^2}$, and performing the integral gives

$$S(t) = 2\pi \alpha h^2 \int_0^\infty \frac{Q\left(t - \frac{2\sqrt{r^2 + h^2}}{c}\right)}{(r^2 + h^2)^3} r\, dr \qquad (4.3)$$

If we assume a delta function heater pulse $Q(t) = Q_o \delta(t)$, the integral can be done explicitly to yield

$$S(t) = \begin{cases} 0 & t < 2h/c \\ 2\pi h^2 Q_o \left(\frac{2}{c}\right) \frac{1}{t^5} & t > 2h/c \end{cases} \qquad (4.4)$$

The diffuse signal rises abruptly to its maximum value of $Q_o \pi\alpha\, c/h^3$ at $t = 2h/c$, the arrival time of the specularly reflected pulse, and then decays as t^{-5} as shown in Figure 4.2. In view of the simple model used, this pulse shape seems to be in reasonable agreement with the experimentally observed diffuse scattering signal. This calculation also indicates that the "tail" due to nonspecular scattering from surface roughness has a rather sharp maximum at the same arrival time as the specular pulse, so it is intrinsically difficult to distinguish between them experimentally.

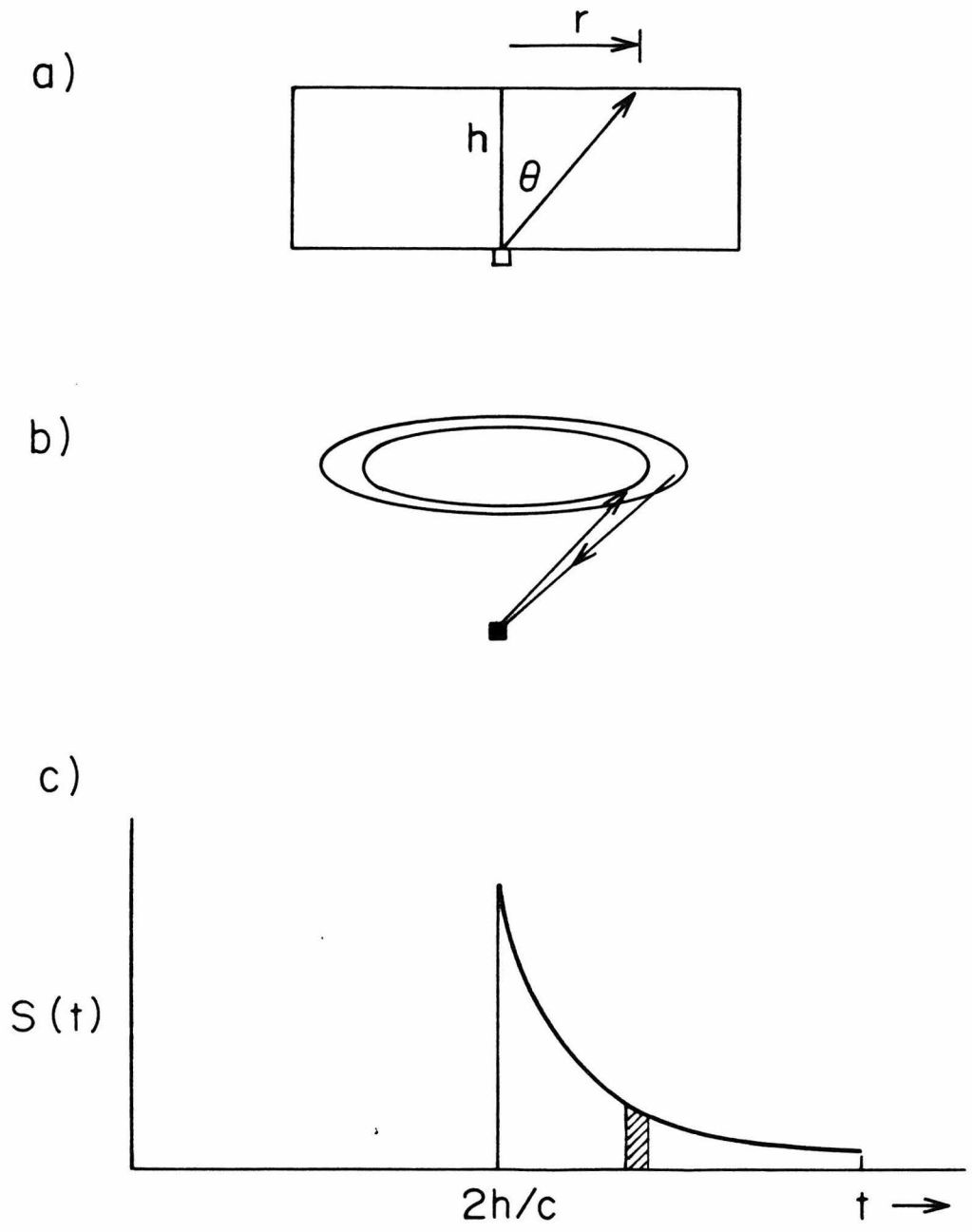

Figure 4.2. a) The geometry for the diffuse signal calculation. b) The contribution to the diffuse signal at a time t comes from a circular annulus on the reflection surface. c) A plot of the signal expected from an infinitely rough surface. The signal has a sharp onset at the time that a specular signal would arrive t = 2h/c.

It is important to estimate the magnitude of α, i.e., the probability of nonspecular scattering. α can be extracted from the experimental data by comparing the total energy which is scattered back to the detector in the specular and nonspecular channels. The total energy in the specular channel is the area under the specular peak. For a delta function heat pulse $Q(t) = Q_o \delta(t)$, the integral of the specular signal is

$$E_{spec} = \int S_{spec}(t)\, dt = \frac{Q_o(1 - \alpha)}{4h^2} \tag{4.5}$$

The total energy E_{dif} which arrives at the detector via nonspecular channels is

$$E_{dif} = \int S_{dif}(t)\, dt = \alpha\, 2\pi\, Q_o\, h^2 \left(\frac{2}{c}\right)^4 \int_{2h/c}^{\infty} \frac{dt}{t^5} = \frac{\alpha Q_o \pi}{2h^2} \tag{4.6}$$

The ratio of the specular to diffuse energy depends only on the fraction of diffuse scattering:

$$\frac{E_{spec}}{E_{dif}} = \frac{(1 - \alpha)}{\alpha} \frac{1}{2\pi} \tag{4.7}$$

This ratio can also be obtained from the experimental data. The only difficulty is in clearly separating the specular and diffuse signal close to the specular arrival time. If the pulse shape of the diffuse signal is extrapolated back to the onset of the specular pulse, the area under the respective curves can be obtained by counting squares. When this

procedure is applied to the last arriving transverse pulse in the Y-C plane data (Figure 3.9), and compared to equation (4.7), the computed values of α are approximately $\alpha \simeq 0.5$.

Another relationship which can be derived from these arguments is the behavior of the specular and diffuse signals as a function of the crystal thickness. The time integral of both signals scales as h^{-2}, as one would expect, but the maximum of the nonspecular signal scales as h^{-3}. The ratio of the specular to the diffuse scattering signal at $t = 2h/c$, the specular pulse arrival time,

$$\frac{S_{spec}\ (2h/c)}{S_{dif}\ (2h/c)} \propto h \qquad (4.8)$$

increases linearly with h. Thus experiments with long crystals allow a better separation of specular and diffuse scattering than short ones.

Although these calculations are only qualitative, they nevertheless clarify several issues which have gone unrecognized by previous workers:

1. approximately half of the phonons incident on the surface of a polished crystal are diffusely scattered. Reflection from a flat surface is not a realistic model for these experiments;
2. the signals due to specular and diffuse scattering overlap and have coincident maxima;
3. in order to measure the reflection coefficient for a well defined reflection process, the diffuse scattering signal should be subtracted out;

4. the reflection signal and pulse shape depends on the thickness of the crystal. For longer crystals, the specular scattering signal becomes predominant at the position of the peak, and;
5. when the diffusely scattered signal is properly accounted for, the data appear to be consistent with acoustic mismatch theory; i.e., the specular part of the signal does not change when helium is introduced. Diffuse scattering seems to be responsible for the anomalous Kapitza conductance. This interpretation is justified by the change in pulse shape when helium is added and the differences between results in long and short crystals.

Although this simple model adequately describes the diffuse scattering signal observed in the C-Y plane data of Figure 3.9, it cannot explain the sharp diffuse peaks of the X-Y plane data, nor can it explain why the diffuse signal should be so sensitive to crystallographic orientation.

Effects of Anisotropy

The elementary considerations discussed above suggest that diffuse scattering is important for understanding both phonon reflection experiments and the Kapitza resistance. In view of the complicated effects of anisotropy on the reflection process, and the strong dependence of the diffuse scattering signal on crystallographic orientation, it seemed important to include crystal anisotropy in the analysis. Elastic anisotropy introduces two major changes in the diffuse signal calculation of the previous section:

1. because the k vector and the energy flux or Poynting vector $\vec{p}$ of a phonon in a crystal are not collinear, the energy flux emitted from the heater is not uniform even if, as we assume, the k vectors of the emitted phonons are uniformly distributed. This effect, known as phonon focusing, was first investigated by Taylor et al.[19] Phonon focusing influences the amount of energy which reaches a given point on the surface from the heater, as well as the intensity of scattering from this point in the direction of the detector.
2. in the isotropic case, the contribution to the diffuse signal between t and t + Δt comes from a circular or elliptical ring on the reflection surface (see Figure 4.2). In a real crystal, however, the set of points on the reflection surface which have total flight time t from heater to detector via the surface is some irregular curve that has no convenient analytic expression.

In order to take these effects into account and to identify the position on the reflection surface which was responsible for the diffuse peaks observed in the X-axis experiments, I set out to make contour plots of the energy distribution on the reflection surface and the flight time for each mode. By superimposing these contour plots, I hoped to be able to examine the intensity on the reflection surface at points which had flight times which corresponded to the mysterious diffuse peaks.

The ostensibly straightforward project of constructing the contour plots was much more difficult to carry out than I had originally anticipated. Due to some subtleties of the problem outlined below, the

program as originally envisioned cannot be completed. Despite these complications, the analysis required for the construction of the contour plots eventually yielded a very useful picture of the energy flow in a crystal. In particular, it was found that a point source in a crystal emits energy in a spectacularly anisotropic way. Associated with a point source are several topologically conical surfaces on which the energy flux density formally becomes infinite. These singular surfaces, which are known as caustics, are very important for the interpretation of the diffuse scattering signal. Before discussing the analysis of caustics, it is important to describe the procedure used to construct the contour plots of time-of-flight and intensity, and some of the difficulties which were encountered.

The contour plots were constructed by interpolating values of the intensity and time-of-flight from a 20 x 20 table of computed values. This grid of 400 points represented a 4 cm^2 area on the reflection surface centered above the heater. Both the intensity and the time-of-flight depend on the Poyntings vector $\vec{p}$, which in turn depends in a complicated way on the k vector and polarization, as given by equation 3.5. For each point in the grid, it was first necessary to find the k vectors which corresponded to Poyntings vectors which cause energy to flow from the heater to the grid point and then back to the detector. This involved iterative calculations similar in principle to those described in Chapter Three. Since the k vector calculation had to be performed hundreds of times per contour plot, it was necessary to write an efficient algorithm to find $\vec{k}$ given the direction of $\vec{p}$ in order to keep the computing time within reasonable limits.

By analogy to the specular reflection analysis, one might expect that there are nine processes which connect heater and detector via an arbitrary grid point. Since each of the nine scattering processes has a distinct arrival time, one would expect to require nine separate arrival time contours for a complete description. In order to simplify the problem, we confined attention to the non-mode conversion transverse → transverse scattering processes, which the experiments indicated were most important.

The difficulties in labeling the transverse modes in an anisotropic solid were discussed in Chapter Three. The solution to the problem described there of continuing the polarization in a continuous way from some fiducial point was also used in constructing contour plots for processes which could be labeled, e.g., 3 → 3. Unfortunately, this labeling scheme did not give unique answers when applied to a general grid point. More precisely, the polarization can be continuously transported along a closed path on the slowness surface, and the initial and final polarizations may not be equal. The reason for this behavior seems to be that there exist points where the curves of constant ω (sections of the slowness surface) for the two transverse modes osculate, as shown in Figure 4.3. In a sense, the surfaces touch without crossing. Starting from one curve on one side of the point A, one can continue the polarization continuously to either curve on the other side of the point. This seems to mean that there is no way, even in principle, to divide the transverse reflection processes into globally distinct classes which have a continuous variation of some vectorial characteristic of the

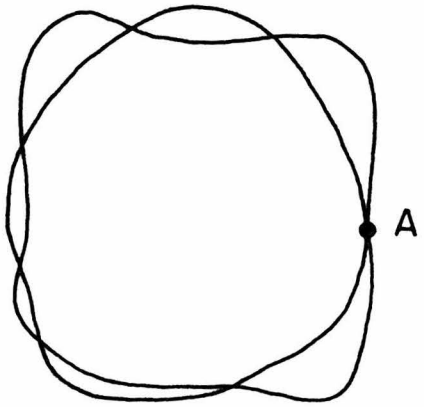

Figure 4.3. Curves of constant ω in k space for transverse modes. Point A is an osculation point where the curves are tangent to each other.

phonon. The previous success of the method for the analysis of the specular processes is due to the fortunate circumstance that no osculation point was in the vicinity of the connecting paths.

Because of the phonon labeling problem, it is impossible to associate with each grid point the flight time of a given transverse phonon scattering process; the best that can be hoped for is to associate with each grid point four k vectors and four times which correspond to two outgoing (from the heater) and two ingoing transverse phonons. Even this is optimistic, since in fact there may be more than two transverse phonons which cause energy flow between the heater and a given point on the reflection surface.

To see how this can happen, it is useful to remember that the group velocity of a wave packet, which is in the direction of energy flow,

is given by $\nabla_k \omega$. Thus, the normal vectors to the ω = constant surface, or slowness surface, are parallel to the energy flux vectors. The problem of finding all phonons that transport energy from the origin to a given point $\vec{x}$ can be interpreted geometrically as finding all points on the slowness surface with normal vector parallel to $\vec{x}$. If the slowness surface is convex like a sphere or ellipsoid, there is only one solution to the problem. If, however, the surface is more complicated, multiple solutions arise as shown in Figure 4.4. The figure shows three distinct k vectors which yield surface normals and energy flow in precisely the same direction, although the magnitude of the three group velocities is not obliged to be equal. The far field due to an instantaneous point

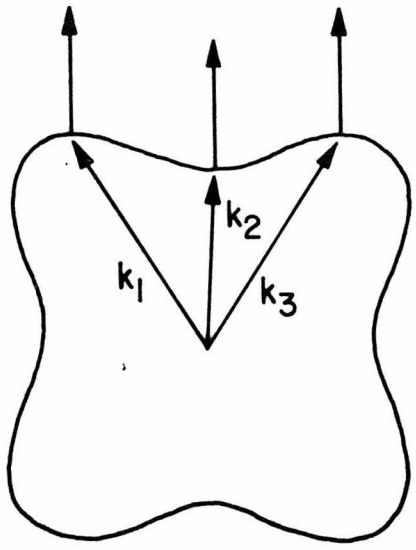

Figure 4.4. Schematic diagram of a non-convex cross section of one sheet of the slowness surface. All three k vectors correspond to energy flow in the same direction.

source may be quite complicated in an anisotropic medium; instead of observing three pulses corresponding to longitudinal, fast transverse and slow transverse, in some directions one may observe several pulses from each polarization. It seems that in sapphire the longitudinal sheet of the slowness surface is actually convex, so multiple solutions occur only for the transverse modes. It is easy to convince oneself that multiple solutions for the transverse branches are not confined to special high symmetry points, but occur in general directions as well. Detailed numerical calculation shows that there are many regions in sapphire in which five or six transverse pulses can be observed.

Before it was fully realized that many k vectors might lead to energy propagation in the same direction, the computational procedure for finding the k vector which sent energy in the $\vec{x}$ direction was based on using $\vec{k} \parallel \vec{x}$ as a first guess, and then improving the guess until a solution was found. As can be seen from Figure 4.4, this technique would only yield the solution $\vec{k}_2$; $\vec{k}_1$ and $\vec{k}_3$ cannot be reached by improving a guess which is close to $\vec{k}_2$. Moreover, there is no way to generate a guess a priori which is close to $\vec{k}_1$ or $\vec{k}_3$. Mathematically, the problem is to find the global solutions to a coupled set of non-linear vector equations in vector unknowns. Since the only practical way to solve non-linear equations is to improve a sufficiently good guess, it was necessary to compute the Poynting vectors for a dense grid of k vectors on the entire slowness surface to find good initial guesses for cases like $\vec{k}_1$ and $\vec{k}_3$ of Figure 4.4. With these added complications, one must be prepared to associate more than two ingoing and/or outgoing transverse phonon k vectors

with each grid point. Once all the k vectors have been found, the time-of-flight can be computed for each process in a straight forward manner.

Phonon Focusing

The computation of the intensity of the wave packet corresponding to each k vector involves the theory of "phonon focusing."[18,19] The way elastic anisotropy may focus or defocus energy is illustrated in Figure 4.5. A wave packet with k vectors contained in a solid angle given by $d\Omega_k = dk_1 \times dk_2$ sends energy into a solid angle $d\Omega_p = dp_1 \times dp_2$. In an isotropic solid, the k and p vectors are parallel, so $d\Omega_k = d\Omega_p$, and there is no focusing. In an anisotropic solid, however, the k vector pyramid and the corresponding Poynting vector pyramid may have considerably different shape. If $d\Omega_k > d\Omega_p$, the energy is focused, while if $d\Omega_k < d\Omega_p$, the energy is spread over a larger area and the intensity is low. The ratio $d\Omega_k/d\Omega_p$,

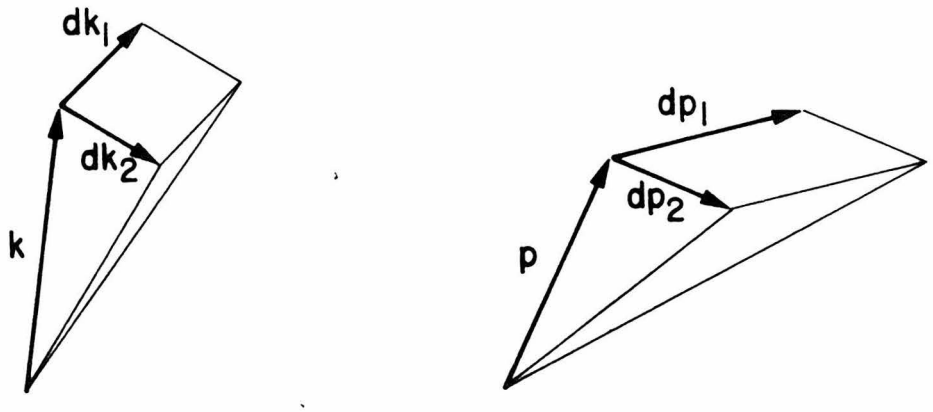

Figure 4.5. Differential volume element in k space with the corresponding volume element in real space spanned by the energy flux vectors $\vec{p}$.

which is called the focusing factor, can be used to measure the intensity of the energy flux which travels along $\vec{p}$. In order to calculate the differential area $d\Omega_p$, one must know the change dp caused by a change dk. This is given by the formula

$$dp_i = \frac{\partial p_i}{\partial k_i} \, dk_i \tag{4.9}$$

Because of the dependence of p_i on the polarization which in turn depends on k, the derivative $\partial p_i/\partial k_i$ is rather complicated. First, the k derivative of the polarization must be computed. The result is

$$\frac{\partial e_k^\gamma(k_j)}{\partial k_i} = \sum_{\alpha \neq \gamma} \frac{1}{\rho} (c_{ij\ell m} + c_{i\ell jm}) \frac{e_i^\alpha \, e_m^\gamma \, e_k^\alpha \, k}{v_\gamma^2 - v_\alpha^2} \tag{4.10}$$

where $e_i^\alpha(k_j)$ denotes the i^{th} component of the unit polarization vector of the α mode (α = 1, 2, 3) with k vector k_j and v_α is the corresponding phase velocity. Substituting into this expression the formula

$$\frac{\partial p_i^\alpha}{\partial k_i} = p_i^\alpha \, p_j^\alpha + \frac{1}{\rho} c_{njmi} \, e_n^\alpha, e_m^\alpha + c_{n\ell mi} \, k_\ell \left[\frac{\partial e_n^\alpha}{\partial k_j} \, e_m^\alpha + e_n^\alpha \frac{\partial e_m}{\partial k_j}\right] \tag{4.11}$$

yields the required derivative which can be used to compute the focusing factor. A computer program was written to compute the various derivatives and the intensity for each k vector associated with a grid point. This is apparently the first time these formulas have been used to calculate the intensities in arbitrary directions; previous applications have only

considered high symmetry directions in cubic crystals where the derivatives can be computed analytically.[18]

Once the analysis outlined above has been completed (a complete run requires about 1 CPU hour on the PDP-10), each grid point has associated with it a list of incoming and outgoing intensities and arrival times. In order to construct a contour plot, one phonon process must be selected at each grid point with its corresponding flight time and intensity. Because of the phonon labeling complications discussed above, there may not be a unique way to make the choice. This is not an insurmountable problem, since the contours will contain information of interest as long as they are reasonably continuous and smooth. It was found that smooth contours could be obtained by choosing the two processes with highest intensity and labeling them according to the magnitude of the group velocity as fast transverse and slow transverse.

A typical set of contour plots which results from this analysis is shown in Figures 4.6 and 4.7. Figure 4.6 shows the intensity distribution of the fast transverse mode on the upper surface of the sapphire crystal, and the rather dramatic effects of elastic anisotropy on energy flow in the crystal can be clearly seen. Figure 4.7 shows the contours of constant arrival time for all scattering processes that involve ingoing and outgoing fast transverse phonons for the experimental geometry corresponding to the reflection signal shown in Figure 3.13; i.e., heater and bolometer displaced by 2 mm along the X axis. The arrival time of the sharp nonspecular peak of 3.5 μsec is marked by the heavy contour. When the arrival time and intensity contour maps are superimposed, the heavy contour overlaps several regions of high intensity,

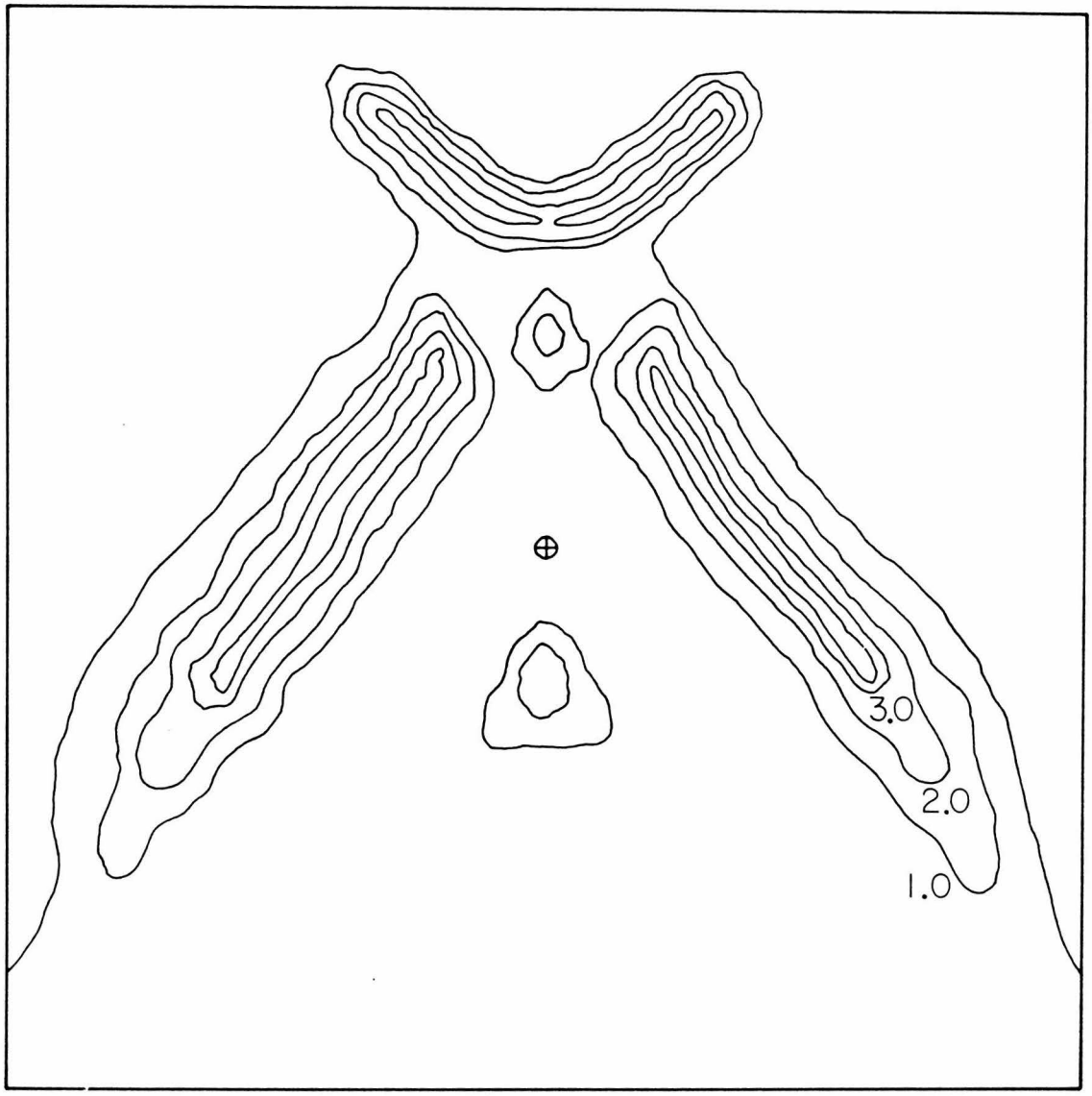

Figure 4.6. Contour plots of the intensity of the fast transverse mode on the reflection surface in sapphire. The circled cross marks the position of the heater on the lower surface of the crystal.

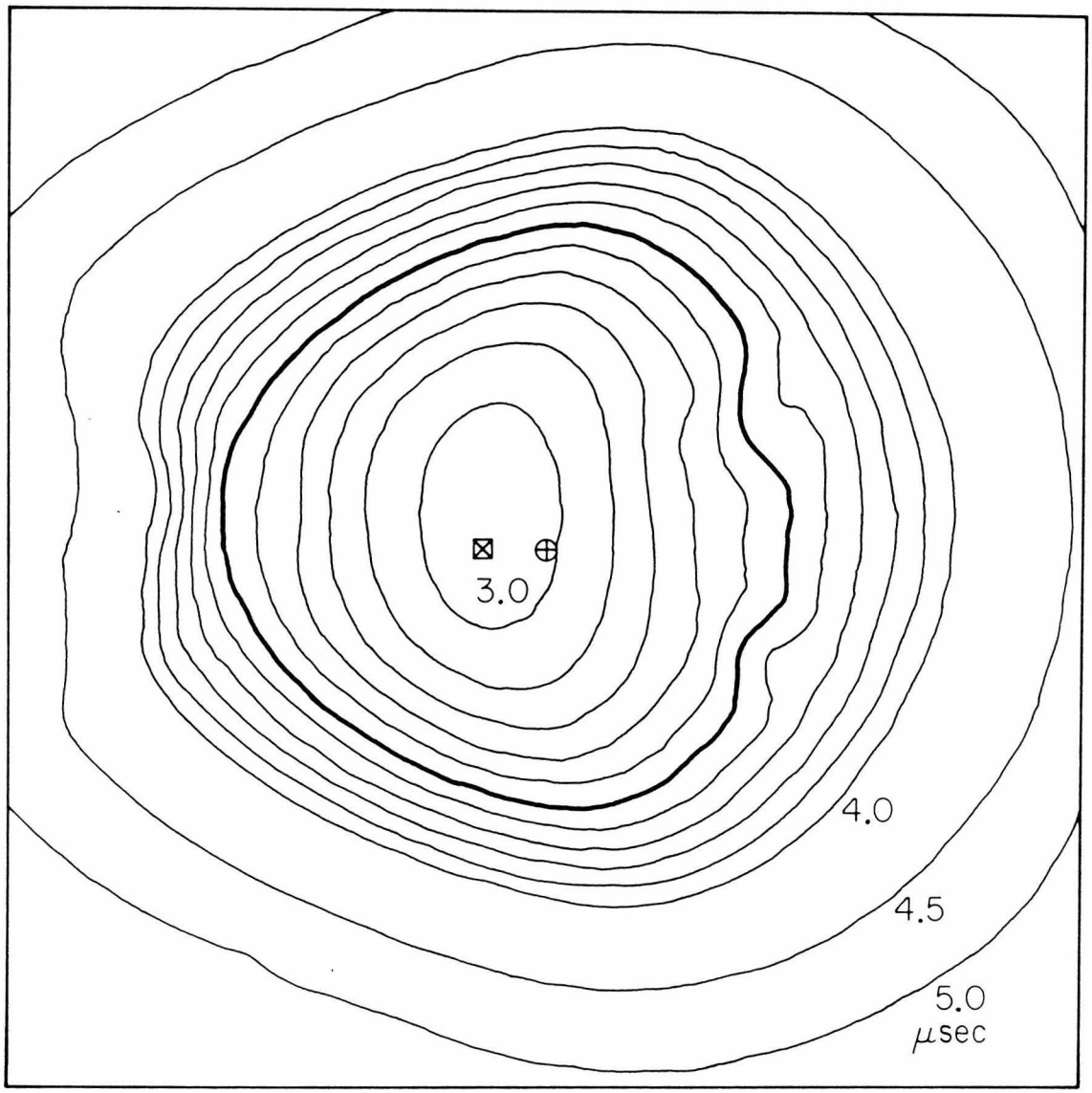

Figure 4.7. Contours of arrival time for fast transverse → fast transverse scattering processes. The circled cross marks the position of the heater on the lower crystal surface, while the squared cross marks the position of the bolometer.

but many other time contours overlap equally intense regions. The large diffuse feature seen in Figure 3.13 is apparently not simply due to the fact that the heater emits energy in a highly non-uniform way.

Phonon Focusing Catastrophes

During the course of further analysis of intensity contours like Figure 4.6, it was discovered that the numerical routines were unstable in some regions of high intensity, and the computer would sometimes converge on isolated points where the focusing factor was very large. Because the equations (4.10) and (4.11) for the focusing factor are rather complex, it is difficult to get a physical understanding of why the intensity is much higher in some regions than in others. In an attempt to gain some insight into this problem, I developed a different method of analyzing phonon focusing based on an analysis of the asymptotic field from a point acoustic source. The integrals which arise in the problem are of the type dealt with in formal catastrophe theory, and this theory can be used to make very general statements about the form of regions of high focusing using some simple geometric arguments.

A general expression of the acoustic field at x from a point source at x' is obtained by constructing the Green tensor $g_{km}(x|x')$ which satisfies the anisotropic wave equation with a periodic point source:

$$L_{ik}\, g_{km}(x|x') = \delta_{im}\, \delta(x - x') \qquad (4.12)$$

where, if $c_{ij\ell k}$ is the elastic tensor, then

$$L_{ik} = c_{ij\ell k} \frac{\partial^2}{\partial x_\ell \partial x_i} - \omega_o^2 \delta_{ik}$$

and its Fourier transform is

$$\tilde{L}_{ik} = c_{ij\ell k} k_i k_j - \omega_o^2 \delta_{ik}$$

A similar equation for the far field from a point source in an anisotropic medium is analyzed in references 37 and 38; the treatment here is adapted from these references.

To examine the field at a point P due to a source at the origin, we transform to a frame in which P has coordinates (0,0,z). The solution

$$g_{km}(P|0) = \int \frac{B_{km}}{(\partial G/\partial k_z)} e^{ik_z(k_x,k_y)\, z}\, dk_x\, dk_y \qquad (4.13)$$

where B_{km} is the matrix of cofactors of $\tilde{L}_{km}$, G = det $\tilde{L}$ and the integral is over the slowness surface defined by G = 0 (surface of constant ω in k space). Equation (4.13) represents the field at P in terms of a weighted sum of plane waves which have k vectors on the slowness surface. The integral cannot be carried out exactly, but for large z it can be approximated using the principle of stationary phase. The phase is stationary at points where $(\partial k_z/\partial k_x)$ and $(\partial k_z/\partial k_y)$ are zero; geometrically this represents points on the slowness surface with the normal vector in the $\hat{z}$ direction. Waves with k vector in the vicinity of the stationary point $\vec{k}_o = (k_x^o, k_y^o, k_z^o)$ contribute to the integral in equation (4.13), but waves with other k vectors tend to be out of phase and cancel each other. The

exponent in equation (4.13) can be expanded to second order around the stationary point, which, in an appropriately chosen coordinate system, yields:

$$k_z = k_z^o + \alpha(k_x - k_x^o)^2 + \beta(k_y - k_y^o)^2 \tag{4.14}$$

When this is substituted into equation (4.13) and the limits are extended to $\pm \infty$, the leading order behavior of the field is obtained:

$$g_{km}(P|0) \propto B_{km}(k_z^o) \frac{e^{ik_z^o z}}{z\sqrt{\alpha\beta}} \tag{4.15}$$

The product $\alpha\beta$ is the Gaussian curvature of the slowness surface at the point of stationary phase $\vec{k}^o$, and in this approximation, the field decreases as z^{-1} and the intensity is inversely proportional to the Gaussian curvature $\alpha\beta$. We have thus constructed a geometric representation of phonon focusing. In retrospect it is evident that the ratio of solid angles shown in Figure 4.5 is formally identical to the curvature of the slowness surface as defined by Gauss.

The geometric measure of focusing has considerable advantages over the traditional approach for making qualitative predictions. For instance it is clear that directions of high focusing are associated with regions of small curvature on the slowness surface and that points of zero curvature yield an infinity in the field amplitude. An infinite or even very large displacement is of course incompatible with linear elastic theory. This result is due to a breakdown of the geometrical optics approximation that has been made in deriving equation (4.15).

The possible form of regions of zero curvature can be investigated by considering perturbations of the slowness surface for an isotropic solid, which are spheres in k space. The effect of elastic anisotropy is to slightly deform the spheres; this generally (but not inevitably) leads to regions of negative curvature. Regions of positive and negative curvature are separated by smooth curves along which the curvature vanishes.

Vectors normal to the slowness surface along such a closed curve sweep out a (topologically) conical surface emanating from the point source on which the field is intense but cannot be computed using geometrical optics. Such surfaces are known as caustics in classical wave theory, and higher order approximations to the wave equation must be used to analyze the field in their vicinity.

If, for example α in equation (4.14) is close to zero, the expansion is not sufficiently accurate and another term must be included:

$$k_z = k_z^o + \alpha(k_x - k_x^o)^2 + \gamma(k_x - k_x^o)^3 + \beta(k_y - k_y^o)^2 \qquad (4.16)$$

The retention of the third order term is necessary because there are two nearby points where the phase is stationary, corresponding to two parallel rays, as shown in Figure 4.8. On the caustic, $\alpha = 0$, the rays merge, and the geometrical optics approximation goes to infinity, but the actual field is finite and is given by

$$g_{km}(P|0) \propto B_{km}(k_z^o) \frac{e^{ik_z^o z}}{z^{5/6}} \frac{1}{\beta^{1/2}} \frac{1}{\gamma^{1/3}} \qquad (4.17)$$

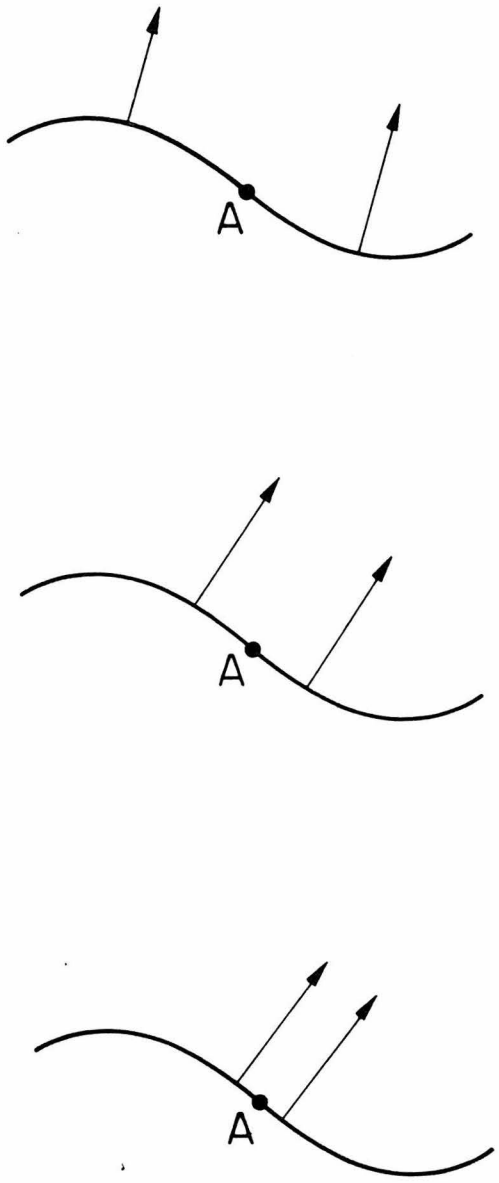

Figure 4.8. Section of a slowness surface which contains a point A of zero curvature. On either side of A, there are two k vectors which yield energy flow in the same direction. As the k vectors approach A, the two rays merge. Note that in the vicinity of A, the slowness surface can be approximated by a cubic polynomial like equation (4.16).

The intensity is not uniform along the caustic as suggested by the geometrical optics approximation, but rather depends on the third derivative term γ; remarkably, the field also has a $z^{-5/6}$ spatial dependence, rather than the z^{-1} dependence normally expected from a point source.

The breakdown of geometrical optics that occurs on a caustic is an example of a catastrophe in the sense of formal catastrophe theory. Many of the implications of catastrophe theory for optical and atomic beam caustics are explored in references 39 and 40. For elastic waves in a solid, catastrophe theory allows only two types of structurally stable caustic behavior. The simplest, known as a fold catastrophe, corresponds to the coalescence of two rays, and is associated with a third order expansion such as equation (4.16). Figure 4.8 shows how the rays merge at a simple inflection point. Along the caustic, γ may occasionally vanish at isolated points, where a fourth order expansion is required. These points are known as cusp catastrophes (because of the characteristic shape of the caustic) and correspond to the coalescence of three rays. A simple analysis shows that the field at a cusp has spatial dependence $z^{-3/4}$. No catastrophes of yet higher order can exist at a typical point. A summary of the catastrophe theory analysis of caustics in anisotropic media is shown in Figure 4.9.

Associated with each elementary catastrophe is a diffraction function which describes the far field in the vicinity of the caustic. For the fold catastrophe, the diffraction function is the Airy function, while the field in the neighborhood of a cusp is described in terms of the less well known Pearcey integral.[41] Using the diffraction functions,

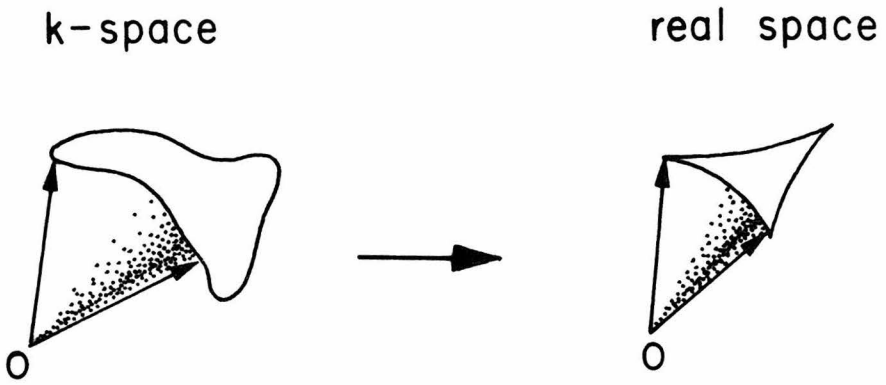

Figure 4.9. The k vectors which correspond to points of zero curvature on the slowness surface define a topologically conical surface in k space which has a smooth boundary, without sharp corners. The Poynting vectors which are associated with the k vectors also sweep out a topologically conical surface, but it generally has sharp cusp-like edges.

uniform asymptotic expansions can be constructed which vary continuously between the z^{-1} dependence at an ordinary point and the higher power of z dependence which holds on the caustic. Thus, catastrophe theory not only classifies the singularities but also describes the field in their vicinity. In addition, we see that the singular surface is associated with an anomalous region which may be responsible for a significant part of the energy in the entire field.

Once it was realized that the intensity distribution on the top surface of the crystal would be dominated by the caustic curves where the focusing factor was infinite, the computer programs used to construct the contour plot of Figure 4.6 were rewritten so that the caustics could be located and plotted, as shown in Figure 4.10. As expected on the basis of catastrophe theory, cusps where the field is particularly high are a prominent feature in the figure. A comparison of Figure 4.6, which was constructed from a table of intensities on a finite grid and Figure 4.10 which locates the caustics, shows that the intensity distribution interpolated from the finite grid can be quite misleading; only some of the high intensity regions visible in Figure 4.6 are associated with an underlying caustic, but these are the most important.

Application to Experimental Results

The caustic structure of the point source can be used to understand the sharp nonspecular features which are observed in some reflection geometries but not in others (compare Figures 4.11 and 4.12). It must be kept in mind, however, that in a reflection experiment diffusely

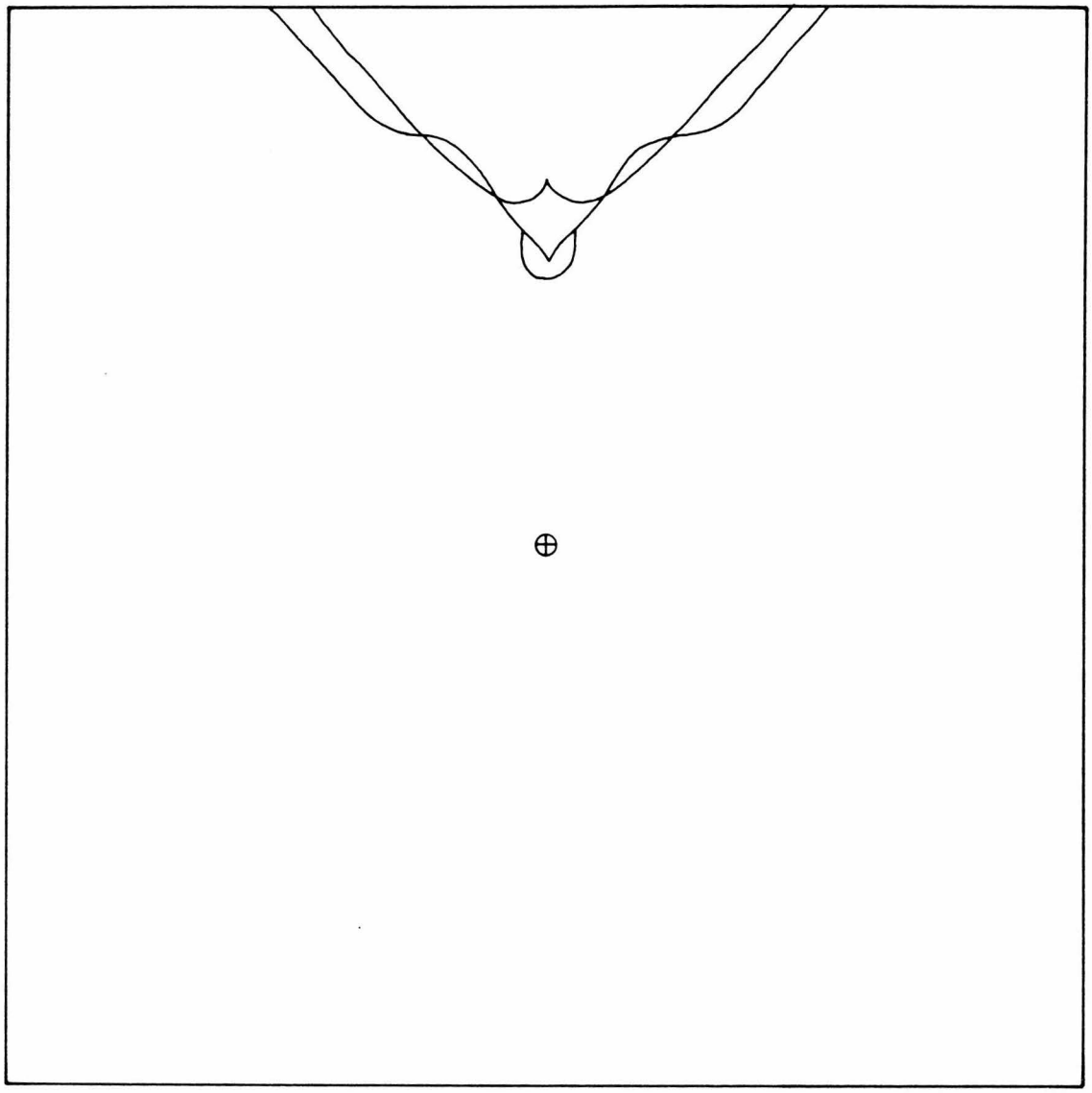

Figure 4.10. Location of caustics for both transverse modes in sapphire. The curves are the intersection of the topologically conical caustic surface which emanates from the heater with the upper surface of the crystal. The position of the heater is marked by the circled cross. Compare with Figure 4.5.

scattered phonons can be refocused by the crystal anisotropy. Thus there are two sets of caustics which are important to describe a reflection experiment: the heater caustics intersect the reflection surface in curves of high incident intensity, while similar caustics are associated with the detector and can be interpreted as a set of points where a source would focus strongly back to the detector. The insets of Figures 4.11 and 4.12 schematically show the orientation of the heater and detector caustics (detector caustic is dotted) for the two representative experiments. Although the caustics are drawn as lines, they have a width given by the size of the source and detector.

If the heater and detector are displaced along the X axis, as in Figure 4.11, the caustics overlap and there is a spatially localized high intensity nonspecular scattering channel. The time-of-flight of this process agrees precisely with the arrival time of the large diffuse peak.

If the heater and bolometer are placed along the C axis, the caustics do not overlap and there is no prominent peak in the diffuse scattering signal, as shown in Figure 4.12. When helium is introduced to the reflecting surface, the nonspecular part of the signal is greatly reduced. Thus, just as one would expect, the effect on the bump in Figure 4.11 is dramatic, while the signal in Figure 4.12 is much less affected.

In another experiment which was designed to test the intersecting caustics interpretation of the large nonspecular peak, the heater and bolometer were placed along the X axis as in Figure 4.11, but on a longer crystal (24 mm x 22 mm diameter). In this configuration, the caustics do not intersect on the reflection surface, but rather hit the side wall,

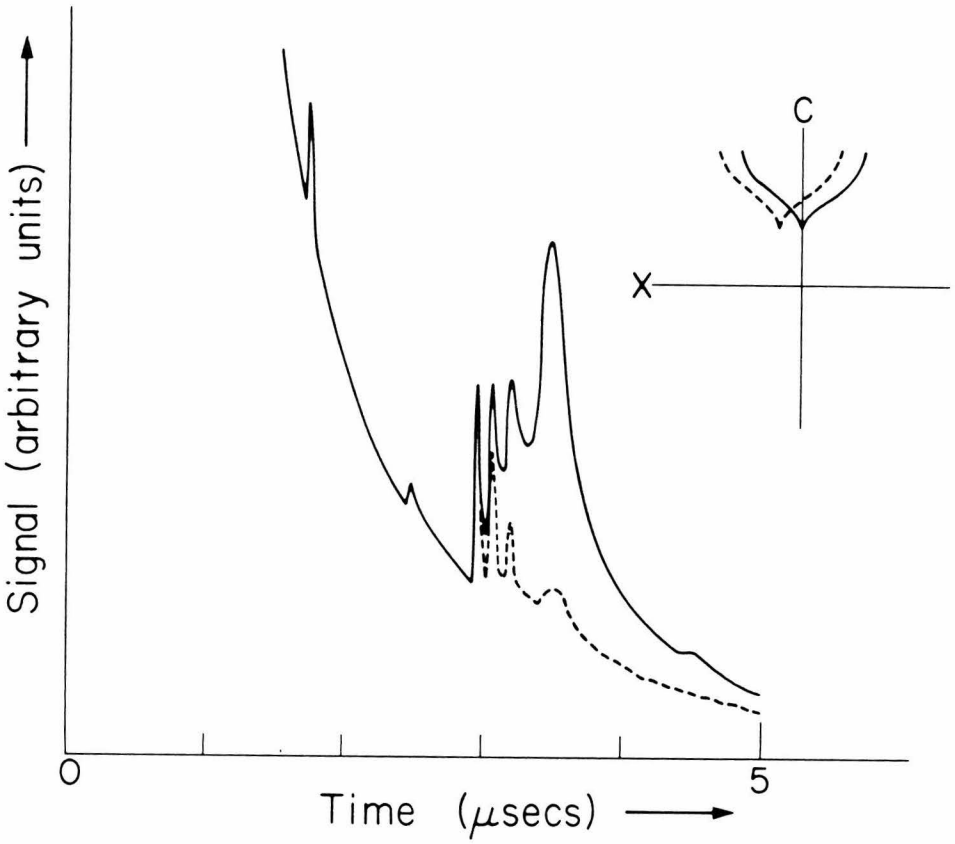

Figure 4.11. Reflection signal for heater and bolometer displaced along the X axis (Y axis is the reflection surface normal). The inset shows the intersection of the heater and bolometer (dotted curve) caustic surfaces with the crystal reflection surface. The intersection of the two caustics provides a high focusing channel for nonspecular scattering which gives rise to the large bump in the reflection signal.

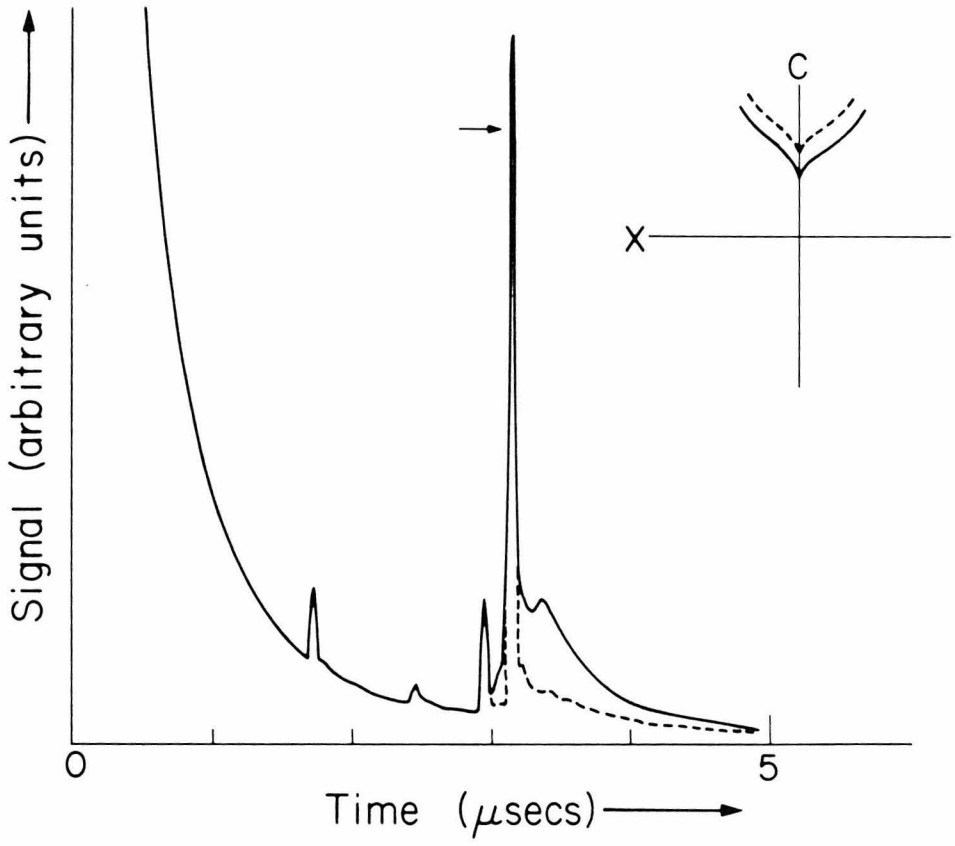

Figure 4.12. Reflection signal for heater and bolometer displaced along C axis. The inset shows that for this geometry, the heater and detector caustics do not intersect. The ratio of specular to diffuse scattering is much higher in this geometry than in X-Y plane reflection shown in Figure 4.11.

as illustrated in the inset of Figure 4.13; note that there is no large diffuse peak which follows the specular transverse peaks. Since the high focusing channels for diffuse scattering intersect the side wall, the diffusely scattered phonons arrive at a much earlier time than the specular phonons, which have made two traversals of the full length of the crystal. When the same crystal was cut and repolished, the diffuse scattering channel intersects the back reflection surface again, and the familiar diffuse bump following the specular channels is recovered, as shown in Figure 4.14. Note that the specular peaks, although shifted to different arrival times, are essentially similar in the two experiments; only the diffuse scattering is strongly affected by the shape of the crystal.

The analysis of caustics and the experimental results presented above have several important implications for the proper interpretation of phonon reflection experiments. Perhaps the most important conclusion is that the diffuse scattering signal behaves in two essentially different ways depending on whether the heater and bolometer caustics intersect or not. If the caustics do not intersect, the anisotropic emission of phonons from the heater is washed out by diffuse reflection, and the signal can be adequately described using an isotropic model. If the caustics intersect, the diffuse scattering produces rather sharp features which in the past have often been confused with specular peaks. The intersection or non-intersection of the caustics depends critically on the relative orientation of the heater and detector and the shape of the crystal. These parameters have been given insufficient attention by

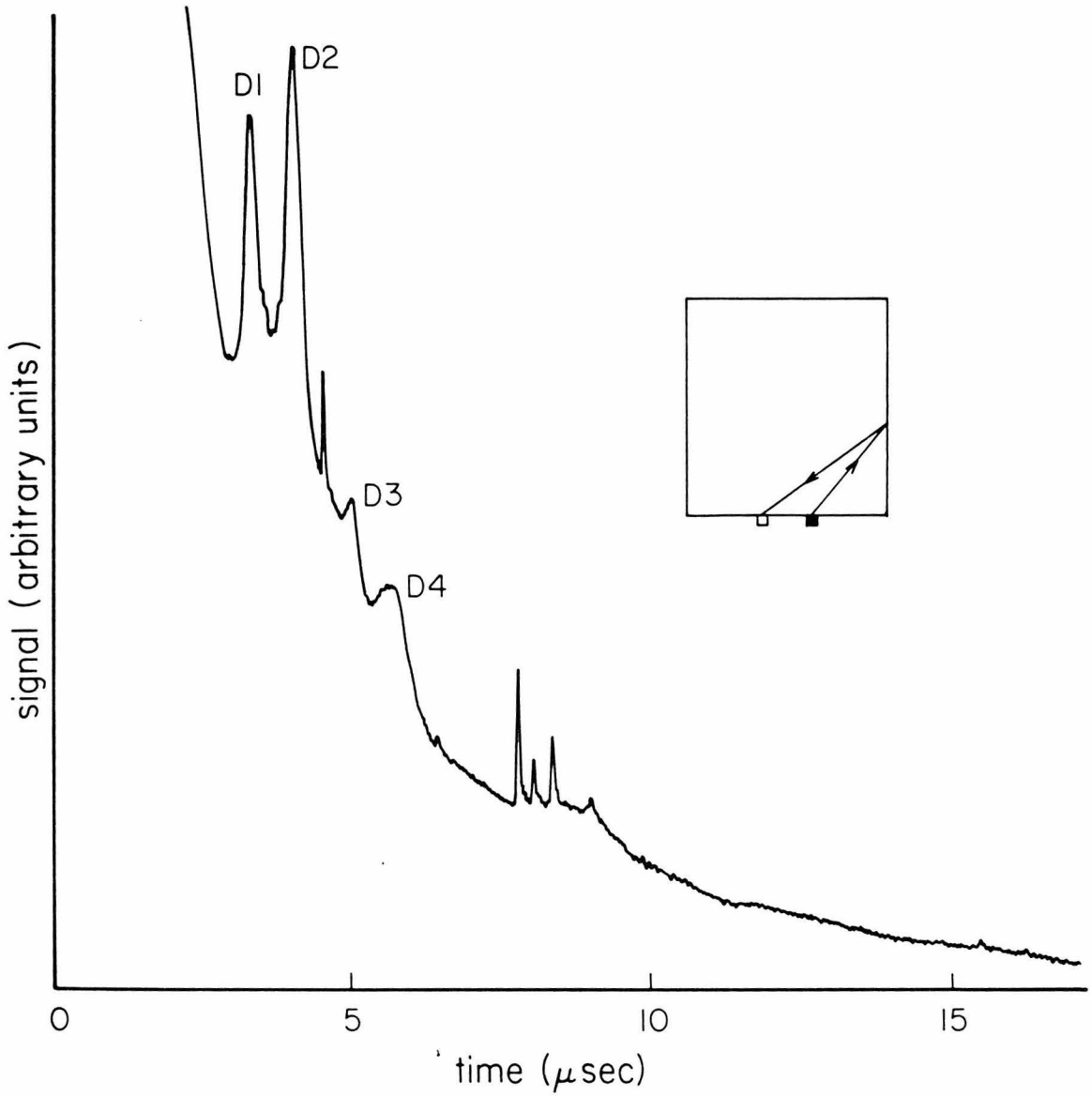

Figure 4.13. Reflection signal for heater and bolometer displaced along X axis (as in Figure 4.11) but in a crystal 24 mm x 22 mm dia. The heater and bolometer caustics intersect in several places on the side wall of the crystal, giving rise to the diffuse peaks D1, D2, D3 and D4. The three sharp peaks at 7.5 μsec are due to specular transverse processes; no large diffuse bump follows these peaks.

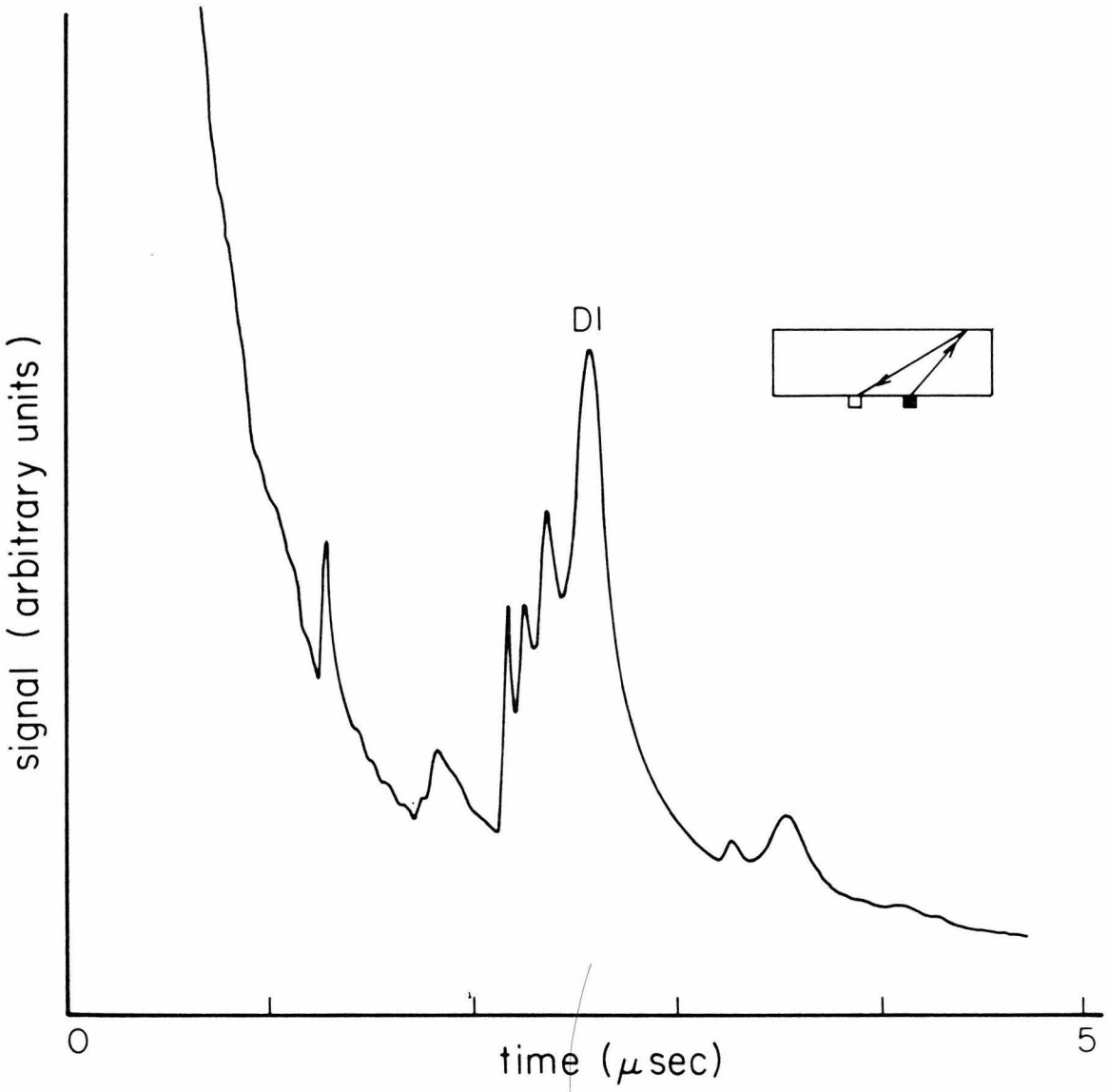

Figure 4.14. Reflection signal for precisely the same geometry as in Figure 4.13, except the crystal has been cut to a length of 6.9 mm. The caustics intersect on the reflection surface and cause the diffuse bump D1.

previous investigators. Many experiments have been reported in which the crystallographic plane of the reflection surface is specified, but the plane which contains the heater-detector surface normal is not. Even if the heater-detector separation is kept constant, changes in the relative orientation with respect to the crystal axes can completely change the received signal, and the apparent effect of helium.

It is interesting to note that the time-of-flight of the diffuse peaks can be predicted from the caustic structure of a point source alone; regions where the focusing factor is finite do not seem to contribute significantly to the diffuse signal. The published tables and plots[19,42] of average phonon intensities computed on a grid are misleading in the sense that they do not reveal the existence of the caustics. Instead, there are regions of elevated intensity, some of which conceal underlying caustics and contribute heavily to the experimental signal, and others which do neither. Thus, while the old phonon focusing calculations can be helpful in interpreting certain simple cases,[43] they cannot explain the details of the experiments described above.

In addition to its utility in predicting experimental results, the geometric theory of focusing developed here also provides an appealing theoretical framework for the discussion of phonon propagation in crystals. Although the detailed calculations are themselves rather involved, catastrophe theory provides a means of extracting a simple and general picture: from a point acoustic source in a crystal there emanate topologically conical caustic surfaces (fold catastrophes) with occasional higher order line singularities in those surfaces (cusp catastrophes). On the caustics the field falls off more slowly than $(\text{distance})^{-1}$, and

on the cusps more slowly still, but it always remains finite and calculable, as it must.

CHAPTER FIVE: SUMMARY AND SUGGESTIONS FOR FURTHER RESEARCH

As explained in the Introduction, the principle motivation for this work was to try to understand why heat transport across a solid/helium interface is so much more efficient than elastic theory suggests it should be. Unfortunately, the experimental results and analysis presented here do not provide an unequivocal answer to this question. What has been accomplished, however, is a greater understanding of what the predictions of elastic theory really are and how they should be applied to realistic experimental situations. The work of Chapter Three shows that phonon reflection spectra contain much more structure than had previously been supposed. Some of this structure can be understood by carefully applying an analysis based on anisotropic elastic theory to the reflection of phonons at a perfectly smooth interface. A considerable fraction of the received signal cannot be accounted for in this way, however, and must therefore be due to nonspecular scattering. Moreover, the nonspecular scattering signal seems to account for most, if not all, of the anomalous coupling to liquid helium. The intensity and pulse shape of the diffuse scattering is a sensitive function of the heater-bolometer orientation. This can be explained by introducing the concept of caustics, which are surfaces of high intensity associated with a point source.

The commonly accepted interpretation of phonon reflection experiments has been that elastic theory does not adequately describe the mechanical coupling between a solid and liquid helium. The implication

is that an additional (non-elastic) interaction mechanism exists between classical solids and quantum systems. It is our opinion that low time-of-flight resolution data and an unwarranted faith in isotropic elastic theory are at least partially responsible for these conclusions of previous researchers. We have found that the specular portion of the reflection signal seems to obey elastic theory exactly. Although the strong coupling of the diffuse scattering signal to liquid helium is still unexplained, we would like to suggest that it is premature to dismiss the possibility that elastic theory will eventually supply a complete explanation of the anomalous Kapitza conductance.

In our view, the problem of phonon reflection from a crystal/liquid helium interface is a difficult problem in classical mechanics which has not yet been thoroughly analyzed. Although the analysis of the effects of elastic anisotropy is an important step toward a more realistic theory, our results on the importance of nonspecular scattering suggest that surface roughness must also be taken into account. Several attempts have been made to incorporate the effects of surface roughness into Kapitza resistance calculations, but the results have been somewhat confusing. On the basis of a simplified (and unphysical) model, Little[44] concluded that the effect of surface roughness on the transmission of phonons was very small, and that this small effect tended to make heat transport less efficient than a flat interface. The complexity of the calculation and the negative nature of the result made surface roughness an unpopular explanation of the anomalous Kapitza resistance for many years. Recently several more sophisticated calculations have been published which conflict with Little's result. Adamenko and Fuks[45] ignore the

transverse phonons in the solid, but find that surface roughness may enhance heat transport by a factor of two. Castelan and Maradudin[46] compute the Kapitza resistance including the transverse phonons and find a factor of four increase in the heat transport efficiency. An unpublished calculation by N. Shiren[47] indicates that including the effect of surface roughness on surface wave scattering may decrease the theoretical Kapitza resistance to about one-tenth of the Khalatnikov value.

The mutual disagreement of these calculations suggests that the physics of the surface roughness problem is not completely understood, and much work must be done before these calculations can be meaningfully applied to realistic experimental situations. The calculations are all done from the liquid's point of view; i.e., the quantity which is actually calculated is the reflection coefficient for phonons incident from the liquid. Although the algebra is easier for this case, only the behavior of phonons incident from the solid are conveniently observable. Thus, the calculations mentioned above cannot be used to interpret phonon reflection experiments from a crystal/vacuum interface. Our philosophy throughout this work has been that a complete understanding of crystal/vacuum reflection spectra is essential to the further development of the phonon reflection technique. A detailed calculation describing the reflection of phonons in the solid from a rough interface would be a valuable aid in interpreting data.

Another difficulty in comparing theory with experiment is the fact that the condition of the surfaces used in the experiments is not well characterized. The predicted effect of surface roughness depends

sensitively on the parameters which describe the roughness, such as the mean square height and slope. Although these parameters are hard to measure accurately for a mechanically polished dielectric crystal, more effort should be devoted to careful surface characterization in future work. Measuring surface topography on Angstrom length scales may be difficult, but controlably altering it is even more difficut. Even cleaved or chemically etched crystal surfaces are atomically rough. The fact that surface roughness is not an experimentally adjustable parameter is another reason for trying to describe the effects with a realistic calculation. If a reliable theory were available, it would presumably predict the amount of diffuse scattering as a function of incident phonon wavelength. Even if the crystal roughness cannot be varied, tunable monochromatic phonon sources could be used to test the theory. It would be an important finding if the diffuse scattering peaks we have observed could be shown to be predominantly due to short wavelength phonons.

An important dimensionless number which characterizes the surface roughness scattering problem is the ratio of the rms roughness height to the wavelength. Scattering calculations are usually perturbation expansions in this supposedly small parameter. In most technologically important problems such as radar or sonar ranging, the small surface roughness limit is valid, but it is almost certainly not a good approximation for thermal phonons impinging on a polished crystal surface. Exact solutions of the wave equation for reflection from rough surfaces indicates that the perturbative solution breaks down for roughness heights larger than one-tenth of the wavelength. In typical phonon reflection experiments, the phonon wavelength in liquid helium is approximately 10 Å.

Since the rms roughness is probably larger than this, there is no reason to believe that perturbation calculations will work. At the conclusion of his discussion on the scattering of sound from rough surfaces, Rayliegh conjectures that "if we suppose the corrugations of a given period to become very deep and involved, it would seem that the condition of things would at last approach that of a very gradual transition between the media, in which case the reflection tends to vanish."[48] The high transmission coefficient one expects at a very rough interface cannot be predicted using perturbation theory. An exact calculation may be feasible, however. Numerical techniques have been developed to solve the similar problems which arise in atomic beam scattering experiments.[49] Such a realistic calculation is essential before we can determine whether phonon reflection experiments from crystal/helium interfaces can be explained in terms of classical mechanics, or if the anomalous Kapitza resistance is really due to some additional non-mechanical coupling.

REFERENCES

1. G.L. Pollack, Rev. Mod. Phys. 41, 48 (1969).
2. A.C. Anderson, in Phonon Scattering in Solids, ed. L.J. Challis, V.W. Rampton, and A.F.G. Wayatt (Plenum Press, New York, 1976), p. 1.
3. L.J. Challis, J. Phys. C. 7, 481 (1974).
4. P.L. Kapitza, Collected Papers of P.L. Kapitza, ed. D. ter Harr (Pergamon Press, Oxford, 1965), Vol. II, p. 581.
5. I.M. Khalatnikov, Zh. Eksperim. i Theor. Fiz. 22, 687 (1952); An Introduction to the Theory of Superfluidity (W.A. Benjamin, New York, 1965), p. 138.
6. L.M. Brekhovskiskh, Waves in Layered Media (Academic Press, New York, 1960), p. 35.
7. P. Herth and O. Weis, Z. Angew. Phys. 29, 101 (1970).
8. R.E. Peterson and A.C. Anderson, J. Low Temp. Phys. 11, 639 (1973).
9. J. Buechner and H. Maris, Phys. Rev. Lett. 34, 316 (1975).
10. C.J. Guo and H.J. Maris, Phys. Rev. A 10, 960 (1974).
11. A.C. Anderson, J.I. Connolly, and J.C. Wheatley, Phys. Rev. 135, A910 (1964).
12. A.C. Anderson and W.L. Johnson, J. Low Temp. Phys. 7, 1 (1972).
13. C.L. Reynolds and A.C. Anderson, Phys. Rev. B 15, 5466 (1977).
14. C.H. Anderson and E.S. Sabisky, in Physical Acoustics, ed. W.P. Mason and R.N. Thurston (Academic Press, New York, 1971).
15. C.J. Guo and H.J. Maris, Phys. Rev. Lett. 29, 885 (1972).
16. H. Kinder and W. Dietshe, Phys. Rev. Lett. 33, 1195 (1974).
17. P. Taborek and D. Goodstein, Rev. Sci. Instr. 50, 227 (1979).

18. H.J. Maris, J. Acoust. Soc. Am. 50, 812 (1970).

19. B. Taylor, H.J. Maris, and C. Elbaum, Phys. Rev. Lett. 23, 416 (1969).

20. G.W. Farnell, Can. J. Phys. 39, 65 (1961).

21. F.I. Federov, Theory of Elastic Waves in Crystals (Plenum Press, New York, 1968).

22. M.J. Musgrave, Crystal Acoustics (Holden Day, San Francisco, 1970).

23. J.B. Wachtman, Jr., W.E. Tefft, D.G. Lam, Jr., and R.P. Stinchfield, J. Res. Nat. Bur. Stan. 64A, 213 (1960).

24. R.V.G. Sundra Rao, Proc. Indian Acad. Sci. (A) 26, 352 (1949).

25. J. Bhimasenschar, Proc. Natl. Inst. Sci. India A 16, 241 (1950).

26. W.G. Mayer and E.A. Hiedemann, J. Acoust. Soc. Am. 30, 756 (1958).

27. J. Weber, W. Sandmann, W. Dietsche, and H. Kinder, Phys. Rev. Lett. 40, 1469 (1978).

28. R.L. Elgin and D.L. Goodstein, Phys. Rev. A 9, 2657 (1974).

29. M. Bretz, J.G. Dash, D.C. Hickernell, E.O. McLean, and O.E. Vilches, Phys. Rev. A 8, 1589 (1973).

30. M. Bretz, in Monolayer and Submonolayer Helium Films, ed J. Daunt and E. Lerner (Plenum Press, 1973), p. 11.

31. W. Dietshe and H. Kinder, J. Low Temp. Phys. 23, 27 (1976).

32. A.R. Long, R.A. Sherlock, and A.F. Wyatt, J. Low Temp. Phys. 15, 523 (1973).

33. P. Taborek and D. Goodstein, J. Phys. C., in press.

34. L.D. Landau and E.M. Lifshitz, Theory of Elasticity (Pergamon Press, New York, 1970).

35. D. Marx, J. Buck, K. Lassmann, and W. Eisenmenger, J. Phys. (France) C6, 1015 (1978).

36. J.T. Folinsbee and J.P. Harrison, J. Low Temp. Phys. 32, 469 (1978).

37. V.T. Buchwald, Proc. Roy. Soc. A 253, 563 (1959).

38. M.J. Lighthill, Phil. Trans. Roy. Soc. A 252, 397 (1960).

39. J.N.L. Connor, Mol. Phys. 31, 33 (1975).

40. M.V. Berry, Adv. Phys. 25, 1 (1975).

41. T. Pearcey, Phil. Mag. 37, 311 (1946).

42. A.K. McCurdy, Phys. Rev. B 12, 6576 (1978).

43. R.E. Horstman and J. Wolter, Phys. Lett. 62A, 279 (1977).

44. W. Little, Phys. Rev. 123, 435 (1961).

45. I.N. Adamenko and I.M. Fuks, JETP 32, 1123 (1971).

46. J. Castelan and A.A. Maradudin, to be published.

47. N. Shiren, reported at Third International Conference on Phonon Scattering in Condensed Matter, held Aug. 28-31, Brown University, Providence, Rhode Island.

48. J.W. Strutt, The Theory of Sound (Macmillian, London, 1926), Vol. II, p. 89.

49. N. Garcia, V. Celli and N.R. Hill, Phys. Rev. B 18, 5184 (1978).